University of Alberta

The Behaviour of Ni/YSZ based SOFC Anodes after Cyclic Reduction and Oxidation

by

David John Waldbillig ©

A thesis submitted to the Faculty of Graduate Studies and Research in partial fulfillment of the

requirements for the degree of *Master of Science*

in

Materials Engineering

Department of *Chemical and Materials Engineering*

Edmonton, Alberta

Fall 2004

Library and
Archives Canada

Published Heritage
Branch

395 Wellington Street
Ottawa ON K1A 0N4
Canada

Bibliothèque et
Archives Canada

Direction du
Patrimoine de l'édition

395, rue Wellington
Ottawa ON K1A 0N4
Canada

0-494-08191-0

Your file Votre référence
ISBN:
Our file Notre reference
ISBN:

NOTICE:
The author has granted a non-exclusive license allowing Library and Archives Canada to reproduce, publish, archive, preserve, conserve, communicate to the public by telecommunication or on the Internet, loan, distribute and sell theses worldwide, for commercial or non-commercial purposes, in microform, paper, electronic and/or any other formats.

The author retains copyright ownership and moral rights in this thesis. Neither the thesis nor substantial extracts from it may be printed or otherwise reproduced without the author's permission.

AVIS:
L'auteur a accordé une licence non exclusive permettant à la Bibliothèque et Archives Canada de reproduire, publier, archiver, sauvegarder, conserver, transmettre au public par télécommunication ou par l'Internet, prêter, distribuer et vendre des thèses partout dans le monde, à des fins commerciales ou autres, sur support microforme, papier, électronique et/ou autres formats.

L'auteur conserve la propriété du droit d'auteur et des droits moraux qui protège cette thèse. Ni la thèse ni des extraits substantiels de celle-ci ne doivent être imprimés ou autrement reproduits sans son autorisation.

In compliance with the Canadian Privacy Act some supporting forms may have been removed from this thesis.

While these forms may be included in the document page count, their removal does not represent any loss of content from the thesis.

Conformément à la loi canadienne sur la protection de la vie privée, quelques formulaires secondaires ont été enlevés de cette thèse.

Bien que ces formulaires aient inclus dans la pagination, il n'y aura aucun contenu manquant.

Canada

I would like to dedicate this work to my parents, my first teachers.

Abstract

The reduction and oxidation kinetics of a Ni/yttria stabilized zirconia (YSZ) cermet were studied using thermogravimetric analysis (TGA). It was found that the reduction kinetics were linear. Parabolic kinetics were observed for samples oxidized at low temperatures, but a divergence from parabolic kinetics was observed at oxidation temperatures greater than 700°C.

The volume changes that occurred after cyclic reduction and oxidation were measured using thermomechanical analysis (TMA). Anode substrate samples exhibited no dimensional change after reduction or oxidation at 750°C. Anode functional layer (AFL) samples did not change dimensions during reduction, but expanded by over 2% after oxidation at 750°C.

A baseline of the redox tolerance of an anode supported solid oxide fuel cell (SOFC) was characterized using electron microscopy and electrochemical testing. Cell performance decreased slightly after each redox cycle, especially for redox times greater than two hours. The microstructure of the cell was altered after redox cycling. The results from the baseline redox tests were used to develop four methods to enhance cell redox tolerance.

I would like to acknowledge the assistance I received from FuelCell Energy and all its employees. I would especially like to thank Tony Wood, Dale Steedman, Murray Tillman, Julia Protkova and Tahir Joia. Without the help of these people, this project would have been much more difficult.

I would also like to thank Beth Mackey for her patience and support.

Table of Contents

1. Summary 1-1

2. Fuel Cells 2-1

- 2.1. Advantages over traditional power generation technologies 2-4
- 2.2. History and development of fuel cells 2-5
- 2.3. Fuel cell operation 2-7
- 2.4. Fuel cell losses 2-9
- 2.5. Types of fuel cells 2-13
- 2.6. Fuel cell applications 2-28
- 2.7. Summary 2-34
- 2.8. Bibliography 2-36
- 2.9. References 2-38

3. Solid Oxide Fuel Cells (SOFC) 3-1

- 3.1. Advantages of SOFC 3-4
- 3.2. Challenges in SOFC 3-5
- 3.3. Cell design 3-6
- 3.4. SOFC components 3-13
- 3.5. Scope of thesis 3-29
- 3.6. Summary 3-30
- 3.7. Appendices 3-32
- 3.8. Bibliography 3-35
- 3.9. References 3-39

4. Reduction and oxidation kinetics of the Ni/YSZ system 4-1

- 4.1. Literature review 4-4
- 4.2. Thermogravimetric analysis (TGA) 4-5
- 4.3. Sample preparation 4-5
- 4.4. Experimental procedure 4-6
- 4.5. Microstructural characterization 4-8
- 4.6. Results and discussion 4-8
- 4.7. Summary 4-23
- 4.8. Appendices 4-25

4.9. References 4-27
5. Volume changes caused by reduction and oxidation of the Ni/YSZ system 5-1
5.1. Thermomechanical analysis (TMA) 5-4
5.2. Sample preparation 5-4
5.3. Experimental procedure 5-6
5.4. Microstructural characterization 5-7
5.5. Results and discussion 5-7
5.6. Summary 5-13
5.7. References 5-15
6. A baseline characterization of SOFC redox tolerance by electrochemical methods 6-1
6.1. Sample preparation 6-4
6.2. Test station description 6-6
6.3. Experimental procedure 6-6
6.4. Results and discussion 6-10
6.5. Summary 6-17
6.6. References 6-19
7. Characterizing the microstructural changes induced by redox cycling with electron microscopy 7-1
7.1. Sample preparation 7-5
7.2. Scanning electron microscopy (SEM) 7-5
7.3. Transmission electron microscopy (TEM) and scanning transmission electron microscopy (STEM) 7-7
7.4. Redox treatment of anode substrate samples 7-10
7.5. Redox treatment of fuel cell samples 7-10
7.6. Results and discussion – Anode substrate samples 7-10
7.7. Results and discussion – Fuel cell samples 7-22
7.8. Summary of redox microstructural changes 7-30
7.9. Bibliography 7-34
7.10. References 7-34
8. Enhancing the redox tolerance of SOFC 8-1

8.1. Low temperature redox cycling 8-5
8.2. Increasing AFL porosity 8-11
8.3. Functionally grading the AFL composition 8-15
8.4. Blocking air flow with an oxidation barrier 8-19
8.5. Summary 8-29
9. Recommendations and future work 9-1

List of Tables

Table 2-1: Summary of the major characteristics of the six types of fuel cells 2-14

Table 4-1: Summary of TGA testing conditions 4-8

Table 4-2: NiO reduction activation energy 4-11

Table 4-3: Activation energy from constant temp ramp rate calculations 4-15

Table 4-4: Literature values of NiO reduction activation energy (E_a) 4-16

Table 4-5: Ni oxidation activation energy values 4-20

Table 4-6: Literature values of Ni oxidation activation Energy (E_a) 4-21

Table 5-1: Summary of literature length change values 5-12

Table 6-1: Summary of the redox testing procedure 6-9

Table 8-1: Summary of the amount of cumulative degradation for the I-V curve tests for cells redox cycled at various temperatures 8-7

Table 8-2: Summary of the amount of cumulative degradation for the steady-state hold tests for cells redox cycled at various temperatures 8-8

Table 8-3: Summary of the amount of cumulative degradation for the I-V curve tests for cells with a graded AFL 8-18

Table 8-4: Summary of the amount of cumulative degradation for the steady-state hold tests for cells with a graded AFL 8-19

Table 8-5: Summary of the amount of cumulative degradation for the I-V curve tests for cells with an oxidation barrier 8-22

Table 8-6: Summary of the amount of cumulative degradation for the steady-state hold tests for cells with an oxidation barrier 8-23

Table 8-7: Summary of the amount of cumulative degradation after 4 hour redox cycles for cells with an oxidation barrier 8-24

Table 8-8: Summary of the percent enhancement in redox tolerance for all methods of redox tolerance enhancement 8-31

List of Figures

Figure 2-1: Schematic diagram of fuel cell inputs and outputs. 2-4

Figure 2-2: A comparison of electrical system efficiencies between a PAFC and other conventional energy conversion systems. 2-5

Figure 2-3: Arrangement of a Nernst glower in a lamp 2-6

Figure 2-4: Schematic diagram of the operation of a SOFC. 2-8

Figure 2-5: Picture of a SOFC stack. 2-9

Figure 2-6: Diagram showing an "exploded" view of two bipolar plates and the gas flow channels on their surfaces. 2-9

Figure 2-7: Schematic diagram of a polarization and power density curve. 2-10

Figure 2-8: TEM image of a fuel cell catalyst. 2-15

Figure 2-9: Image of a space shuttle launch. 2-16

Figure 2-10: Portable telephone powered by a DMFC. 2-17

Figure 2-11: Prototype DMFC system produced by Smart Fuel Cells. 2-17

Figure 2-12: Diagram of an AFC with mobile electrolyte. 2-19

Figure 2-13: AFC fuel cell with a static electrolyte contained in a matrix. 2-19

Figure 2-14: The world's first fuel cell vehicle (1959) powered by an AFC. 2-20

Figure 2-15: The Apollo space capsule orbiting the moon. 2-20

Figure 2-16: UTC fuel cell systems powering a postal facility in Alaska. 2-22

Figure 2-17: Dynamic equilibrium in MCFC elements. 2-24

Figure 2-18: MCFC field trials are underway. 2-26

Figure 2-19: HXS 1000 premiere SOFC system produced by Sulzer-Hexis. 2-28

Figure 2-20: Number of fuel cell systems built from 1990 to 2003. 2-28

Figure 2-21: 220kW SOFC/gas turbine hybrid system developed by Siemens-Westinghouse. 2-30

Figure 2-22: A 5kW Plug Power PEMFC system. 2-31

Figure 2-23: Chart of well-to-wheels energy efficiency. 2-32

Figure 2-24: Daimler Chrysler Citaro fuel cell bus. 2-33

Figure 2-25: Necar (New Electric Car) 4 produced by Daimler Chrysler. ... 2-33

Figure 2-26: Prototype DMFC powered laptop produced by NEC. 2-34

Figure 3-1: Cell-to-cell connections in a tubular SOFC stack 3-8

Figure 3-2: Schematic diagram of a tubular SOFC 3-9

Figure 3-3: Anode supported flat tube cells. 3-10

Figure 3-4: SEM micrograph of a micro-tubular SOFC LSM cathode support tube 3-11
Figure 3-5: SEM micrograph of a micro-tubular SOFC 3-11
Figure 3-6: Image of a planar anode supported SOFC 3-12
Figure 3-7: Typical microstructure of an anode supported SOFC 3-12
Figure 3-8: Typical microstructure of an electrolyte supported SOFC 3-12
Figure 3-9: Polished cross-section of an interconnect supported SOFC 3-13
Figure 3-11: Ionic conductivity of high temperature ionic conductors 3-17
Figure 3-12: SEM image of the anode functional layer anode substrate 3-25
Figure 4-1: Schematic diagram of a TGA sample. 4-6
Figure 4-2: Image of the TGA setup. 4-6
Figure 4-3: TGA curves for constant temperature reduction tests. 4-10
Figure 4-4: Arrhenius plots for reduction tests. 4-11
Figure 4-5: TGA curves for constant temperature ramp rate reduction test 4-12
Figure 4-6: Derivative of the reduction mass change curve vs temperature for different ramp rates. 4-14
Figure 4-7: Plots of $\ln(\alpha/T_m^2)$ vs $1/T$ for the 2 sets of T_m values for Ni reduction. 4-15
Figure 4-8: Kinetic plots for constant temperature oxidation tests. 4-17
Figure 4-9: Arrhenius plot for oxidation tests. 4-18
Figure 4-10: TGA curves for constant temperature ramp rate oxidation tests 4-18
Figure 4-11: Derivative of the oxidation mass change curve vs temperature for different ramp rates. 4-19
Figure 4-12: Plots of $\ln(\alpha/T_m^2)$ vs $1/T_m$ for Ni oxidation. 4-20
Figure 4-13: SEM BSE image TGA samples. 4-22
Figure 5-1: SEM image of a typical anode-supported SOFC. 5-5
Figure 5-2: Image of the TMA setup. 5-6
Figure 5-3: Reduction and oxidation TMA of the coarse structured anode samples. 5-8
Figure 5-4: Image of a oxidized coarse structured TMA sample. 5-8
Figure 5-5: Reduction TMA of the fine structured anode samples. 5-9
Figure 5-6: Oxidation TMA of fine structured anode samples 5-9
Figure 5-7: Images of an oxidized fine structured TMA sample. 5-11

Figure 5-8: SEM image of a fine structured TMA sample compared to the typical microstructure seen in a SOFC AFL layer. 5-13
Figure 6-1: TSC-2 cell manufacturing process diagram. 6-5
Figure 6-2: FCE's single cell testing stations. 6-6
Figure 6-3: I-V curves comparing the performance before and after redox cycling. 6-11
Figure 6-4: Summary of the cumulative percent degradation per redox cycle for I-V tests. 6-12
Figure 6-5: I-V curves measured before and after steady-state holds. 6-13
Figure 6-6: Steady-state holds comparing the performance before and after redox cycling 6-14
Figure 6-7: Summary of the cumulative percent degradation per redox cycle for the steady-state tests. 6-15
Figure 6-8: Voltage behaviour during oxidation. 6-17
Figure 7-1: Schematic of the TEM sample preparation process. 7-9
Figure 7-2: Optical micrograph of a TEM specimen. 7-9
Figure 7-3: BSE SEM image of a fresh fractured, as prepared sample. 7-11
Figure 7-4: Higher magnification SEM image of an as prepared sample. 7-11
Figure 7-5: BSE SEM image of a polished, as prepared (oxidized) sample. 7-11
Figure 7-6: BF TEM image of an as prepared sample. 7-12
Figure 7-7: EDX spectrum of a NiO grain in an as prepared sample. 7-12
Figure 7-8: EDX spectrum of an YSZ grain in an as prepared sample. 7-12
Figure 7-9: SEM image of a fresh fractured, partially reduced sample. 7-13
Figure 7-10: EDX spectrum of NiO grain shown in Figure 7-9. 7-13
Figure 7-11: EDX spectrum of Ni rim indicated in Figure 7-9. . 7-13
Figure 7-12: BSE SEM image of a fresh fractured, fully reduced sample. 7-14
Figure 7-13: Higher magnification SEM image of a fully reduced sample. 7-14
Figure 7-14: BSE SEM image of a polished, reduced sample. 7-14
Figure 7-15: HAADF STEM image of a reduced sample (inverted contrast). 7-16
Figure 7-16: BF TEM image of a reduced sample. 7-16
Figure 7-17: Schematic diagram of electron beam diffraction. 7-17
Figure 7-18: Schematic diagram of multiple diffraction in Ni/NiO/Ni layers 7-18
Figure 7-19: BSE SEM image of a reoxidized sample. 7-18
Figure 7-20: Higher magnification BSE SEM image of a reoxidized sample. 7-18

Figure 7-21: BSE SEM image of a polished, reoxidized sample. 7-19
Figure 7-22: BSE SEM image of a polished, partially reoxidized sample with EDX spectra from site 14.2 and site 14.3 in the figure. 7-19
Figure 7-23: HAADF STEM image of a reoxidized sample. 7-20
Figure 7-24: BF TEM image of a reoxidized sample. 7-20
Figure 7-25: HAADF STEM image of a rereduced sample 7-21
Figure 7-26: BF TEM image of a rereduced sample. 7-21
Figure 7-27: HAADF STEM image (inverted contrast) of rereduced sample. 7-22
Figure 7-28: SEM BSE image of an as prepared anode-supported SOFC. 7-22
Figure 7-29: SEM BSE image of a reduced anode-supported SOFC. 7-23
Figure 7-30: SEM image of a polished, reduced anode-supported SOFC. 7-23
Figure 7-31: SEM BSE image of a reoxidized anode-supported SOFC. 7-23
Figure 7-32: SEM image of a polished, reoxidized anode-supported SOFC. 7-23
Figure 7-33: Higher magnification SEM BSE image of a reoxidized anode-supported SOFC. 7-24
Figure 7-34: SEM BSE image of a rereduced anode-supported SOFC. 7-24
Figure 7-35: SEM image of a polished, rereduced anode-supported SOFC... 7-24
Figure 7-36: HAADF STEM image of an oxidized fuel cell sample showing the AFL-electrolyte interface. 7-25
Figure 7-37: HAADF STEM image of an oxidized fuel cell sample showing the AFL-anode substrate interface. 7-25
Figure 7-38: Higher magnification HAADF STEM image of an oxidized fuel cell sample showing the AFL-electrolyte interface. 7-26
Figure 7-39: EDX spectrum from point 1 in Figure 7-38. 7-26
Figure 7-40: EDX spectrum from point 2 in Figure 7-38. 7-26
Figure 7-41: Image of the anode side of an as prepared cell. 7-27
Figure 7-42: Image of the anode side of a reduced cell after testing. 7-27
Figure 7-43: Image of anode side of a partially reoxidized redox cycled cell. 7-28
Figure 7-44: Image of anode side of a fully reoxidized redox cycled cell. 7-28
Figure 7-45: Cross-sectional view of a partially reoxidized cell. 7-29
Figure 7-46: SEM image of an anode-supported SOFC after redox cycling.. 7-29
Figure 7-47: SEM image of an anode-supported SOFC after redox cycling. 7-29
Figure 7-48: SEM image of an anode-supported SOFC after redox cycling. 7-30
Figure 7-49: Higher magnification SEM image of Figure 7-48. 7-30

Figure 7-50: SEM BSE image of a fresh fractured as prepared sample. 7-31

Figure 7-51: SEM BSE image of a fresh fractured reduced sample. 7-31

Figure 7-52: SEM BSE image of a fresh fractured reoxidized sample. 7-31

Figure 7-53: SEM BSE image of the reoxidized sample in Figure 7-52 at higher magnification. 7-31

Figure 7-54: BF TEM image of an as prepared sample. 7-32

Figure 7-55: BF TEM image of a reduced sample. 7-32

Figure 7-56: BF TEM image of a reoxidized sample. 7-32

Figure 7-57: BF TEM image of a rereduced sample. 7-32

Figure 7-58: SEM BSE image of an as prepared anode-supported SOFC. 7-33

Figure 7-59: SEM BSE image of a reduced anode-supported SOFC. 7-33

Figure 7-60: SEM BSE image of a reoxidized anode-supported SOFC. 7-33

Figure 7-61: SEM BSE image of a rereduced anode-supported SOFC. 7-33

Figure 8-1: Summary of cumulative percent degradation per redox cycle for I-V curve tests for cells redox cycled at various temperatures. 8-6

Figure 8-2: Summary of cumulative percent degradation per redox cycle for steady-state tests for cells redox cycled at various temperatures. 8-7

Figure 8-3: Summary of cumulative percent OCV degradation per redox cycle for cells redox cycled at various temperatures. 8-9

Figure 8-4: SEM image of the anode substrate of a cell reoxidized at 600°C. 8-9

Figure 8-5: SEM image of the anode substrate of a cell reoxidized at 750°C. 8-9

Figure 8-6: SEM image of a reoxidized cell after a redox cycle at 600°C ... 8-10

Figure 8-7: SEM image of the carbon black particles used as pore formers. 8-11

Figure 8-8: SEM image of a cell with an AFL containing pore formers. 8-12

Figure 8-9: BSE SEM image of an as prepared cell with a regular AFL. 8-12

Figure 8-10: SEM image of a reduced cell with an AFL with pore formers. . 8-12

Figure 8-11: BSE SEM image of a reduced cell with a regular AFL. 8-12

Figure 8-12: SEM image of a reoxidized cell with AFL pore formers. 8-12

Figure 8-13: BSE SEM image of a reoxidized cell with a regular AFL. 8-12

Figure 8-14: Summary of cumulative percent degradation per redox cycle for I-V curve tests for cells with AFL pore formers. 8-14

Figure 8-15: Summary of cumulative percent degradation per redox cycle for steady-state tests for cells with AFL pore formers. 8-14

Figure 8-16: BSE SEM image of a cell with a functionally graded AFL. 8-16

Figure 8-17: SEM image of a reduced cell with a functionally graded AFL . 8-16

Figure 8-18: Summary of the cumulative percent degradation per redox cycle for I-V curve tests for cells with a graded AFL. 8-17

Figure 8-19: Summary of the cumulative percent degradation per redox cycle for steady-state tests for cells with a graded AFL...................... 8-18

Figure 8-20: Schematic diagram of a fuel cell with oxidation barrier layer... 8-20

Figure 8-21: BSE SEM image of a fuel cell with an oxidation barrier........... 8-21

Figure 8-22: Summary of the cumulative percent degradation per redox cycle for I-V curve tests for cells with an oxidation barrier................ 8-22

Figure 8-23: Summary of the cumulative percent degradation per redox cycle for steady-state tests for cells with an oxidation barrier. 8-23

Figure 8-24: High current and utilization results for a cell with an oxidation barrier. 8-25

Figure 8-25: BSE SEM image of the surface of a 57wt% NiO oxidation barrier layer in the reduced condition.. 8-26

Figure 8-26: BSE SEM image of the surface of a 57wt% NiO oxidation barrier layer in the reoxidized condition.. 8-26

Figure 8-27: BSE SEM image of the surface of a 75wt% NiO oxidation barrier layer in the reoxidized condition.. 8-26

Figure 8-28: Cross sectional BSE SEM image of a 57wt% NiO oxidation barrier in the as prepared condition. 8-27

Figure 8-29: Cross sectional BSE SEM image of a 57wt% NiO oxidation barrier in the reduced condition. 8-27

Figure 8-30: Cross sectional BSE SEM image of a 57wt% NiO oxidation barrier in the reoxidized condition.. 8-27

Figure 8-31: Cross sectional BSE SEM image of a 75wt% NiO oxidation barrier in the reoxidized condition.. 8-27

Figure 8-32: Voltage behaviour during oxidation for the baseline cell test. .. 8-28

Figure 8-33: Voltage behaviour during oxidation for oxidation barrier cell. . 8-28

Chapter 1: Summary

Abstract

This chapter summarizes the scope and results of the present study.

1. Summary

Fuel cells are a clean, efficient energy generation technology that produces electricity by the direct electrochemical combination of a fuel with an oxidant. This direct production of electricity effectively bypasses the conversion of the fuel's chemical energy into thermal and mechanical energy and thus allows higher theoretical efficiencies to be achieved.

Solid oxide fuel cells (SOFC) are a type of fuel cell that use a solid, ionically conducting ceramic oxide as an electrolyte. Due to the inherently low ionic conductivity of the solid electrolytes, these cells must be operated at temperatures between 600°C and 1000°C.

The most commonly used SOFC anode material is a two phase cermet composed of Ni and YSZ. Since this material is on the anode side, it is exposed to a reducing environment during operation and thus remains a cermet. However, the metallic component of the anode may reoxidize in a commercial SOFC system due to seal leakage, fuel supply interruption or system shutdown. In order to reuse a reoxidized cell, it must be reduced. Thus, cyclic reduction and oxidation (redox) of the anode is likely to occur during commercial SOFC operations. The reduction and oxidation of nickel will result in large bulk volume changes, which may have a significant effect on the integrity of interfaces within a fuel cell and thus result in performance degradation.

System redox solutions, such as the use of a reducing purge gas, are possible, but are cumbersome and expensive. Another possible redox solution is to change the anode material to a substance that is not as susceptible to oxidation, such as a ceramic oxide. However, there are currently no alternative anode materials that exhibit equivalent performance to the state-of-the-art Ni/YSZ materials system. Thus, if the anode material remains unchanged and system redox solutions are deemed too expense, the only remaining way to enhance SOFC redox tolerance is to modify the microstructure of the anode. This study investigates the baseline redox tolerance of SOFC produced using Fuel Cell Energy Ltd.'s (FCE) TSC-2 process and then uses the information obtained to modify the anode microstructure and enhance cell redox tolerance.

The initial characterization section was divided into four main areas.

Thermogravimetric analysis (TGA) was used to characterize the reduction and oxidation kinetics of SOFC anode substrates and to calculate an activation energy for reduction and oxidation. During reduction, linear kinetics were followed and a reduction activation energy of 78 kJ/mol was calculated. Parabolic kinetics were observed for samples oxidized at low temperatures and for low amounts of mass change. A divergence from parabolic kinetics was observed at oxidation temperatures greater than 700°C. An activation energy of 87 kJ/mol for reoxidation was calculated.

The volume change that occurred after cyclic reduction and oxidation was measured using thermomechanical analysis (TMA). Two types of samples were tested: one sample type had a relatively coarse microstructure similar to the anode substrate, while the other sample type had a fine microstructure similar to the anode functional layer (AFL). Anode substrate samples exhibited no dimensional change after reduction or oxidation at 750°C. AFL samples did not change dimensions during reduction, but expanded by over 2% after oxidation at 750°C. All AFL samples were severely cracked after oxidation; however, AFL samples that were oxidized at lower temperatures or that contained lower amounts of Ni expanded and cracked less than standard samples upon oxidation.

A baseline of the electrochemical degradation, after redox cycling for standard TSC-2 cells, was developed using the single cell testing facilities at FCE. Two types of electrochemical tests were performed: current-voltage (I-V) curves and steady-state hold tests. Cell performance decreased slightly after each redox cycle, but significant amounts of degradation did not occur until after the 2 hour redox cycle. After the redox cycles were complete, the overall cell performance degraded by 9.4% for I-V curve tests and by 7.9% for steady-state hold tests.

The microstructural changes that occurred after redox cycling were characterized using scanning and transmission electron microscopy (SEM and TEM). Redox cycling significantly changed the microstructure of the anode substrate of the cell. Initially, as prepared (oxidized) samples had an anode substrate composed of NiO particles several microns in size, YSZ grains about 1 micron in size and intergranular porosity. Using SEM, it was observed that the porosity of the anode substrate increased significantly after reduction and that a spongy NiO structure was formed after reoxidation. TEM analysis indicated that very fine intragranular pores formed within the Ni grains after reduction and, upon reoxidation, very fine (<100 nm) randomly oriented NiO grains nucleated and grew. The change in the AFL microstructure was more difficult to characterize due to the very fine structure of this layer. The AFL appeared to be more porous after reduction and quite dense after reoxidation. Some microstructural damage was observed after redox cycling. Vertical cracks in the electrolyte, likely caused by AFL oxidation, volume expansion and AFL microstructural damage, were observed in some redox cycled samples.

The baseline results from this study were used to develop four methods to enhance cell redox tolerance. The redox tolerance of the enhanced cells was then compared to baseline cells.

TGA showed that the reaction kinetics of nickel oxidation were very temperature dependent, which means that the rate of anode oxidation should slow down as the redox temperature is lowered. As well, TMA showed that the amount of oxidation volume expansion decreased at lower oxidation temperatures. Therefore, redox cycles at lower temperatures should cause less volume expansion during oxidation and thus less cell layer delamination and electrolyte cracking should be decreased. The effect of lowering the redox temperature was examined by performing redox cycles at 600, 650 and 700°C and the results were compared to baseline redox tests at 750°C. Redox cycling at 700°C enhanced the cell redox tolerance by over 50%, while cycling at 600°C decreased the amount of redox degradation between 80 and 90%, when compared to baseline redox tests at 750°C.

All the fine microstructured AFL samples expanded and cracked during TMA oxidation tests regardless of the oxidation temperature; however, none of the coarse microstructured anode substrate samples expanded or cracked. Anode substrate samples have much larger pores, which allows the volume increase due to oxidation to be accommodated by filling this added porosity rather than by fracturing the YSZ skeleton. Nanosize carbon black pore formers were added to the AFL paste in order to increase the porosity of the AFL. Unfortunately, cells with AFL pore formers degraded rapidly, which indicates that the microstructure was not sufficiently optimized for stable performance.

TMA testing showed that AFL samples, containing more than 30wt% and less than 57wt% NiO, expanded less than standard samples during oxidation. Therefore, a reduction in the amount of Ni in the AFL of the cell might reduce the amount of volume expansion during oxidation and thus increase the redox tolerance. The amount of Ni in the AFL must be high enough to ensure that the AFL has sufficient electronic conductivity, triple phase boundary length and porosity, but should be as low as possible in order to minimize the amount of oxidation volume expansion. In order to best satisfy these opposing demands, the Ni content in the AFL can be functionally graded to ensure that the Ni content is high near the anode substrate and lower near the electrolyte. Grading the AFL increased the redox tolerance of the cell by 10 to 40% depending on the AFL composition used.

A fine microstructured layer was printed on the bottom of the anode substrate to act as an oxidation barrier layer. Under the reducing conditions seen during operation, the barrier layer is porous to allow fuel to pass through. If the anode conditions become more oxidizing, the layer will rapidly oxidize and densify which will slow down the rate that oxygen penetrates into the anode. Cells with an oxidation barrier had a 40% improvement in redox tolerance for redox cycles up to 4 hours in length; however, the redox tolerance after the 6 hour cycle was only slightly improved when compared to baseline redox tests. This indicates that the oxidation barrier does not completely stop the flow of oxygen into the cell. The barrier only slows down the rate at which oxidation can occur.

This study used a variety of techniques to more fully characterize the redox behaviour of Ni/YSZ cermets and to develop a baseline of cell redox tolerance and redox induced microstructural changes and electrochemical performance degradation. The knowledge was then successfully used to modify the anode microstructure in order to create an SOFC with enhanced redox tolerance.

Chapter 2: Fuel Cells

Abstract

Fuel cells are a clean efficient energy generation technology that produces electricity through the direct electrochemical reaction of a fuel with an oxidant. Although the origins of fuel cells can be traced back to the early 19th century, fuel cells are only now becoming feasible for commercial applications. There are four main areas of commercial interest for fuel cells: stationary power, distributed generation, transportation and small scale portable power. Six main types of fuel cells have been developed with the typical difference between differing cell types being the type of electrolyte used.

Chapter 2: Fuel Cells

List of Figures 2-3
List of Tables 2-3

2. Fuel Cells 2-4
  2.1. Advantages over traditional power generation technologies 2-4
  2.2. History and development of fuel cells 2-5
  2.3. Fuel cell operation 2-7
  2.4. Fuel cell losses 2-9
    2.4.1. Equilibrium voltage 2-10
    2.4.2. Losses due to leakage and electronic conductivity 2-11
    2.4.3. Activation overpotential 2-11
    2.4.4. Ohmic losses 2-12
    2.4.5. Mass transport losses 2-12
  2.5. Types of fuel cells 2-13
    2.5.1. Polymer Electrolyte Membrane Fuel Cell (PEMFC) 2-14
    2.5.2. Direct Methanol Fuel Cells (DMFC) 2-16
    2.5.3. Alkaline Fuel Cell (AFC) 2-17
    2.5.4. Phosphoric Acid Fuel Cell (PAFC) 2-20
    2.5.5. Molten Carbonate Fuel Cell (MCFC) 2-21
    2.5.6. Solid Oxide Fuel Cells (SOFC) 2-25
  2.6. Fuel cell applications 2-27
    2.6.1. Stationary power plants (>10kW) 2-28
    2.6.2. Distributed generation (<10kW) 2-29
    2.6.3. Transportation 2-30
    2.6.4. Small scale portable power (1W to 1.5kW) 2-32
  2.7. Summary 2-33
  2.8. Bibliography 2-35
  2.9 References 2-37

List of Figures

Figure 2-1: Schematic diagram of fuel cell inputs and outputs. 2-4
Figure 2-2: A comparison of electrical system efficiencies between a PAFC and other conventional energy conversion systems. 2-5
Figure 2-3: Arrangement of a Nernst glower in a lamp................................. 2-6
Figure 2-4: Schematic Diagram of the Operation of a SOFC........................... 2-8
Figure 2-5: Picture of a SOFC stack. 2-9
Figure 2-6: Diagram showing an "exploded" view of two bipolar plates and the gas flow channels on their surfaces. 2-9
Figure 2-7: Schematic diagram of a polarization and power density curve. .. 2-10
Figure 2-8: TEM image of a fuel cell catalyst. 2-15
Figure 2-9: Image of a space shuttle launch. 2-16
Figure 2-10: Portable telephone powered by a DMFC. 2-17
Figure 2-11: Prototype DMFC system produced by Smart Fuel Cells. 2-17
Figure 2-12: Diagram of an AFC with mobile electrolyte. 2-19
Figure 2-13: AFC fuel cell with a static electrolyte contained in a matrix....... 2-19
Figure 2-14: The world's first fuel cell vehicle (1959) powered by an AFC. . 2-19
Figure 2-15: The Apollo space capsule orbiting the moon. 2-19
Figure 2-16: Five UTC fuel cell systems powering a postal facility in Alaska 2-21
Figure 2-17: Dynamic equilibrium in MCFC elements. 2-23
Figure 2-18: MCFC field trials are underway. 2-25
Figure 2-19: HXS 1000 premiere SOFC system produced by Sulzer-Hexis. .. 2-27
Figure 2-20: Number of fuel cell systems built from 1990 to 2003 2-28
Figure 2-21: 220kW SOFC/gas turbine hybrid system developed by Siemens-Westinghouse. 2-29
Figure 2-22: A 5kW Plug Power PEMFC system. 2-30
Figure 2-23: Chart of well-to-wheels energy efficiency. 2-31
Figure 2-24: Daimler Chrysler Citaro fuel cell bus. 2-32
Figure 2-25: Necar (New Electric Car) 4 produced by Daimler Chrysler. 2-32
Figure 2-26: Prototype DMFC powered laptop produced by NEC. 2-33

List of Tables

Table 2-1: Summary of the Major Characteristics of the Six Types of Fuel Cells.. 2-14

2. Fuel Cells

Fuel cells are an energy generation technology that produces electricity quietly, cleanly and efficiently through the direct electrochemical combination of a fuel with an oxidant. This direct production of electricity effectively bypasses the conversion of the fuel's chemical energy into thermal and mechanical energy and thus allows higher theoretical efficiencies to be achieved. A schematic diagram of the inputs and outputs for fuel cells is show in Figure 2-1.

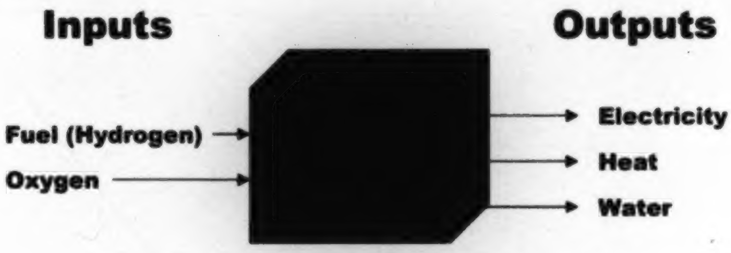

Figure 2-1: Schematic diagram of fuel cell inputs and outputs.

2.1. Advantages over traditional power generation technologies

Fuel cells have many advantages over traditional power generation technologies. They are highly efficient, easily modular, simple to maintain as they have no moving parts, able to use multiple fuels, small in size, and able to operate silently. However, perhaps the greatest advantage of fuel cells over the majority of traditional power generation technologies is their environmental compatibility. If hydrocarbon sources are used as fuel, fuel cells produce no combustion product pollutants such as NO_x and SO_x. If hydrogen is used as the fuel, water vapour is the only byproduct. Recent interest in distributed power generation also benefits fuel cells. Distributed power generation reduces the capital costs for the provider and improves overall plant efficiency by improving the ability to cogenerate electricity and heat. Figure 2-2 shows a comparison of the efficiency of a phosphoric acid fuel cell (PAFC) with other types of energy conversion systems. As worldwide concerns about the environment and the overdependence of the industrialized world on fossil fuels continues to grow, fuel cells are an attractive option to provide dependable, efficient distributed power without contributing poisonous emissions into the environment.

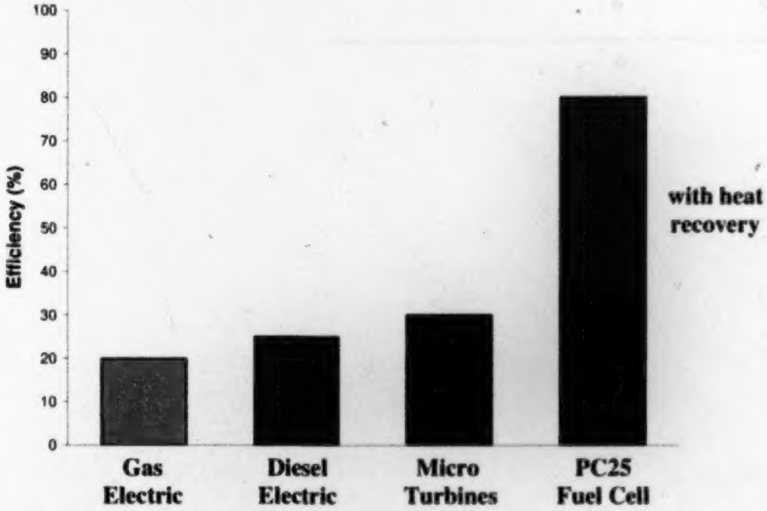

Figure 2-2: A comparison of electrical system efficiencies between a PAFC and other conventional energy conversion systems.[1]

2.2. History and development of fuel cells

Fuel cells are one of the oldest modern energy conversion systems. Although the initial concept for fuel cells has been ascribed to Sir Humphrey Davy in 1802, Sir William Grove is commonly credited with the practical invention of the fuel cell in 1839. Grove studied water electrolysis and reasoned that it might be possible to reverse the process and generate electricity. He used two platinum electrodes in oxygen and hydrogen submersed in an electrolyte of dilute sulfuric acid and successfully produced a small amount of electricity. He stated: "A shock was given which could be felt by five persons joining hands, and which when taken by a single person was painful."

In 1853, Gaugain made the important discovery of the first solid electrolyte cell. He performed thermoelectric experiments between metal contacts on glass and porcelain. He observed that, "the new source of electricity possesses all the characteristic features of an aqueous-electric cell" and thus acted as a galvanic solid electrolyte gas cell (fuel cell).

Another large contribution to solid oxide fuel cells was made by Nernst when he noticed that the conductivity of mixed metal oxides was much higher than the individual pure components. In 1899, Nernst patented the particularly conductive mixture of 85% ZrO_2 doped with 15% Y_2O_3 (YSZ) for his glowers. Today YSZ is the most commonly used solid oxide electrolyte. Thus Nernst's glowers may be thought of as the first commercially produced solid electrolyte gas cells. An illustration of a Nernst glower in a lamp from a patent filed April 9, 1899 is shown in Figure 2-3. Although Nernst was convinced that his glowers were ionic conductors this assertion could not be proven until 1943 when Wagner discovered that the ionic conductivity of these solutions was caused by the existence of vacancies on the anion sublattice of mixed oxide solid solutions.

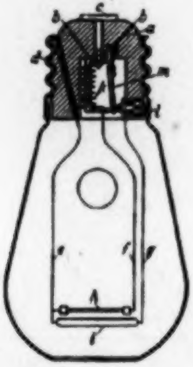

Figure 2-3: Arrangement of a Nernst glower in a lamp (from a patent filed April 9, 1899). [2]

By the early 20th century the first solid electrolyte fuel cell patents began to be filed. Haber filed a patent on a fuel cell using porcelain or glass as the electrolyte material (depending on the temperature of operation) in 1905, which was then followed by Baur and Treadwell's patent of a fuel cell using metal oxides as the electrodes and ceramic solids with salt melts in the pores as the electrolyte.

The use of YSZ as the electrolyte in a solid oxide fuel cell was first proposed by Schottky in 1935 and in 1937 Bauer and Preis fabricated a fuel cell using a YSZ electrolyte running at 1000°C. However, the high operating temperature and various materials problems limited the stability and performance of the cell. These problems hindered the development of SOFC until the 1960's.

By the mid 20th century the rate of development of SOFC increased greatly. Initial research focused on characterizing and optimizing the ionic conductivity of the solid electrolyte and producing thinner, dense electrolyte materials. This work resulted in the adoption of YSZ as the standard electrolyte material for SOFC. Another important development was Spacil's composite anode electrode. He used layers of Ni mixed with the solid electrolyte material in order to deal with adhesion and thermal expansion problems present in SOFC anodes. This composite Ni anode is used in the vast majority of modern SOFC.

Currently, much SOFC research focuses on increasing SOFC lifetimes, optimizing performance, reducing costs and investigating poisoning and degradation mechanisms. These areas are critical to ensure the successful commercialization of SOFC and there are a number of companies worldwide that are close to a commercial SOFC product.

2.3. Fuel cell operation

All fuel cells consist of two electrodes (the anode and the cathode), which are separated by an ionically conducting electrolyte. At the cathode, oxygen in the oxidizing gas (usually air) is reduced to form oxide ions. If the electrolyte is an oxygen ion conductor (for example, an SOFC) the ions can then migrate through the electrolyte to oxidize the fuel gas at the anode. An excess of electrons at the anode is produced by the oxidation of the fuel. For single cell operation the electrons pass along an external circuit and through an electrical load. Eventually the electrons reach the electron deficient cathode and reduce the oxygen in the oxidizing gas. The current flow from the anode to the cathode produces direct current electricity. A schematic diagram of SOFC operation is shown in Figure 2-4. The overall reaction seen in a fuel cell operating on pure hydrogen fuel is shown in Reaction 2-1.

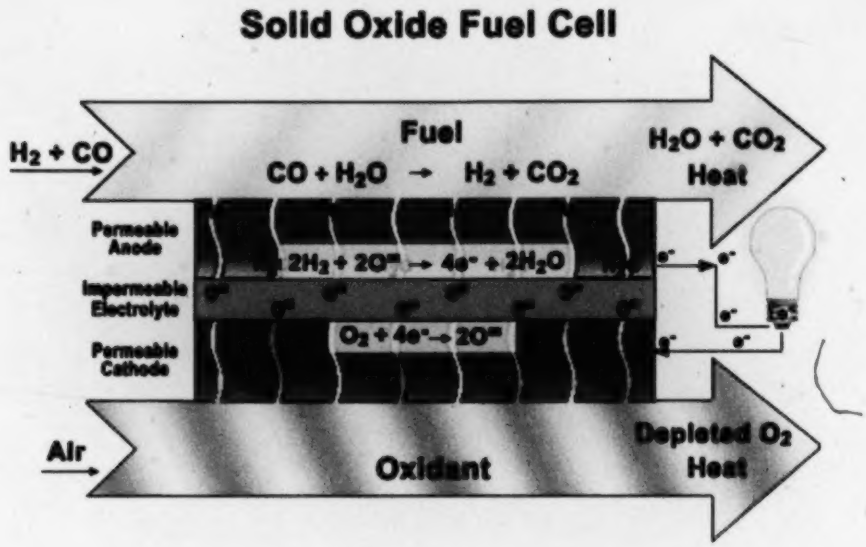
Solid Oxide Fuel Cell
H2 + CO
Fuel
CO + H2O → H2 + CO2
H2O + CO2
Heat
Permeable Anode
Impermeable Electrolyte
Permeable Cathode
2H2 + 2O= → 4e- + 2H2O
O2 + 4e- → 2O=
e-
Air
Oxidant
Depleted O2
Heat

Figure 2-4: Schematic diagram of the operation of a SOFC. [3]

Overall reaction: $\frac{1}{2}O_2 + H_2 \rightarrow H_2O$ Reaction 2-1

Individual fuel cells produce less than 1 V of potential under typical operating conditions. Therefore commercial fuel cell operations usually involve the connection of a number of cells in series in order to increase the voltage. The connected cells are called stacks. An image of a SOFC stack is shown in Figure 2-5. For a SOFC, an interconnect electrically connects the anode of one cell to the cathode of the next. In other types of fuel cells these interconnects are known as bipolar plates. Bipolar plates/interconnects typically are flat pieces with shaped grooves for gas flow. They are often made of graphite (low temperature fuel cells), stainless steel (MCFC and SOFC), or electrically conductive ceramics (SOFC). A schematic diagram showing an "exploded" view of two bipolar plates is seen in Figure 2-6.

Figure 2-5: Picture of a SOFC stack. [4]

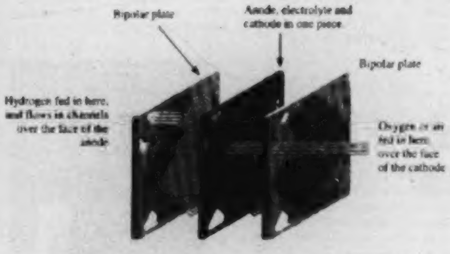

Bipolar plate
Anode, electrolyte and cathode in one piece
Bipolar plate
Hydrogen fed in here, and flows in channels over the face of the anode
Oxygen or air fed in here, over the face of the cathode

Figure 2-6: Diagram showing an "exploded" view of two bipolar plates and the gas flow channels on their surfaces. [5]

2.4. Fuel cell losses

One of the key measures of fuel cell performance is a plot of the voltage versus current density called a polarization curve. From these values, a power density curve can be calculated by multiplying the voltage by the current density. As the current density is increased the voltage decreases due to various losses. The power density will increase until about half the open circuit voltage is reached and then will decrease. These effects can be seen schematically in Figure 2-7. The measured voltage (E) can be broken down into a number of components, which represent the various losses that occur during operation and can be written in the following form:

$$E = E_{eq} - E_{L} - E_{act} - E_{IR} - E_{trans} \qquad \text{Equation 2-1}$$

where: E_{eq} is the reversible equilibrium voltage, which is calculated from the thermodynamics of the reaction

E_{L} is the voltage loss due to leaks across the electrolyte and due to partial electronic conductivity in the electrolyte

E_{act} is the activation overpotential due to slow electrode reactions

E_{iR} is due to ohmic resistances in the cell

E_{trans} is the overpotential due to mass transport limitations

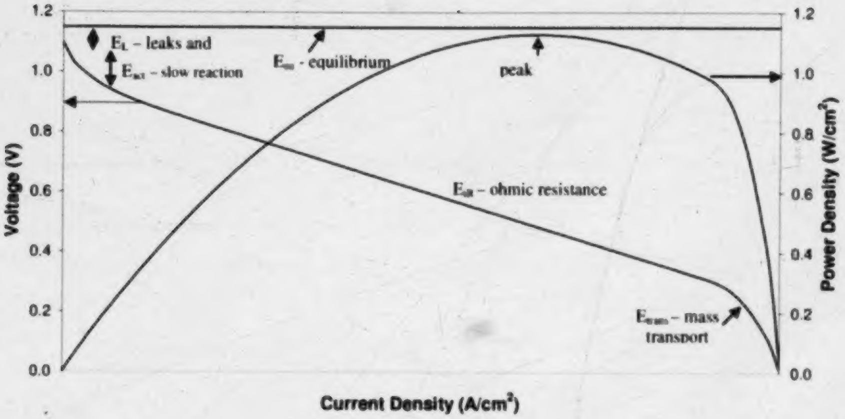

Figure 2-7: Schematic diagram of a polarization and power density curve.

2.4.1. Equilibrium voltage

E_{eq} can be calculated from thermodynamics by determining the change in Gibbs free energy (ΔG) for the fuel cell reactions under operating conditions (Equation 2-2).

$$E_{eq} = -\frac{\Delta G}{nF} \qquad \text{Equation 2-2}$$

where: n is the number of electrons transferred in the reaction
F is Faraday's constant

ΔG for a typical fuel cell reaction (Reaction 2-1) can be determined by the following equation:

$$\Delta G = \Delta G^\circ + RT \ \ln\left(\frac{P_{H_2O^\circ}}{P_{H_2} P_{O_2}^{1/2}}\right) \qquad \text{Equation 2-3}$$

where: ΔG° is the Gibbs free energy when all species are in their standard states (1 atm pressure, pure condensed species)
P is the actual pressure of the various components (H_2, O_2, H_2O) during fuel cell operation

2.4.2. Losses due to leakage and electronic conductivity

Under open circuit voltage conditions the measured voltage should be exactly the reversible equilibrium voltage, but in practice this is rarely the case. Deviations from the equilibrium voltage may be caused by gas leakage due to poor sealing, electrolyte cracks or by electronic conductivity within the electrolyte, which causes internal short circuits. The E_L term may be minimized by: increasing the temperature (except in the cases where raising the temperature increases the electronic conductivity of the electrolyte more than the ionic conductivity), minimizing the electronic conductivity of the electrolyte and by ensuring that the electrolyte is fully dense and that good sealing occurs.

2.4.3. Activation overpotential

Activation overpotential losses are a result of sluggish reaction kinetics on the electrochemically active areas of the electrodes. These activation losses occur because a proportion of the voltage generated is lost to drive the chemical reactions that transfer electrons to or from the electrode. Activation losses can be approximated using Equation 2-4.

$$E_{act} = \left(\frac{RT}{\alpha nF}\right)\ln\left(\frac{i}{i_o}\right) \qquad \text{Equation 2-4}$$

where: α is the charge transfer coefficient (the fraction of electrical energy used to change the rate of the electrochemical reaction)
i_o is the exchange current density (the current that flows equally in the forward and reverse directions at zero overpotential (equilibrium))
n is the number of electrons transferred in the reaction
i is the current density

Activation overpotential losses are highly non-linear and are the dominant type of losses at low current densities. The activation overpotential of the cathode is frequently much higher than the anode since hydrogen electro-oxidation is extremely rapid; however, the strong temperature dependence on the amount of activation overpotential means that even the cathode activation overpotential may be small at high temperatures. Other methods to decrease activation overpotential include: using more efficient catalysts, increasing the surface area of the electrodes, increasing the operating pressure which increases the number of occupied catalyst sites, or by increasing the reactant concentration i.e. using oxygen instead of air as the oxidant.

2.4.4. Ohmic losses

Ohmic losses (E_{iR}) occur as a result of the electrical resistance of the electrodes, interconnects and lead wires and the ionic resistance of the electrolyte. These losses are linear with current density and follow Ohm's law (Equation 2.5).

$$E_{iR} = iR \qquad \text{Equation 2-5}$$

where: i is the current density (A/cm^2)
R is the area specific resistance (the resistance corresponding to 1 cm^2 of the cell)

Ohmic losses can be minimized by increasing the operating temperature, by reducing the electrolyte thickness and by using electrolytes, electrodes, interconnects and lead wires with high conductivity.

2.4.5. Mass transport losses

During fuel cell operation the concentration of reactants will decrease slightly and the concentration of products will increase as reactants are used up and products are produced. As the amount of current being drawn increases, a reactant depletion zone and product build-up zone begin to form. Mass transport losses occur due to the rate at which reactants and products diffuse through the depletion/build-up zone. These losses are also dependent on the physical characteristics of the fuel cell system, i.e., the flow rate of gases, porosity of electrodes, etc. The mass transport losses may be approximated by the following expression:

$$E_{trans} = -\frac{RT}{nF}\ln\left(1-\frac{i}{i_l}\right) \qquad \text{Equation 2-6}$$

where: i_l is a limiting current density at which the fuel is consumed at an equal rate to its maximum supply speed

Mass transport losses are highly non-linear and rapidly drive the voltage to zero at high current densities. Mass transport losses may be eliminated by decreasing the current density. If this is not feasible, mass transport losses can be decreased by increasing the operating temperature and by modifying the physical characteristics of the fuel cell system to enhance the flow of reactants to the electrochemically active area of the electrodes and products away from it.

2.5. Types of fuel cells

There are five main categories of fuel cells. These types are typically differentiated by the type of electrolyte used within the cell. The five main classes of fuel cells are: the Polymer Electrolyte Fuel Cell (PEMFC), the Alkaline Fuel Cell (AFC), the Phosphoric Acid Fuel Cell (PAFC), the Molten Carbonate Fuel Cell (MCFC), and the Solid Oxide Fuel Cell (SOFC). PEMFC may also be run on liquid or gaseous methanol. This type of cell is typically called a Direct Methanol Fuel Cell (DMFC) and may be classified as a sixth major type of fuel cell. Table 2-1 below summarizes the major characteristics of the six main fuel cell types.

Table 2-1: Summary of the Major Characteristics of the Six Types of Fuel Cells

	[illegible]	[illegible]	[illegible]	[illegible]	[illegible]	[illegible]
Operating temperature (°C)	<100	60-120	60-120	160-220	650	600-1000
Anode reaction	$H_2 + 2OH^- \rightarrow 2H_2O + 2e^-$	$H_2 \rightarrow 2H^+ + 2e^-$	$CH_3OH + H_2O \rightarrow CO_2 + 6H^+ + 6e^-$	$H_2 \rightarrow 2H^+ + 2e^-$	$H_2 + CO_3^{2-} \rightarrow H_2O + CO_2 + 2e^-$	$H_2 + O^{2-} \rightarrow H_2O + 2e^-$
Cathode reaction	$\frac{1}{2}O_2 + H_2O + 2e^- \rightarrow 2OH^-$	$\frac{1}{2}O_2 + 2H^+ + 2e^- \rightarrow H_2O$	$\frac{3}{2}O_2 + 6H^+ + 6e^- \rightarrow 3H_2O$	$\frac{1}{2}O_2 + 2H^+ + 2e^- \rightarrow H_2O$	$\frac{1}{2}O_2 + CO_2 + 2e^- \rightarrow CO_3^{2-}$	$\frac{1}{2}O_2 + 2e^- \rightarrow O^{2-}$
Charge carrier in Electrolyte	OH^-	H^+	H^+	H^+	CO_3^{2-}	O^{2-}
State-of-the-art anode material	Carbon with Pt catalyst particles	Carbon with Pt catalyst particles	Carbon with Pt catalyst particles	Carbon with Pt catalyst particles	Cr-Ni-Al alloy	Ni/YSZ cermet
State-of-the-art cathode material	Carbon with Pt catalyst particles	Carbon with Pt catalyst particles	Carbon with Pt catalyst particles	Carbon with Pt catalyst particles	Lithiated NiO	LSM/YSZ
State-of-the-art electrolyte material	35 wt% KOH aqueous solution immobilized in asbestos matrix	Sulfonated PTFE	Sulfonated PTFE	100% H_3PO_4 contained in a SiC matrix	Li/K or Li/Na molten carbonate immobilized in $LiAlO_2$ matrix	YSZ
Applications	Space, transportation	Space, transportation, distributed power, portable power	Portable power	Stationary power	Stationary power	Transportation (APU), distributed power, stationary power

2.5.1. Polymer Electrolyte Membrane Fuel Cell (PEMFC)

Polymer electrolyte membrane fuel cells (also known as proton exchange membrane fuel cells) use a proton conducting polymer membrane as the electrolyte and operate at low temperatures (typically 60-80°C). Typically the electrolyte membrane is made of a sulfonated poly-tetrafluoroethylene (PTFE) structure permeable to protons (H^+ ions) and electrodes consist of well-distributed platinum electrocatalysts deposited on a carbon support. Originally, very high catalyst loadings were required to catalyze the electrode reactions due to the low operating temperatures of PEMFC. Much of the focus of the last 10 years of PEMFC research has been to enhance catalyst activities and reduce catalyst loadings. As a result of this work Pt loadings have been greatly reduced, while maintaining fuel cell performance. Nanocrystalline Pt particles on the carbon support can be seen in the TEM image in Figure 2-8.

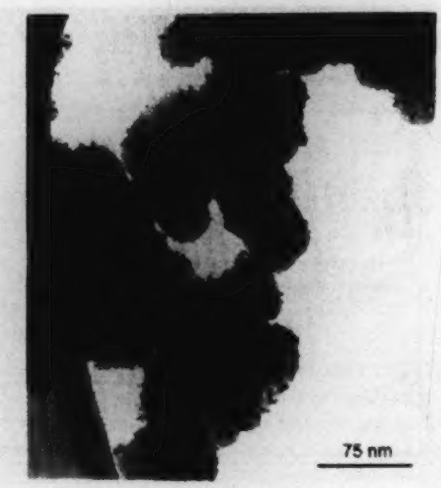

Figure 2-8: TEM image of a fuel cell catalyst. The black dots are the Pt catalyst particles finely distributed over a carbon support. [5]

PEMFC were first developed for the Gemini space program in the 1960's by General Electric and are still used in NASA's current space shuttle (Figure 2-9). Due to the low operating temperature and high power density PEMFC are especially suited for vehicles and for portable applications. However, since the electrolyte is a proton conductor, only fuels that can form H^+ ions, e.g. hydrogen and methanol, can be used as the fuel. PEMFC have significant difficulties with fuel impurities, especially sulfur and carbon monoxide. These additions degrade the performance by poisoning the catalyst; therefore, only very pure fuels may be used for PEMFC systems.

Figure 2-9: Image of a space shuttle launch. PEMFC provide auxiliary power for the shuttle. [6]

2.5.2. Direct Methanol Fuel Cells (DMFC)

Direct methanol fuel cells (DMFC) are closely related to PEMFC. They typically use similar electrolyte and electrode materials, but use a diluted methanol in water mixture as the fuel. Methanol is an attractive fuel since it can be produced from natural gas or from renewable biomass sources; it has a high specific energy density especially compared to hydrogen (due to the fact that it is a liquid under operating conditions) and existing fuel distribution infrastructure could be easily adapted to dispense methanol.

DMFC directly react methanol fuel using the following reactions:

Anode reaction: $CH_3OH + H_2O \rightarrow CO_2 + 6H^+ + 6e^-$ (Reaction 2-2)

Cathode reaction: $\frac{3}{2}O_2 + 6H^+ + 6e^- \rightarrow 3H_2O$ (Reaction 2-3)

DMFC have several challenges that need to be addressed before they can become commercially viable. Better methanol oxidation catalysts need to be developed, as the reaction rates of the Pt catalysts currently used are quite sluggish. The other major problem that needs to be addressed is the methanol crossover. Since methanol has very similar properties to water it may be transported from the anode to the cathode without being oxidized. At the cathode, methanol oxidation interferes with oxygen reduction and thus reduces cell performance.

Due to their compact size and low operating temperature DMFC are very well suited for small portable applications such as cell phones and laptops. Figure 2-10 and Figure 2-11 show two prototype DMFC systems being developed for portable power applications.

Figure 2-10: Portable telephone powered by a DMFC. On the right the removable methanol fuel cartridge may be seen. [7]

Figure 2-11: Prototype DMFC system produced by Smart Fuel Cells to power devices such as laptop computers. [8]

2.5.3. Alkaline Fuel Cell (AFC)

Alkaline fuel cells (AFC) were first developed to produce on-board power for the Apollo space missions in the 1960's and have one of the highest potential efficiencies of all types of fuel cells. These cells use an aqueous alkaline solution as the electrolyte and can use non-precious metal electrodes. The biggest advantage of this system is that the cathode activation overpotential is much lower than for other low temperature acid electrolyte based systems. The following reactions occur in an AFC:

Anode reaction: $2H_2 + 4OH^- \rightarrow 4H_2O + 4e^-$ Reaction 2-4

Cathode reaction: $O_2 + 4e^- + 2H_2O \rightarrow 4OH^-$ Reaction 2-5

It can be seen from the previous reactions that hydroxide ions are consumed and water is produced at the anode. Water is consumed and hydroxide ions are produced at the cathode. These reactions may lead to significant concentration gradients developing in the molten electrolyte. In fact, the electrolyte at the cathode may become so concentrated that it solidifies. These concentration problems are best dealt with by using a mobile electrolyte system design.

The first viable AFC, developed in the 1940's and 1950's by Bacon's group at Cambridge, originally operated at elevated temperatures (~200°C) and high pressures (~4.5 MPa) and used a Ni anode, a lithiated NiO cathode and 30 wt% aqueous KOH electrolyte. Today most systems run at lower temperatures (80-95°C) and pressures (220-400 kPa) and typically use Pt dispersed on carbon electrodes. The electrolyte remains a 35 wt% KOH aqueous solution, although more highly concentrated KOH solutions have also been tested.

The most significant problem with AFC is that the electrolyte reacts with CO_2 in the fuel or the oxidant or there are interactions with the carbon support to form carbonates by the following reaction:

$$CO_2 + 2OH^- \rightarrow (CO_3)^{2-} + H_2O \qquad \text{Reaction 2-6}$$

These reactions gradually replace the hydroxide ions in the electrolyte with carbonate ions, which drastically decreases cell performance. As well, when the carbonate ion concentration increases high enough, carbonate precipitates may form on the electrodes reducing catalyst efficiency and blocking electrode pores.

There are two major designs of AFC currently used: immobilized electrolyte and mobile electrolyte. Immobilized electrolyte designs (Figure 2-12) use a KOH electrolyte immobilized in a porous solid matrix such as asbestos. This design is very simple but makes it very difficult to change the electrolyte solution if it has been poisoned by carbon dioxide. Mobile electrolyte designs (Figure 2-13) incorporate pumps in order to circulate the electrolyte solution throughout the cell. This design greatly increases the cost and complexity of the system, but is advantageous because the circulating electrolyte solution keeps water and hydroxide concentrations much more constant and allows accumulated impurities such as carbonates to be easily removed. The circulated electrolyte can also be used as a cooling liquid to simplify thermal management issues.

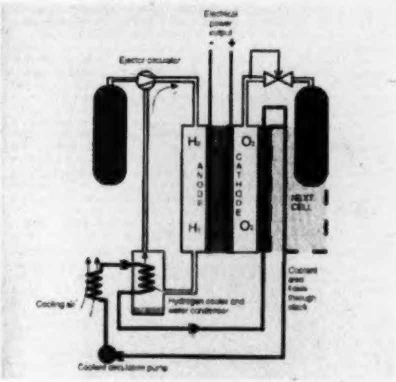
Electrical power output
-
+
Ejector circulator
H_2
ANODE
H_2
O_2
CATHODE
O_2
NEXT CELL
Cooling air
Hydrogen cooler and water condenser
Coolant flows through stack
Coolant circulation pump

Figure 2-12: AFC fuel cell with a static electrolyte contained in a matrix. [5]

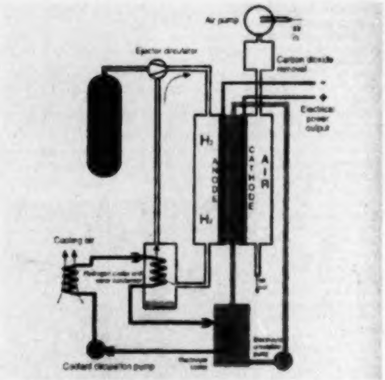
Air pump
Air in
Ejector circulator
Carbon dioxide removal
-
+
Electrical power output
H_2
ANODE
H_2
CATHODE
AIR
Cooling air
Hydrogen cooler and water condenser
Coolant circulation pump

Figure 2-13: Diagram of an AFC with mobile electrolyte. The electrolyte also is used as a coolant. [5]

There was much work being done on AFC in the early to mid 20th century and much success using AFC in the space program. AFC development has slowed down since the 1970's as technical difficulties for terrestrial systems failed to be solved and as PEMFC systems became more and more successful. Currently there is little development activity on AFC systems. Figure 2-14 and Figure 2-15 show two early AFC systems.

Figure 2-14: The world's first fuel cell vehicle (1959) powered by an AFC. [8]

Figure 2-15: The Apollo space capsule orbiting the moon. An AFC provided the on-board power for the capsule. [9]

2.5.4. Phosphoric Acid Fuel Cell (PAFC)

Phosphoric acid fuel cells (PAFC) were the first commercially available fuel cells and many plants, mostly between 50 and 200 kW, have been produced and tested. Some larger scale plants (1, 5 and 11 MW) have also been built. These plants give high power quality, are very reliable and run for commercially viable lifetimes (40000 hours), but are still too costly to directly compete with other power generation systems.

PAFC use an inorganic acid as a proton conducting electrolyte. Concentrated phosphoric acid (100%) is the most commonly used acid as it has good thermal, chemical, and electrochemical stability and low volatility at operating temperatures. The electrolyte is typically contained within a SiC based matrix. The matrix is comprised of SiC particles about 0.1-0.2 µm thick, which is thick enough to have sufficient mechanical strength and to prevent gas crossover, but is thin enough to keep ohmic losses low.

The electrodes and electrocatalysts are very similar to those used by PEMFC and typically consist of very fine Pt particles supported on carbon which is then bonded with PTFE in order to provide an electrode support structure. The carbon helps to disperse the Pt catalyst, provides micropores to enhance gas diffusion and enhances the conductivity of the catalyst. The use of carbon in PAFC electrodes has allowed the Pt catalyst loadings to be drastically reduced. The PTFE in the electrode helps to bind the carbon particles together to form a porous structure. As well, the hydrophobic nature of PTFE helps to prevent the liquid electrolyte from flooding electrode pores.

PAFC are typically operated at 200°C and atmospheric pressure. Higher temperatures and pressures may be used to improve the performance, but corrosion problems become more serious as the temperature and pressure increase. Corrosion also becomes severe at operating voltages greater than ~0.8 V. PAFC are tolerant to CO_2 (unlike AFC), but are still quite susceptible to poisoning by CO and sulfur.

Current PAFC systems have reached a level of maturity. Systems with decent power densities and very low degradation rates (2-4 mV / 1000 hours) have been achieved and there are over 200 PAFC units in the field and many have operated for between 30000 and 40000 hours. Further increases in power density and cost reductions are necessary in order to allow PAFC to achieve economic competitiveness with other energy generation systems. Figure 2-16 shows 5 UTC PAFC systems powering a postal facility in Alaska.

Figure 2-16: Five UTC fuel cell systems powering a postal facility in Alaska. [8]

2.5.5. Molten Carbonate Fuel Cell (MCFC)

Molten carbonate fuel cells (MCFC) are high temperature fuel cells that are being marketed for medium scale power plants (250 kW to several MW). This technology is relatively mature and many units in Europe and the United States are being field tested. The relatively low power density of the cells, highly corrosive nature of the molten carbonate electrolyte and expensive nature of MCFC systems are significant challenges that need to be overcome before a final MCFC product can be commercialized.

The MCFC electrolytes are a molten mixture of alkali metal carbonates which are usually retained within a ceramic $LiALO_2$ matrix. The cells typically operate at a temperature of 650°C which is high enough to melt the electrolyte to form a molten salt containing ionically conductive carbonate ions (CO_3^{2-}), but low enough to use relatively inexpensive metal components.

The following reactions take place at MCFC electrodes:

Anode reaction: $H_2 + CO_3^{2-} \rightarrow H_2O + CO_2 + 2e^-$ Reaction 2-7

Cathode reaction: $\frac{1}{2}O_2 + CO_2 + 2e^- \rightarrow CO_3^{2-}$ Reaction 2-8

From the above reactions it can be seen that carbon dioxide is consumed at the cathode and produced at the anode. Thus there is a net transfer of carbon dioxide from the cathode to the anode and therefore a need for both oxygen and carbon dioxide in the oxidizing gas. The level of carbon dioxide naturally present in air is not sufficient for fuel cell operation; therefore, methods to add carbon dioxide to the oxidizing gas have been developed. Typically the carbon dioxide generated at the anode is recycled externally to the cathode to increase the carbon dioxide content to sufficient levels. The anode exhaust gas is fed through a burner to convert the left over fuel gas to carbon dioxide and water vapour, which is then mixed with fresh air.

The elevated operated temperatures of MCFC are advantageous because they permit non-noble metal catalysts to be used and allow higher system efficiencies and increased fuel flexibility. However, the operating temperature places severe restrictions on the materials used in the cell due to the extremely corrosive nature of the fuel cell environment. The high temperature of operation also means that the polymeric hydrophilic and hydrophobic materials used in lower temperature fuel cells to establish a stable gas/electrolyte interface cannot be used. Thus MCFC must tightly control electrolyte and electrode porosity in order to set up a balance in capillary pressures to establish a good triple phase boundary in the porous electrodes. By properly coordinating the porosity within the electrolyte and electrodes the electrolyte matrix can remain completely flooded with molten carbonate electrolyte while the electrodes remain only partially filled. The small pores within the electrolyte are completely full while the larger pores in the electrodes are only partially filled. A schematic diagram illustrating the different amount of porosity for each MCFC component can be seen in Figure 2-17. The optimization and high level of control over the microstructure and filling of the various fuel cell components is absolutely critical to achieve high performance and durability in MCFC.

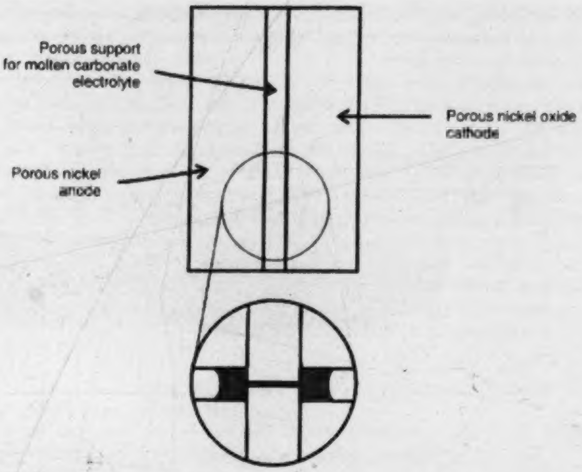
Porous support for molten carbonate electrolyte
Porous nickel oxide cathode
Porous nickel anode

Figure 2-17: Dynamic equilibrium in MCFC elements. The balance in capillary pressures establishes a good triple phase boundary in the porous electrodes. The small pores within the electrolyte are completely full while the larger pores in the electrodes are only partially filled. [5]

The evolution of materials for the MCFC fuel cell has followed the same progression of many other types of fuel cells. In the mid 1960's precious metals were most commonly used as electrodes, but MCFC systems soon evolved to use Ni based alloys for anodes and oxides for cathodes. However, the molten carbonate electrolyte and $LiAlO_2$ electrolyte matrix have remained virtually unchanged throughout MCFC development. Currently state-of-art MCFC electrolytes typically contain about 60 wt% carbonates in a matrix of γ or α $LiAlO_2$. Fibres and particles are frequently used in order to further stabilize the matrix. Typically Li_2CO_3/K_2CO_3 or Na_2CO_3/Li_2CO_3 melts are used as the electrolyte. Li/K electrolytes have higher ionic conductivities, but also more severely degrade electrode materials.

MCFC anodes typically consist of a Cr-Ni-Al alloy typically fabricated by hot powder pressing or by tape casting and sintering. Ten to twenty percent chromium is added to the nickel anode in order to decrease the amount of electrode sintering that occurs during operation; however, Cr tends to react with the molten electrolyte over time increasing the amount of electrolyte loss.

Aluminum additions are thought to increase the creep resistance of the anode and decrease the amount of electrolyte loss possibly by forming a $LiAlO_2$ phase within the Ni particles. Alternate materials such as $LiFeO_2$ and other ceramic oxides are being considered to improve the sulphur tolerance of the electrode. The partial substitution of Ni by Cu is also being investigated in order to reduce electrode costs. Full substitution of Ni by Cu is not feasible due to the low creep resistance of Cu.

The high operating temperature of an MCFC improves the oxygen reduction kinetics sufficiently to enable a lithiated NiO or NiO-MgO ceramic to be active enough to be a good MCFC cathode. Thus the precious metal cathode catalysts required for all lower temperature fuel cell systems are not necessary for MCFC. The only difficulty with NiO cathodes is the small but not negligible solubility of NiO in the electrolyte. When Ni ions dissolve in the electrolyte they tend to diffuse towards the anode and in the more reducing conditions of the anode precipitate out in the electrolyte. These precipitates act as nucleation sites for further precipitates and can cause internal shorts especially if the electrolyte layer is very thin. In order to reduce Ni dissolution the CO_2 partial pressure can be lowered, a more basic electrolyte carbonate can be used, or the thickness of the electrolyte matrix can be increased. Double layer cathodes using doped lithium oxides combined with NiO are also being investigated to increase cathode stability.

MCFC are more tolerant to fuel impurities than lower temperature fuel cells and are able to use both CO and H_2 as a fuel (CO is a poison in all lower temperature fuel cells). Internal reforming of hydrocarbon fuels is possible due to the high operating temperatures, but may require an additional metal catalyst and some method to control carbon formation.

MCFC systems are beginning to reach maturity. Companies such as Fuel Cell Energy, Ishikawajima-Harima Heavy Industries and MTU are actively field testing pre-commercial systems; however, costs must be drastically reduced and power densities increased before a commercially viable system can be marketed. Figure 2-18 shows two MCFC systems currently being field tested.

Figure 2-18: MCFC field trials are underway. Left: 300kW biogas-fuelled system built by Ishikawajima-Harima heavy industries. Right: A 250kW MTU unit. [10]

2.5.6. Solid Oxide Fuel Cells (SOFC)

Solid oxide fuel cells are an all solid-state device that uses an oxide ion conducting ceramic as the electrolyte. These fuel cells are much simpler than all other types of fuel cells because there are only two phases involved (gas and solid). Since there are no liquid phases, SOFC do not have the electrolyte management problems that liquid electrolyte fuel cell systems such as AFC, PAFC and MCFC experience or the water management issues that cause DMFC and PEMFC difficulties. The high temperature of SOFC operation (600 to 1000°C) enables non-precious metal electrocatalysts to be used and makes internal reforming of hydrocarbon fuels possible. SOFC electrolytes are oxygen ion conductors and therefore can use both H_2 and CO as fuels, but no extra carbon dioxide is required as is the case with MCFC, which simplifies the system configuration.

The most commonly used SOFC electrolyte material is yttria stabilized zirconia (YSZ). Yttria (Y_2O_3) is added to zirconia (ZrO_2) to enhance the ionic conductivity and stability by increasing the number of oxygen ion vacancies and by stabilizing the cubic phase. Other dopants such as scandia (Sc_2O_3) can be used in order to increase zirconia's ionic conductivity, but typically are more expensive than yttria. Lower temperature SOFC (650-750°C) often use electrolyte materials with higher inherent ionic conductivities such as samaria or gadolinia doped ceria

(SDC or GDC) or lanthanum gallates typically doped with strontium and magnesium (LSGM – $(La, Sr)(Ga, Mg)O_3$), but these materials have stability and compatibility issues.

Anode materials have been relatively constant throughout recent SOFC development. The most commonly used SOFC anode material consists of a cermet of Ni and YSZ. The Ni component of the anode is mainly used to catalyze the hydrogen reduction reaction and provide electrical conductivity while the YSZ component is mainly used to modify the thermal expansion coefficient to better match the electrolyte and to inhibit Ni sintering. Ni is chosen as the metallic component because it has excellent catalytic activity, electrical conductivity, and mechanical properties, and is relatively inexpensive.

The most commonly used SOFC cathode material is strontium doped lanthanum manganite (LSM). LSM is stable in oxidizing atmospheres, has sufficient electronic conductivity at high temperatures and has a similar thermal expansion coefficient to YSZ. At high temperatures (>1200°C), however, LSM reacts with YSZ to form a poorly conducting $La_2Zr_2O_7$ phase. Other higher performance cathode materials are being developed, but these materials frequently have compatibility issues with YSZ or are not very stable.

Significant progress is being made toward commercialization of SOFC for large scale power plant and distributed generation applications. Major players such as Siemens-Westinghouse and Sulzer-Hexis are aggressively field testing prototype systems. One of Sulzer-Hexis' field test systems, the HXS 1000, is shown in Figure 2-19. The American Department of Energy has committed significant resources to push forward SOFC commercialization through the Solid State Energy Conversion Alliance (SECA) program and many companies in Canada, the United States, Europe and Japan are actively working to develop commercially viable SOFC systems.

Figure 2-19: HXS 1000 premiere SOFC system produced by Sulzer-Hexis. This system produces an electrical output of 1 kW and thermal output 2.5 kW. It is meant to cover basic heat and electricity demands for a single family home. The heat produced is used for both heating the home and providing hot water. Many of these units are presently being field tested. [11]

2.6.Fuel cell applications

Although the concept of fuel cells has been demonstrated since the mid 1800's, the modern history of the fuel cell really did not really begin until the 1950's. It was in the 1950's when fuel cells first began to be incorporated into integrated systems as the power source. There have been more than 6800 fuel cell systems [10] built since the 1950's; however, the number of systems being tested did not really take off until the year 2000 as can be seen in Figure 2-20.

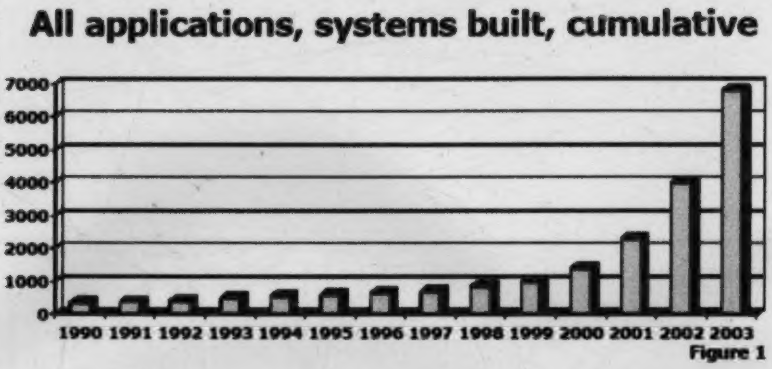

Figure 2-20: Cumulative number of fuel cell systems built worldwide from 1990 to 2003. [10]

Before 1990, there were very few fuel cell systems built and the vast majority of system work involved the fuel cells powering the NASA spacecraft. After 1990, fuel cells began to be utilized in other areas including automobiles and buses and in stationary power. It was in the early 1990's that Ballard began early testing of their PEM bus systems and UTC Fuel Cells began to sell a 200kW PAFC stationary power system. After the year 2000 the number of fuel cell systems being tested began to accelerate rapidly and this number is growing every year. Currently there are four main areas that fuel cells are considered especially well suited for: stationary power, distributed generation, transportation, and small-scale portable power. Most fuel cell systems are being developed for one or more these applications. The unique requirements of each power generation application means that certain fuel cells are more appropriate for use in each situation.

2.6.1. Stationary power plants (>10kW)

Development work on stationary power (>10kW) fuel cell systems started in the 1960's and over 600 systems have been commissioned worldwide [10]. Initially this area was dominated by PAFC and UTC Fuel Cells sold the first commercially available fuel cell system in the early 1990's. More recently, however, higher temperature fuel cell systems based on SOFC or MCFC technology have become more common. Higher temperature fuel cells are particularly attractive for these applications because of their ability to use hydrocarbon fuels and high operating temperatures, which allows the system efficiency to be increased by using the excess heat for applications such as co-generation. Major stationary power developers include MCFC companies, such as Fuel Cell Energy, Ishikawajima Heavy Industries and MTU Friedrichsafen and SOFC developers, such as Mitsubishi Heavy Industries, Rolls Royce, and Siemens Westinghouse. Figure 2-21 shows a prototype 220kW SOFC/gas turbine hybrid system developed by Siemens-Westinghouse.

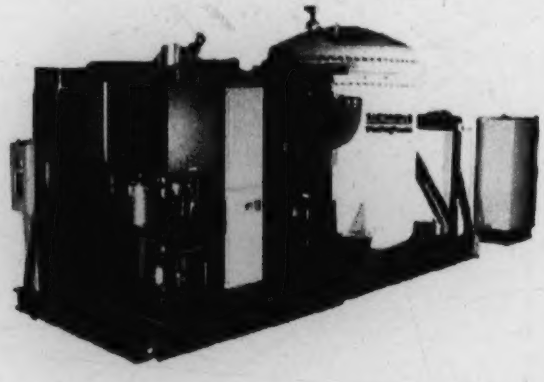

Figure 2-21: 220kW SOFC/gas turbine hybrid system developed by Siemens-Westinghouse. The system is being tested at Irvine's National Fuel Cell Research Center and has demonstrated electrical efficiencies of 53%. [12]

2.6.2. Distributed generation (<10kW)

There have been many smaller scale (<10kW) systems built to provide residential power, high quality backup power or distributed generation. Recently there has been more and more interest in distributed power generation. Distributed power generation systems create a large network of smaller generation sites located closer to the end user of the power rather than the traditional method of having a few large capacity power plants and a grid network to distribute the power. Distributed power reduces the capital costs for the electricity providers and improves overall plant efficiency by improving the ability to cogenerate electricity and heat. As worldwide concerns about the environment and the overdependence of the industrialized world on fossil fuels continues to grow, fuel cells will become a more and more attractive option to provide dependable, efficient distributed power without contributing poisonous emissions into the environment. All types of fuel cells could be used for distributed power systems and traditionally PEMFC systems dominated this sector. However, higher temperature SOFC systems are beginning to make more of an impact in this area. High temperature fuel cells are attractive due to their ability to use hydrocarbon fuels and their high operating temperatures, which allow the high quality byproduct heat to be used with gas turbines, for cogeneration, or to provide heat for endothermic fuel reforming processes. Major companies working in this sector include: Plug Power, Fuel Cell Technologies Ltd, Sulzer-Hexis and Fuel Cell Energy Ltd. (formerly Global Thermoelectric). Figure 2-22 shows a Plug Power PEMFC demonstration system that provides power for a McDonalds outlet in Long Island, USA.

Figure 2-22: A 5kW Plug Power PEMFC system that provides power at a McDonalds outlet in Long Island, USA. [10]

2.6.3. Transportation

Transportation applications are potentially the biggest market for fuel cells. Since the world's first fuel cell vehicle was showcased in 1959, fuel cells have been used to provide primary or auxiliary power for transportation applications varying from bicycles to buses and automobiles and even spacecraft. Ballard and PEM fuel cells have been at the forefront of this area for many years. PEMFC are particularly suited for transportation applications, since their low temperature of operation makes rapid start up and thermal cycling easy compared to higher temperature fuel cell systems. However, PEMFC need for expensive catalysts and water management issues, especially dealing with operating conditions below 0°C,are difficult problems that must be solved. However, the biggest challenge for PEMFC transportation systems to overcome may be the requirement of PEMFC for impurity free hydrogen as fuel. Critical problems like economical hydrogen generation, distribution and storage have still not been solved. The solution to these problems must be achieved before widely available commercial PEMFC vehicles are feasible. Figure 2-23 shows the well-to-wheels energy efficiency for fuel cell powered vehicles compared to internal combustion engines and other types of vehicle propulsion units. It can be seen from the figure that while fuel cells themselves are quite efficient the fuel chain to produce hydrogen is not nearly as efficient, drastically decreasing the overall efficiency of hydrogen fueled fuel cell vehicles.

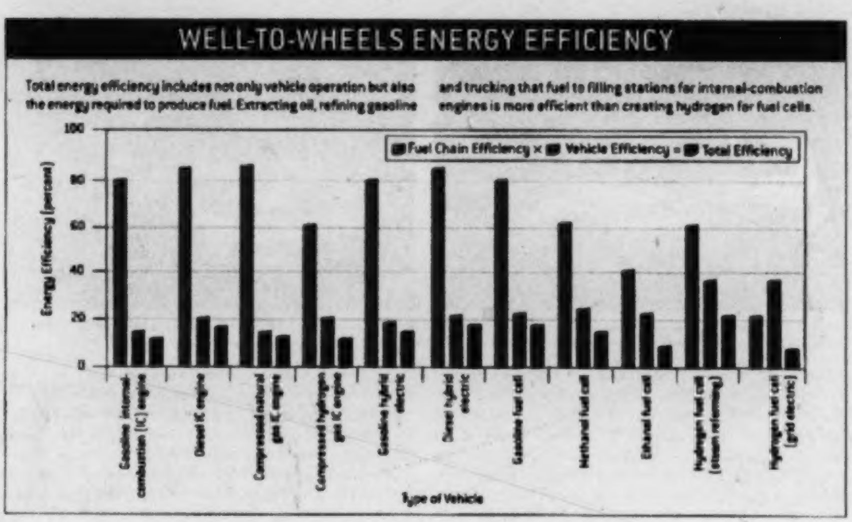

Figure 2-23: Chart of well-to-wheels energy efficiency. [13]

There have been many PEMFC powered buses field tested and it is perhaps in niche areas, such as buses and taxi fleets, where fuel cell powered vehicles will first appear. In 2003 thirty Daimler Chrysler Citaro fuel cell buses were delivered for testing in a number of European cities.

The vast majority of automotive companies are developing fuel cell powered prototype vehicles and five major automotive companies (Daimler Chrysler, Ford, Honda, Nissan and Toyota) have begun field trials of production ready prototype systems. These vehicles are leased or sold to real customers to provide the most realistic testing conditions. Daimler Chrysler plans to build between 50000 and 100000 fuel cell vehicles between 2005 and 2010 and by 2030 a production target of over 50 million total fuel cell powered vehicles (10% of the global market) is forecast. Finally, ship builders, especially the US Navy are considering SOFC systems to provide cleaner, more efficient ship propulsion systems. Figure 2-24 and Figure 2-25 show two PEMFC powered vehicles currently being field tested.

SOFC are also being considered as alternative power units (APU) for vehicles. These systems would run on gasoline and would run the parasitic electrical systems such as air conditioning. SOFC are particularly suited for this application due to their high power density and ability to use gasoline as fuel.

Figure 2-24: Daimler Chrysler Citaro fuel cell bus. Thirty of these buses will be delivered to 10 European cities in 2003 for a two year demonstration project. [14]

Figure 2-25: Necar (New Electric Car) 4 produced by Daimler Chrysler. This car is completely powered by a PEMFC system and uses liquid hydrogen fuel. [15]

2.6.4. Small scale portable power (1W to 1.5kW)

Small scale portable fuel cell systems are the fastest growing fuel cell sector. In fact, there are more companies actively developing portable power fuel cell systems than any other application. These systems will directly compete with batteries for portable applications such as cell phones and laptops. Fuel cells systems such as PEMFC and especially DMFC are attractive for these applications, because they can provide higher power densities than batteries and instant recharging. Battery life would then only be limited by the size of the fuel tank and recharging would be instantaneous simply by replacing the fuel cartridge rather having to wait while the battery recharges. It is easy to see why a technology that gives three to five times greater battery life and a recharge time of seconds would be exciting. Companies such as Ball Aerospace, Ballard and Smart Fuel Cells have already begun production and limited marketing of portable systems. NEC, Hitachi and Toshiba have demonstrated the fuel cell powered laptops which may be commercially available as early as 2005. A prototype DMFC powered laptop system produced by NEC is shown in Figure 2-26.

Figure 2-26: Prototype DMFC powered laptop produced by NEC. Commercially available fuel cell powered laptop systems are expected to go on sale in 2005. [10]

2.7.Summary

Fuels cells are an energy generation technology that cleanly and efficiently produce electricity through an electrochemical reaction. Although the original concept of a fuel cell was first developed in the mid 1800's they are only now beginning to be developed for commercial applications. There are six main types of fuel cells currently being developed for many different applications.

The remaining portion of this thesis will concentrate on one particular type of fuel cell, solid oxide fuel cells (SOFC). SOFC operate at elevated temperatures (600 to 1000°C) and have many advantages over other types of fuel cells including: excellent efficiency, high grade byproduct heat, all solid-state construction, greater tolerance to fuel impurities and the ability to operate on hydrocarbon fuels. However, the high temperature of operation also means that there are many challenges that need to be solved before SOFC systems can be commercialized. Chapter 3 will provide more background into SOFC materials and design and into some of challenges that need to be solved before commercialization can occur.

2.8. Bibliography

A.S. Arico, S. Srinvasan, V. Antonucci, *Fuel Cells*, **1** (2001) 133.

N.P. Brandon, S. Skinner, B.C.H. Steele, *Annu. Rev. Mater. Res.* **33** (2003) 183.

L. Carrette, K.A. Friedrich and U. Stimming, *Fuel Cells*, **1** (2001) 5.

Chen Chen, *MSc Thesis, University of Virginia*, (2003).

M. Cropper & D. Jollie, "Fuel Cell Systems: A Survey of Worldwide Activity", *Fuel Cell Today*, Nov 14, 2002. Retrieved June 1, 2004 from the World Wide Web: http://www.fuelcelltoday.com/FuelCellToday/FCTFiles/FCTArticleFiles/Article_528_WorldwideSurvey1102.pdf

M. Cropper, S. Geiger & D. Jollie, "Fuel Cell Systems: A survey of worldwide activity", *Fuel Cell Today*, November 5, 2003. Retrieved June 1, 2004 from the World Wide Web: http://www.fuelcelltoday.com/FuelCellToday/FCTFiles/FCTArticleFiles/Article_696_WorldWideSurvey1103.pdf

M. Cropper, S. Geiger, D. Jollie, *Journal of Power Sources*, **131** (2004) 57.

B. de Boer, *PhD Thesis, University of Twente*, (1998).

R. Dillon, S. Srinivasan, A.S. Arico, V. Antonucci, *Journal of Power Sources*, 127 (2000) 112.

G. Friedlmeir, J. Friedrich, F. Panik, *Fuel Cells*, **1** (2001) 92.

Fuel Cell Handbook, 6th ed., EG&G Technical Services Inc., 2002.

S. M. Haile, *Acta Materialia*, **51** (2003) 5981.

K. Hassmann, *Fuel Cells*, **1** (2001) 78.

M.J. Jorgensen, S. Primdahl, C. Bagger, M. Mogensen, *Solid State Ionics*, **139** (2001) 1.

K Kieveland, M. Einarsrud, C.R. Schmidt, S. Shamsili, S. Faaland, K. Wiik, T. Grande, *Journal of the American Ceramic Society*, **82** (1999) 729.

L. Kindermann, D. Das, D. Bahadur, R. Weiss, H. Nickel and K. Hilpert, Journal of the American Ceramic Society, 80 (1997) 909.

P. Lamp, J. Tachtler, O. Finkenwirth, S. Mukerjee, S. Shaffer, *Fuel Cells*, **3** (2002) 146.

J. Larminie and A. Dicks, *Fuel Cell Systems Explained*, John Wiley & Sons Ltd., West Sussex, England, 2000.

V. Mehta and J.S. Cooper, *Journal of Power Sources*, **114** (2003) 32.

N. Minh and T. Takahashi, *Science and Technology of Ceramic Fuel Cells*, Elsevier Science, Amsterdam, The Netherlands, 1995.

H. Mobius, *Journal of Solid State Electrochemistry*, **1** (1997) 2.

R. M. Ormerod, *Chem. Soc. Rev.*, **32** (2003) 17.

F. Preli, *Fuel Cells*, **2** (2002) 5.

S. Primdahl, *PhD Thesis, University of Twente*, (1999).

S.C. Singhal, *Solid State Ionics*, **152-153** (2002) 405.

M. L. Wald, *Scientific American*, **5** (2001) 66.

A. Weber and E. Ivers-Tiffee, *Journal of Power Sources*, **127** (2004) 273.

K. Wiik, C.R. Schmidt, S. Faaland, S. Shamsili, M. Einarsrud, T. Grande, *Journal of the American Ceramic Society*, **82** (1999) 721.

M. C. Williams, *Fuel Cells*, **1** (2001) 87.

M.C. Williams, J.P. Strakey, S.C. Singhal, *Journal of Power Sources*, **131** (2004) 79.

2.9 References

1 L. Carrette, K.A. Friedrich and U. Stimming, *Fuel Cells*, **1** (2001) 5.

2 H. Mobius, *Journal of Solid State Electrochemistry*, **1** (1997) 2.

3 Solid State Energy Conversion Alliance website. Retrieved June 14, 2004 from the World Wide Web: http://www.seca.doe.gov

4 Retrieved June 1, 2004 from the World Wide Web: http://www.globalte.com

5 J. Larminie and A. Dicks, *Fuel Cell Systems Explained*, John Wiley & Sons Ltd., West Sussex, England, 2000.

6 Retrieved June 1, 2004 from the World Wide Web: http://pilotweather.topcities.com/space-shuttle-launch3a.jpg

7 S. Valette, "Miniature fuel cells", *Cleff CEA*, **44**, Winter 2000-2001. Retrieved June 1, 2004 from the World Wide Web: http://www.cea.fr/gb/publications/Clefs44/an-clefs44/clefs4445a.html

8 Mark Cropper & David Jollie, "Fuel Cell Systems: A Survey of Worldwide Activity", *Fuel Cell Today*, Nov 14, 2002. Retrieved June 1, 2004 from the World Wide Web: http://www.fuelcelltoday.com/FuelCellToday/FCTFiles/FCTArticleFiles/Article_528_WorldwideSurvey1102.pdf

9 Retrieved June 1, 2004 from the World Wide Web: http://www.iol.ie/~jordane/aviation/images/space/apollo_csm.jpg

10 Mark Cropper, Stefan Geiger & David Jollie, "Fuel Cell Systems: A survey of worldwide activity", *Fuel Cell Today*, November 5, 2003. Retrieved June 1, 2004 from the World Wide Web: http://www.fuelcelltoday.com/FuelCellToday/FCTFiles/FCTArticleFiles/Article_696_WorldWideSurvey1103.pdf

11 Retrieved June 1, 2004 from the World Wide Web: http://www.sulzer.com/map/SulzerDocuments/DocumentsImages/Images/Hexis/HX_BMK02_1.jpg

12 Retrieved June 1, 2004 from the World Wide Web: http://www.powergeneration.siemens.com/en/fuelcells/demo/index.cfm?session=3123775x39956396

13 M. L. Wald, *Scientific American*, **5** (2001) 66.

14 Retrieved August 29, 2004 from the World Wide Web: http://www.daimlerchrysler.com/dccom/0,,0-5-7145-1-9433-1-0-0-0-0-0-13-0-0-0-0-0-0-0,00.html

15 Thierry Alleau and Isabelle Dumas, "The fuel cell: a solution for energy and environmental concerns" *Cleff CEA*, No. 44, Winter 2000-2001. Retrieved June 1, 2004 from the World Wide Web: http://www.cea.fr/gb/publications/Clefs44/an-clefs44/clefs4440a.html

Chapter 3: Solid Oxide Fuel Cells (SOFC)

Abstract

Solid oxide fuel cells (SOFC) use a solid, ionically conductive ceramic oxide as the electrolyte. The low inherent ionic conductivity of the electrolyte material means that SOFC must be operated at elevated temperatures usually between about 600°C and 1000°C. High operating temperatures give SOFC several advantages over other types of fuel cells such as the ability to use high grade byproduct heat for cogeneration, the capacity for direct internal reforming of hydrocarbon fuels and a lack of requirements for noble metal catalysts. However, the high operating temperatures limit material selection choices, complicate thermal cycling issues and make commercially viable fuel cell lifetimes difficult to achieve.

There are presently two main types of SOFC designs being developed: tubular and planar. However, the majority of SOFC developers are focussing on the planar design, which is easier to fabricate and promises higher power densities.

SOFC electrolytes are typically made of yttria-stabilized zirconia (YSZ), which has adequate ionic conductivity at high temperatures or for very thin layers. Many new lower temperature SOFC electrolyte materials such as doped ceria or lanthanum gallates are being developed. SOFC interconnects may be formed from ceramic or metallic materials depending on the cell operating temperature. Anode materials are typically cermet mixtures of Ni and YSZ while the most common cathode material is strontium doped lanthanum manganite (LSM).

Chapter 3: Solid Oxide Fuel Cells (SOFC) 3-1

List of Figures 3-3

3. Solid Oxide Fuel Cells (SOFC) 3-4
  3.1. Advantages of SOFC 3-4
  3.2. Challenges in SOFC 3-5
  3.3. Cell Design 3-7
    3.3.1. Tubular 3-7
    3.3.2. Planar 3-11
  3.4. SOFC Components 3-14
    3.4.1. Electrolytes 3-14
    3.4.2. Interconnects 3-18
    3.4.3. Seals 3-20
    3.4.4. Cathodes 3-22
    3.4.5. Anodes 3-23
  3.5. Scope of Thesis 3-31
  3.6. Summary 3-32
  3.7. Appendices 3-35
    3.7.1. Appendix 3-1: Bulk volume changes for Ni samples. 3-35
    3.7.2. Appendix 3-2: Redox depth calculations 3-36
  3.8. Bibliography 3-38
  3.9. References 3-42

List of Figures

Figure 3-1: Cell-to-cell connections in a tubular SOFC stack 3-8
Figure 3-2: Schematic diagram of a tubular SOFC 3-9
Figure 3-3: Anode supported flat tube cells.. 3-10
Figure 3-4: SEM micrograph of a micro-tubular SOFC LSM cathode support tube 3-11
Figure 3-5: SEM micrograph of a micro-tubular SOFC................................. 3-11
Figure 3-6: Image of a planar anode supported SOFC 3-12
Figure 3-7: Typical microstructure of an anode supported SOFC.................. 3-12
Figure 3-8: Typical microstructure of an electrolyte supported SOFC 3-12
Figure 3-9: Polished cross-section of an interconnect supported SOFC 3-13
Figure 3-11: Ionic conductivity of various high temperature ionic conductors 3-17
Figure 3-12: SEM image of the anode functional layer anode substrate.......... 3-25

3. Solid Oxide Fuel Cells (SOFC)

Solid oxide fuel cells (SOFC) utilize a solid, ionically conducting ceramic oxide as an electrolyte. Due to the inherently low ionic conductivity of the solid electrolytes, SOFC must be operated at elevated temperatures that usually range between 600°C and 1000°C. High operating temperatures and all solid-state construction are the two most distinguishing features of SOFC.

3.1. Advantages of SOFC

SOFC have many advantages over other types of fuel cells. They have one of the highest efficiencies of all types of fuel cells. This efficiency is increased even higher when the high grade byproduct heat produced by SOFC is used by gas turbines, for cogeneration, or to provide heat for endothermic fuel reforming processes. SOFC also have a relatively high power density, which enables compact designs to give excellent power outputs.

Another significant advantage of SOFC is that they can utilize both hydrocarbon and hydrogen based fuels, because the electrolyte material conducts oxide ions (O^{2-}) rather than hydrogen ions (H^+). As a result, a SOFC can use CO as fuel rather than being poisoned by it, as is the case for PEMFC, DMFC, AFC, and PAFC. SOFC also exhibit a higher tolerance to fuel contaminants such as sulphur than other types of fuel cells.

The elevated operating temperature of an SOFC provides several more competitive advantages over other fuel cell types. The heat allows the internal reformation of hydrocarbon fuels, which removes the requirement for complicated, and expensive external fuel reformers. As well, elevated temperatures allow non-noble metal catalysts such as nickel to be used.

The final important advantage SOFC have over other types of fuel cells is an all solid-state construction. Since the electrolyte is solid, corrosion problems that occur in liquid systems such as MCFC are not present. Water management, catalyst layer flooding and slow oxygen reduction kinetics difficulties seen in PEMFC are not a problem due to the fact that SOFC are a two phase (gas-solid) system. The all solid-state construction also allows cell components to be fabricated into thin layers to minimize resistive losses and unique shapes that are unachievable in liquid electrolyte systems.

3.2. Challenges in SOFC

The high operating temperature of SOFC is a benefit, but it also presents one of the most significant challenges especially when considering that 40000 hours is the typical operating lifetime goal for commercial SOFC systems. [1] It is very difficult and expensive to find materials that have the necessary thermal properties and that are sufficiently stable at SOFC operating temperatures over such a long lifetime. Volume changes induced by slight thermal expansion coefficient mismatches between components or due to reduction/oxidation (redox) processes can cause significant stresses to build up at cell operating temperatures or after thermal or redox cycles. These stresses may cause cell interfaces to delaminate, which increases contact resistances, or they may even fracture the electrolyte causing internal shorts and gas leakage. During heat up and operation non-uniform temperature gradients can also occur due to the poor thermal conductivity of the ceramic cell components. One way to minimize some of the thermal stresses is to heat the cell to working temperatures over a relatively long period of time; however, for some applications, such as transportation, long start-up times are not feasible.

The high operating and fabrication temperatures may also cause stability issues for cell components. Doped lanthanides that are commonly used as cathode or interconnect materials are frequently only metastable phases and thus may form undesirable insulating phases. Nickel used in the anode will sinter at operating temperatures, which coarsens the microstructure and degrades the electrochemical performance by reducing the triple phase boundary area. Interconnect materials that contain chromium such as stainless steels, may also be unstable. At operating temperatures, some of the chromium may vaporize from the interconnect and deposit on the cathode which degrades the electrochemical performance by blocking sites on the triple phase boundary. As well, the growth of oxide scales on metallic interconnects may greatly increase the contact resistance between the cathode and the interconnect.

Another SOFC challenge is the contact made between each component. As cell fabrication methods improve and cell layers decrease in thickness the corresponding layer resistance losses decrease. As a result, losses due to poor contact between layers become more important and may even become the predominant type of losses during fuel cell operation. Contact may also degrade over time if cell components react with each other or if delamination of fuel cell layers occurs.

The choice of fuels also presents both an impressive opportunity and challenge for SOFC systems. The high operating temperatures and ability of SOFC to use carbon monoxide as a fuel give SOFC vastly superior fuel flexibility than other types of fuel cells. SOFC can directly use hydrogen or hydrocarbon based fuels and both internal reforming or direct oxidation of hydrocarbon fuel gases is possible. Pure hydrogen may be used with few problems in SOFC, but until major issues in hydrogen production and storage are addressed it is not practical to assume that hydrogen will be the most common fuel for any fuel cell, especially SOFC. Hydrocarbon fuels are much more likely to be the fuel of choice since they are readily available and a well established production, storage and distribution infrastructure is already in place.

There are two major issues that need to be addressed if hydrocarbon fuels are used for SOFC: carbon deposition on the anode and fuel impurities. If the operating conditions are not strictly controlled, internal reforming and direct oxidation may cause carbon to be deposited on the anode. This deposition blocks electrochemically active sites and thus reduces anode performance. Impurities commonly present in hydrocarbon fuels such as sulphur act as poisons in SOFC and reduce performance. Although SOFC are much more tolerant of fuel poisons than other types of fuel cells, significant work still needs to be done to increase SOFC poison tolerance.

3.3. Cell Design

There are two major SOFC cells designs that are currently being developed: tubular and planar. Each design has advantages and disadvantages and hybrid tubular/planar designs are also being developed in order to capitalize on the advantages of both primary SOFC designs.

3.3.1. Tubular

Tubular SOFC designs were the first type of SOFC to be extensively investigated and are now are almost universally linked to the many years of SOFC development work that have been performed by Siemens-Westinghouse. The major advantage of the tubular design is that it is mostly self-sealing and the few seals that are required can be moved out of the hot zone of the fuel cell. Tubular designs are much more mechanically robust than planar designs, which enhances their thermal cycling abilities, and long term degradation rates of tubular SOFC are lower. However there are several disadvantages inherent in a tubular design. Cell fabrication is more complicated and expensive due to the geometry of the system and tubes don't stack into fuel cell stacks nearly as well as planar cells (Figure 3-1). However, the most significant disadvantage is that the current path and electrolyte thickness in tubular cells is typically much larger than in planar cells. Therefore, resistive losses are typically much higher. These higher resistive losses force tubular designs to operate at very high temperatures (~1000°C).

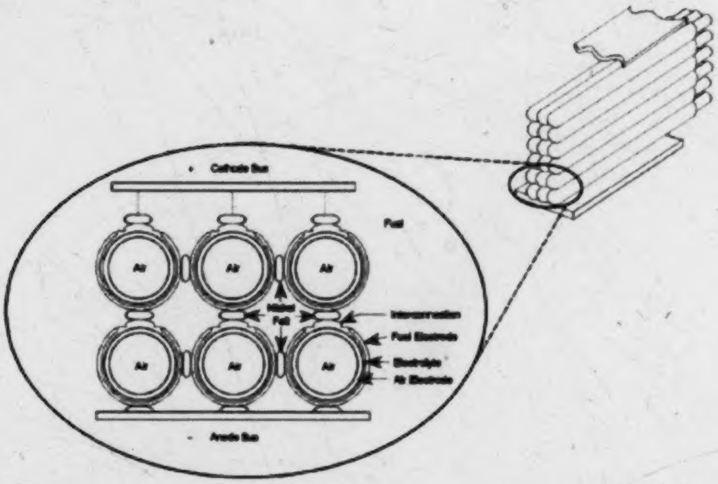
+ Cathode Bus
Fuel
Air
Nickel Felt
Interconnection
Fuel Electrode
Electrolyte
Air Electrode
- Anode Bus

Figure 3-1: Cell-to-cell connections in a tubular SOFC stack. [2]

The original Siemens-Westinghouse tubular design deposited fuel cell layers on a porous zirconia support tube with one closed end using electrochemical vapour deposition (EVD). Recent progress has allowed the support tube to be eliminated and a cathode supported design has been developed. The YSZ electrolyte is deposited on an extruded LaMn cathode support tube using EVD while the Ni/YSZ anode is deposited using plasma spraying. Typical tubular cells are greater than 2 cm in diameter and over 150 cm long. Fuel flows along the outside of the tube while air is fed inside the tube through a small alumina supply tube centrally located within each fuel cell tube in order to ensure that air penetrates all the way to the closed end of the tube. A schematic diagram of a tubular SOFC is shown in Figure 3-2.

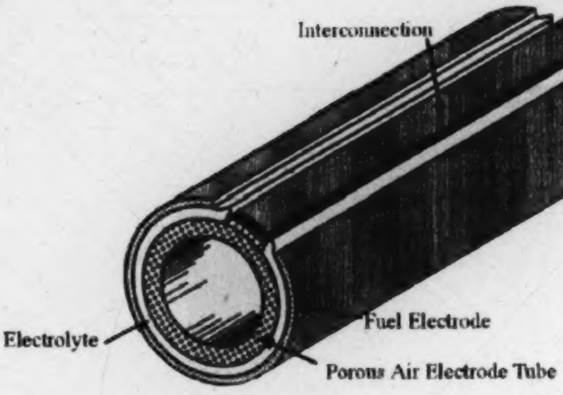
Interconnection
Fuel Electrode
Electrolyte
Porous Air Electrode Tube

Figure 3-2: Schematic diagram of a tubular SOFC. [3]

One innovative method to reduce the amount of resistive losses that occur with a tubular design is to use a flattened tubular design. Kim et al. have produced a flat NiO/YSZ tube with interior ribs by an extrusion process (Figure 3-3). This configuration has the increased thermal stability and sealless design of tubular systems, and has the high power density and short conduction path provided by electronic conduction through the central ribs of a planar cell.

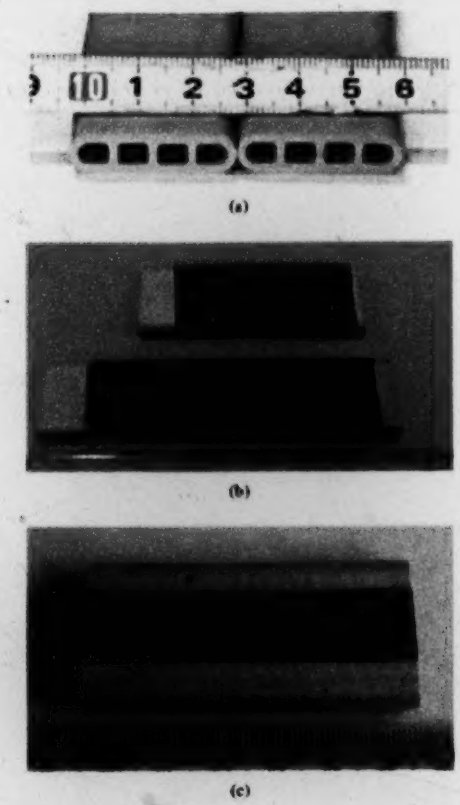

(a)

(b)

(c)

Figure 3-3: Anode supported flat tube cells: (a) as-extruded and pre-sintered anode supported flat tube (b) flat-tube cell coated with electrolyte and cathode layer (c) flat-tube cell coated with electrolyte and plasma spray-coated interconnect layer. [4]

A micro-tubular SOFC design attempts to utilize the excellent mechanical properties and minimal sealing requirements of a tubular design and to improve the power density by minimizing the tube diameter, which increases the electrolyte surface area per volume in a stack. Tubes with a diameter on the order of several mm are typically used and anode, cathode and electrolyte supported designs have all been developed. The functional layers are typically deposited on the extruded support tube using electrophoretic deposition. The biggest advantage of this design is that it has excellent thermal and mechanical stability. A study by Prica et al. heated a 200 tube micro-tubular stack to 800°C at a heating rate of 200°/min and then rapidly thermal cycled the cells 50 times without any failures. [5] The ability to survive rapid heat-ups and thermal cycling combined with the higher power density means that this type of SOFC may be able to compete with lower temperature fuel cells for transportation applications.

Figure 3-4: SEM micrograph of a micro-tubular SOFC LSM cathode support tube. [6]

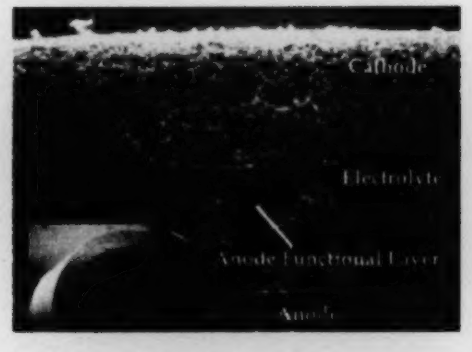

Figure 3-5: SEM micrograph of a cross-sectional fracture surface of a micro-tubular SOFC. [7]

3.3.2. Planar

Planar cell designs are cheaper, easier to fabricate and have vastly higher power densities than tubular designs; however, large areas of the cell and manifold require high temperature seals and thermal cycling is frequently a problem. Despite these challenges the majority of worldwide SOFC developers are developing the planar design shown in Figure 3-6.

Figure 3-6: Image of a planar anode supported SOFC. [8]

Planar designs typically have one thicker layer that provides the mechanical support and provides a base for the other layers to be deposited onto. Cells may be anode, cathode, electrolyte, or interconnect supported. Originally many cell designs were electrolyte supported in order to ensure that the electrolyte was fully dense; however, many developers have moved to an anode supported design in order to minimize the ohmic losses caused by the electrolyte by minimizing the electrolyte thickness. SEM images of anode supported and electrolyte supported cells are shown in Figure 3-7 and Figure 3-8.

cathode
electrolyte
anode functional layer
anode substrate

Figure 3-7: Typical microstructure of an anode supported SOFC. [9]

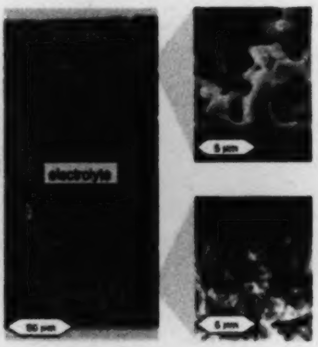

Figure 3-8: Typical microstructure of an electrolyte supported SOFC. [10]

In order to lower long term degradation rates and to allow more inexpensive materials to be used, most planar SOFC developers have attempted to lower operating temperatures. Several groups have begun to work on a cell design that is supported by a metallic interconnect (usually ferritic stainless steel) which will run at very low temperatures (500 to 650°C). [11,12] The stainless steel supported cell is more tolerant to redox cycling because there is no thick Ni anode support to oxidize, has better thermal conductivity which reduces thermal gradients in the cell, and is much stronger and tougher than cermet or ceramic supported cells. However, the metallic substrate ultimately limits the maximum operating temperature of the fuel cell system since most metals are not stable at very high temperatures. Metallic substrates are also cheaper than the Ni/YSZ cermet substrate currently being used and allow conventional low cost metal fabrication and joining techniques such as welding to be used. An SEM image of an interconnect supported SOFC is shown in Figure 3-9.

Contact layer
Cathode
Electrolyte
Anode
Steel substrate

Figure 3-9: Polished cross-section of a metal (interconnect) supported SOFC. [12]

Tubular and planar SOFC designs have both significant advantages and challenges. Tubular designs tend to be more stable both from both a long term degradation point of view and a thermal cycling viewpoint and have minimal high temperature sealing requirements. However, the high resistive losses necessitate operation of tubular cells at higher temperatures in order to achieve adequate performance, which limits the choice of materials for other cell components such as interconnects. Planar cells have high power densities and non-electrolyte supported designs can be run at temperatures as low at 500°C. Thermal cycling and long term degradation still present significant challenges that need to be addressed, but are significantly easier in lower temperature SOFC systems. The large areas of high temperature seals that are required for the planar design are also a major challenge that still needs to be solved. Hybrid designs such as flat-tubular or micro-tubular designs may help to overcome some of the limitations of tubular designs while maintaining their many advantages.

3.4.SOFC Components

The major components of an SOFC are the same as all fuel cells and consist of an anode, a cathode, and an electrolyte. Multiple cells are grouped into stacks in order to build up voltage. Individual cells are electrically connected together with an interconnect which also acts a barrier to keep the anode gas from one cell and cathode gas from the next separate. Depending on the design of the cell and stack, high temperature seals may also be required.

3.4.1. Electrolytes

SOFC electrolytes consist of an ionically conductive ceramic oxide, which conducts the O^{2-} ions produced at the cathode to the anode. The electrolyte also serves as a barrier to keep the fuel and oxidizing gases separate.

The most important requirement for a SOFC electrolyte is high ionic conductivity in order to minimize ohmic losses and low electronic conductivity in order to minimize losses due to electrolyte short circuits. There must also be no connected porosity within the electrolyte in order to prevent gas leakage between the anode and cathode cavities. In order to minimize resistive losses, the electrolyte should also be kept as thin as possible.

Frequently SOFC are designed to be anode or cathode supported. This enables the thickness of the electrolyte to be minimized (<10μm) because it does not need to provide mechanical support. If an electrolyte supported SOFC design is used, the electrolyte layer must be thicker (several 100μm) in order to provide mechanical support for the cell.

3.4.1.1. Yttria stabilized zirconia (YSZ)

The most common electrolyte used in SOFC is zirconia (ZrO_2), which is usually stabilized with 3, 8 or 10 mol% yttria (Y_2O_3) to form yttria-stabilized zirconia (YSZ). Yttria is added in order to stabilize the cubic phase and to enhance the ionic conductivity by increasing the number of oxygen vacancies. YSZ with 3 mol% yttria additions is only partially stabilized and consists of a mixture of a stabilized cubic phase and a metastable monoclinic (or tetragonal) phase depending on temperature. The dual phase microstructure has excellent mechanical properties, but lower ionic conductivity than fully stabilized YSZ. At yttria compositions of 8 mol% or greater the cubic phase in zirconia is fully stabilized. Fully stabilized YSZ compositions give maximum ionic conductivity. However, there has been some concern over the long term stability of YSZ stabilized with 8 mol% yttria. Several studies have shown that the ionic conductivity of 8 mol% YSZ decays over time at operating conditions. [13,14] Thus some SOFC developers have begun to use YSZ stabilized with 10 mol% yttria in order to ensure that the conductivity does not degrade over time.

Fully stabilized YSZ has excellent ionic conductivity at high temperatures (1000°C), but as the temperature decreases the ionic conductivity decreases. One of the major aims of most SOFC developers is to reduce the operating temperature in order to reduce sealing problems, to allow ferritic stainless steels to be used as interconnect materials and to increase cell lifetimes. As operating temperatures decrease there are two strategies in order to keep electrolyte performance at reasonable levels: decrease the YSZ electrolyte thickness or find new electrolyte materials with higher ionic conductivities. Much electrolyte research has focused on finding materials that exhibit higher ionic conductivities than YSZ at lower temperatures. However, YSZ is still a viable option for intermediate operating temperatures as ceramic processing techniques have improved to the point where reducing the electrolyte layer thickness to less than 10μm is quite feasible which allows operating temperatures to easily be reduced to 750°C or less. [15, 16]

3.4.1.2.Other electrolyte materials

Other dopants for zirconia have also been considered in order to increase the ionic conductivity. Scandia doped zirconia (ScSZ) has much higher ionic conductivity even at lower temperatures, but this conductivity degrades rapidly at SOFC operating temperatures due to the metastable nature of the phases. [17] ScSZ with a higher amount of Sc (10 – 15 mol%) is more stable at SOFC operating temperatures, but exhibits a phase change at 700 K. This is undesirable as the phase change causes irreversible thermal expansion and a decrease in ionic conductivity. Hirano and Oda have added 1 mol% Bi_2O_3 to 10 mol% ScSZ and have successfully suppressed this phase change. [18] They then fabricated cells that incorporated 10 mol% ScSZ as the electrolyte and electrochemically tested them at 800 and 1000°C. The cells exhibited sufficient stability and ionic conductivity when tested at both temperatures; however, long term testing to ensure the stability of 10ScSZ still needs to be performed.

Doped ceria electrolytes (especially samaria doped ceria (SCO) and gadolinia doped ceria (GCO)) have ionic conductivities higher than all zirconia based electrolytes (with the exception of ScSZ). Unfortunately doped ceria is reduced at the low oxygen partial pressures seen at the anode at elevated temperatures. [19] This reduction leads to an increase in electronic conductivity, which lowers the electrolyte's performance. In order to maximize performance, ceria electrolytes will either have to be coated by a thin layer of YSZ in order remain stable in the reducing conditions present on the anode side or the operating temperature of the fuel cell will have to be reduced low enough (<600°C) so that the change in oxidation state is negligible. [12] Since ceria and zirconia in contact with each other form solid solutions with low ionic conductivity at temperatures above 1200°C ceria/zirconia composite electrolytes will have to be processed below 1200°C. [17,20]

Recently, perovskites based on $LaGaO_3$ have been recognized as a potential low temperature SOFC electrolyte material. These perovskites may be doped by various elements in order to enhance their properties. Strontium and magnesium doped lanthanum gallate (LSGM) is most frequently studied due to its high ionic conductivity especially at low operating temperatures. LSGM reacts severely with fuel cell components at temperatures above 1300°C so fuel cell fabrication temperatures must be lowered to less than 1300°C. [21] LSGM may also be unstable in the reducing atmosphere present on the anode side of the fuel cell and thus may either have to be coated with a thin layer of YSZ to enhance its stability or the fuel cell's operating temperature may need to be reduced. [17]

A comparison of the conductivity of many commonly studied high temperature oxygen ion conductors is shown in Figure 3-10.

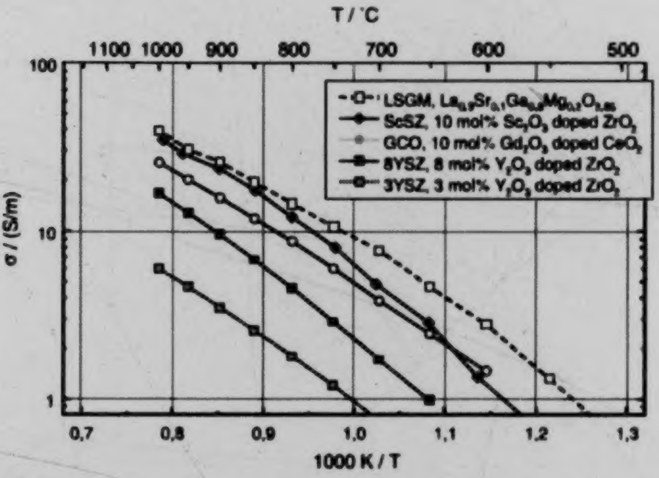

Figure 3-10: Ionic conductivity of various high temperature ionic conductors. [10]

3.4.1.3. Electrolyte materials issues

The most significant electrolyte materials issue is the interaction of the electrolyte with other fuel cell components. When YSZ is used as the electrolyte there are few interactions between the electrolyte and other components of the fuel cell, but thick YSZ films (several 100μm) can only be used at high temperatures (~1000°C). If very thin YSZ (<10 μm) electrolytes are used, the ohmic resistance is low enough that intermediate operating temperatures of 650 to 850°C are achievable. Ceria and LSGM based electrolytes have higher ionic conductivities making them easier to use at low temperatures, but may interact with other components during fabrication if the temperature exceeds 1200°C. [17]

As well these electrolytes are also not completely stable under the reducing conditions seen at the anode at temperatures greater than 600°C. In order to enhance the stability of ceria and LSGM electrolytes under anodic conditions, they may either be coated with a thin protective layer of YSZ or the operating temperature must be lower than 600°C.

3.4.2. Interconnects

The interconnect is used to electrically connect the cathode of one cell to the anode of a subsequent cell. This connection allows multiple cells to be connected in series to build up voltage, or in parallel in order to prevent cells from being electrically isolated if one cell fails. The interconnect also acts as a barrier to prevent the mixing of fuel and oxidizing gases.

Recently Ceres Power has begun to produce cells that are supported on ferritic stainless steel interconnects. The use of the interconnect as a support improves the mechanical strength and the thermal shock resistance of the cell. It also reduces the severity of temperature gradients within the cell due to the enhanced thermal conductivity of the metal and allows conventional metal forming and joining techniques such as welding to be used. [12]

Interconnect materials experience difficult conditions because they must be stable at fuel cell operating temperatures in both the oxidizing environment of the cathode and the reducing environment of the anode. The interconnect must be highly electrically conductive and have negligible ionic conductivity in order to minimize resistive losses, and have no porosity in order to keep the oxidant and fuel gases from mixing. As with all fuel cell components, the interconnect material must have a thermal expansion coefficient that matches the rest of the fuel cell components; it must be easy to fabricate and relatively inexpensive.

Electronically conductive oxides or high temperature oxidation resistant metal alloys are most commonly used as SOFC interconnects depending on the operating temperatures of the fuel cell. [17,22,23]

3.4.2.1.Ceramic interconnects

At high operating temperatures (1000°C) electronically conductive oxides must be used as interconnects. The most commonly used ceramic interconnect material used is doped $LaCrO_3$ (LC). This ceramic has adequate electronic conductivity at high temperatures, reasonable stability in oxidizing and reducing conditions, a compatible thermal expansion coefficient with other cell components, and low Cr vapour pressure, which inhibits Cr vapourization.

There are several material issues that arise from the use of ceramic interconnects. First of all, they have extremely low thermal conductivity, which imposes severe thermal gradients and therefore thermal stress on fuel cell stacks. As well, many of these oxides have slightly different thermal expansion properties depending on whether the environment is oxidizing or reducing. This difference in expansion causes the anode and cathode sides to expand at slightly different rates, which induces stress and may lead to catastrophic failure of the interconnect. Ceramic interconnects may also exhibit significant oxygen ion conductivity, which reduces performance. In addition, as the operation temperature of the cell decreases, the electronic conductivity will typically decrease making these material unfeasible for use at low temperatures. Finally, ceramic oxides are relatively brittle and may be expensive to produce and to form into the desired interconnect shapes.

3.4.2.2.Metallic interconnects

At operating temperatures lower than 850°C it becomes feasible to use high temperature oxidation resistant metal alloys for interconnects. Metal interconnects are preferable to ceramic ones because they have good mechanical stability, high thermal and electronic conductivity and little porosity. They are also easier to fabricate and machine and are less costly than ceramic interconnects. Ferritic stainless steels are the most commonly used metallic interconnect material due to their good oxidation resistance, excellent thermal expansion match with other components and relatively inexpensive cost. However, the high chromium content in these alloys may cause chromium vapourization which poisons the cathode and the electrical conductivity may decrease over time due to surface oxide scale growth during operation. Other specialty metal alloys such as Siemens /Plansee's Cr-based alloy or Ni-based high temperature superalloys are also being investigated. [22]

High temperature oxidation resistant alloys usually form protective chromium and/or aluminum oxide scales. Alumina scales provide better protection of the underlying alloy surface, but have very low electronic conductivities which increases the amount of resistive losses that are due to the interconnect. Chromia scales have better conductivity, but Cr vapourization may occur which deposits chromia at the electrolyte/cathode interface and degrades fuel cell performance by blocking active sites at the triple phase boundary. [22] In order to reduce the oxide scale thickness and prevent Cr vapourization a dense coating layer or a thin surface layer of reactive elements may be deposited in order to reduce the oxidation rate and protect the interconnect.

3.4.3. Seals

Although sealing difficulties may be alleviated by using alternative cell designs, i.e., tubular cells, the planar SOFC design used by many SOFC developers requires large areas to be sealed. Obviously, the first and most important requirement for SOFC seals is that they must form gas-tight seals to cell and stack components and must hold this seal during and after thermal cycling and long periods of use. In order for seals to successfully survive thermal cycling, they must have similar thermal expansion behaviour to cell components and be able tolerate large mismatches that may occur with stack components such as manifolds. Good sealing is critical in order to achieve high fuel utilizations, to prevent localized heating that occurs when leaked fuel burns, and to prevent air from leaking into the anode chamber to oxidize the anode if the fuel supply is interrupted. Since seals are exposed to all parts of the cell, they must be electronically insulating and chemically stable in oxidizing and reducing atmospheres. Finally, the seals must be stable over the lifetime of the system, i.e., inert to reactions with cell components and have low vapour pressure in order to minimize component losses through vapourization.

The high operating temperature of SOFC means that the majority of traditional seal types cannot be used. This requires the development of new high temperature seals. Glass and glass-ceramic seals, cement seals, compression seals, gold gaskets, and solid mica seals have been used to seal single cells and fuel cell stacks.

3.4.3.1.Glass and Glass-Ceramic Seals

The most commonly used type of seals in SOFC are glass or glass-ceramic seals. These seals are a viscous fluid at SOFC operating temperatures and thus are able to deal with thermal cycling easily. In order for these cells to work properly, they must have a glass transition temperature less than the SOFC operating temperature, in order to minimize stress build up, and must be viscous enough at operating temperatures so that flow does not occur. The minimum seal viscosity in order to prevent material flow is thought to be about 10^3 Pa-s. Below this viscosity, the seal will flow preventing the seal from forming an effective gas flow barrier. [24]

Many groups are working on glass and glass-ceramic seals for SOFC, but few results have been published due to the proprietary nature of most glass and glass-ceramic seals. Seal systems reported in the literature have been based on soda-lime glasses, other alkali silicates, alkaline-earth silicates, alkali borosilicates, [25] phosphate glasses, [26] aluminosilicate glasses, [27] and $SrO\text{-}La_2O_3\text{-}Al_2O_3\text{-}B_2O_3\text{-}SiO_2$ glasses. [24]

3.4.3.2.Other Types of Seals

Compression seals have been used to seal SOFC single cells. [23] These seals may not be very practical, as they are likely to leak if surfaces are not extremely flat. Gold gaskets have been used for lab scale SOFC testing. [23] These gaskets seal well, but are too expensive to be used in a large scale setting. Solid mica gaskets have also been used to seal cells. The test setup has been designed so that the seals were always under compressive spring loading by springs located outside the furnace. [28] These seals worked quite well, but this setup is likely not feasible for SOFC stacks.

3.4.3.3.Seal materials issues

Seals tend to contain large quantities of alkali or alkaline earth oxides in addition to SiO_2. These components are quite mobile at fuel cell operating conditions and tend to migrate and react with other cell components. [22] The reaction of seal components with cell materials may cause various detrimental phases to form, which degrade cell performance.

Seals that have poorly matched thermal expansion properties may degrade quickly after thermal cycling. Taniguichi et al. [25] have addressed this thermal degradation problem by adding ceramic fibers to the sealing material in order to suppress crack formation by relaxing stresses induced as a result of thermal cycling. Cells may also degrade over longer periods of time due to changes in the seal viscosity and composition. These changes are usually caused by reactions with cell components or by the volatility of some seal materials under operating conditions. [17]

3.4.4. Cathodes

SOFC cathodes provide reaction sites for the electrochemical reduction of the oxidant. The oxidant most commonly used in SOFC is air, although performance may be increased slightly by increasing the partial pressure of oxygen in the oxidizing gas. [29] The overall oxidation reaction takes place by the following reaction:

$$\frac{1}{2}O_2 + 2e^- \rightarrow O^{2-} \qquad \text{Reaction 3-1}$$

Most planar SOFC are not cathode supported; however, Siemens-Westinghouse's tubular SOFC design does rely on a cathode supported structure. Cathode materials must be stable in the oxidizing environment of the cathode and must have sufficient catalytic activity to reduce oxygen rapidly in order to ensure good performance. When fabricated, cathodes must have sufficient electronic conductivity to minimize resistive losses and adequate porosity to allow oxidant gas transport to reaction sites. Finally, the fabricated cathode must have a long triple phase boundary in order to enhance reaction rates.

The oxidizing conditions for the cathode and the high operating temperatures of SOFC narrow the choice of cathode materials to noble metals, electrically conducting oxides and mixed conducting oxides.

3.4.4.1. Doped Lanthanum Manganite (LSM)

The most commonly used SOFC cathode material is strontium doped lanthanum manganite (LSM). [30] LSM is stable in oxidizing atmospheres, has sufficient electronic conductivity at high temperatures and has a similar thermal expansion coefficient to YSZ. The conductivity in LSM is almost entirely electronic in nature; therefore, an ionically conducting phase such as YSZ is typically added to the LSM cathode in order to increase the triple phase boundary area and thus increase the number of reaction sites for oxygen reduction. [28] At high temperatures, LSM reacts with YSZ to form a poorly conducting $La_2Zr_2O_7$ phase. [31,32,33] This phase can be avoided, though, by fabricating the cell below 1200°C. [23] At low operating temperatures, LSM has poor electronic conductivity and other cathode materials are typically chosen.

3.4.4.2.Other Cathode Materials

The viability of alternative SOFC cathodes depends greatly on the electrolyte being used. Argonne National Laboratory has tested many new mixed conducting cathode materials on YSZ and GCO electrolytes. [23] On YSZ electrolytes, the majority of tested cathodes reacted with the electrolyte to form undesirable reaction products. The exception to this trend was $La_{0.8}Sr_{0.2}FeO_3$ (LSF), which exhibited high, stable performance and no undesirable reactions with YSZ. When GCO electrolytes were used, several promising potential candidates were found. $La_{0.8}Sr_{0.2}CoO_3$ (LSC) and $La_{0.8}Sr_{0.2}Co_{0.8}Fe_{0.2}O_3$ (LSCF) are too reactive to be used with YSZ electrolytes, but exhibit strong, stable electrochemical performance on GCO electrolytes. [23] $Sm_{0.8}Sr_{0.2}CoO_3$ and $Gd_{0.8}Sr_{0.2}CoO_3$ also performed very well. Lowering cell fabrication and operation temperatures may eliminate the undesirable reactions between cathode and electrolyte materials.

3.4.5. Anodes

In SOFC the anode provides reaction sites for the electrochemical oxidation of the fuel. The overall reaction that takes place depends on the fuel being used but typically oxidation takes place by the following reactions:

$$H_2 + O^{2-} \rightarrow H_2O + 2e^- \qquad \text{Reaction 3-2}$$

or if CO is used as the fuel

$$CO + O^{2-} \rightarrow CO_2 + 2e^- \qquad \text{Reaction 3-3}$$

Other reactions such as the direct oxidation of hydrocarbons may take place if unreformed or partially reformed hydrocarbon fuels are used.

Frequently a two layer anode structure is used. A thicker, coarse microstructure substrate layer, often up to 1 mm thick, is used as the mechanical support for the cell, while a thinner, finer microstructure functional layer (10 to 15 µm) serves as the active area where electrochemical oxidation of the fuel occurs. The anode substrate layer must be sufficiently porous in order to allow fuel gases to transport to reaction sites, while still having enough strength to support the cell and good electronic conductivity to minimize ohmic resistance losses. The anode functional layer must have good catalytic activity for the oxidation of H_2 and CO and a long triple phase boundary in order to enhance reaction rates.

Anode materials must be stable in the reducing environment of the anode and should be reasonably tolerant to fuel impurities such as sulphur. As hydrocarbon fuels will typically be used as fuels, SOFC anodes must also have good catalytic activity for either steam reforming or for the direct oxidation of hydrocarbons, but must not promote carbon deposition at operating conditions. Finally, the anodes should be reasonably tolerant to slightly oxidizing environments, in case air is introduced to the anode cavity due to seal leakage, fuel supply interruption or system shutdown.

Anode substrates typically have reasonably coarse microstructures in order to have good porosity and electrical conductivity, while anode functional layers have very fine microstructures to maximize the length of the triple phase boundary. The microstructure of the SOFC anodes plays a critical role in determining anode performance and stability in fuel cell operating environments. [17] Typical anode substrate and anode functional layer microstructures can be seen in Figure 3-11.

Electrolyte
Anode functional layer
Anode substrate

Figure 3-11: SEM image illustrating the difference between the fine microstructure anode functional layer and coarse microstructure anode substrate. [9]

3.4.5.1. Ni/YSZ cermets

The reducing conditions of the anode chamber narrows the choice of anode materials to metals, electrically conducting oxides and mixed conducting oxides. The typically high operating temperatures of SOFC limit suitable metallic materials to nickel, cobalt and noble metals.

Typically, SOFC anodes are fabricated from a NiO/yttria-stabilized zirconia (YSZ) ceramic composite and are reduced in-situ, during operation, to form a Ni/YSZ cermet with greater than 30% porosity. Nickel is used as the electrically conductive component of the anode because it has excellent catalytic activity for CO and H_2 oxidation, electrical conductivity, and mechanical properties, and is relatively inexpensive. The YSZ component is used to minimize coarsening of the Ni particles at operating temperatures and to reduce the thermal expansion of the anode in order to better match the thermal expansion of the other components. Most commonly, a cermet with a nickel content of 40 vol% is used in order to provide good electronic conductivity.

3.4.5.2. Other Anode Materials

Other potential anode materials have been studied including: Co/YSZ, Ru/YSZ, Cu/ceria/YSZ, [34,35,36,37,38] niobia based rutiles,[39] doped ceria/Ni, [40,41] gadolinia-doped ceria (Ce0.6Gd0.4O1.8), [42] tungsten bronzes, [43] $SrTiO_3$, [44] $La_{0.8}Sr_{0.2}Cr_{0.97}V_{0.03}O_3$ (LSCV)/YSZ, [45] and various doped $LaCrO_3$, [45,46,47] but Ni/YSZ is still the anode material of choice for the vast majority of SOFC systems. The copper/ceria/YSZ system is quite a promising materials choice in order to address reduction/oxidation (redox), sulphur and carbon deposition issues, but it is difficult to fabricate and may not have sufficient long term stability due to sintering and creep of the copper component.

Many of these new anode materials are more tolerant to sintering, fuel impurities, carbon deposition and redox cycling; however, performance, stability and cost issues mean that the Ni/YSZ system is still the anode material of choice for most SOFC developers.

3.4.5.3.Anode materials issues

There are four main anode materials issues in SOFC: anode sintering, fuel impurities, carbon deposition and redox cycling.

3.4.5.3.1. Anode sintering

Since the operating temperature of most SOFC systems is greater than half of the melting point of nickel (1728 K) sintering of the nickel particles in the anode is likely to occur. The electrochemical performance of the anode degrades as Ni particles coarsen, because the length of the triple phase boundary and, therefore, the number of reaction sites decreases. Ceramic phases (usually YSZ) are added to the anode in order to help suppress Ni sintering, but they are not completely effective in stopping degradation.

Attempts to reduce Ni sintering have mainly focused on the optimization of the anode microstructure by altering the YSZ or Ni particles, the addition of other components to the anode in order to enhance metal-ceramic interfacial bonding, or the replacement of Ni with other higher melting point materials. [48,49,50,51,52,53,54]

3.4.5.3.2. Sulphur poisoning

Sulphur is present as an impurity in most hydrocarbon based fuels. Commercial SOFC systems will likely utilize hydrocarbon fuels and therefore will likely be exposed to some amount of sulphur impurities. While SOFC have higher sulphur tolerances than other types of fuel cells, current cells cannot tolerate sulphur levels of more than several ppm without permanent degradation.

[55] The effect of sulphur on SOFC is being studied by several groups and new more sulphur tolerant materials are being developed.

Novel sulphur tolerant anode materials are being developed by Kim et al. [38] The anode material being developed consists of a Cu/ceria/YSZ cermet. Copper-based cermets are significantly more tolerant to sulphur than the traditional Ni-based ones, since copper sulphides are less stable than nickel sulphides and therefore are less likely to form. [34] As well, sulphides adsorbed on the copper surface will likely not affect performance, as copper does not appear to act as a catalyst for anode reactions. Ceria is therefore an essential component in these anodes in order to catalyze the hydrocarbon oxidation. [37]

Sulphur poisoning is a significant problem when traditional Ni/YSZ anodes are fuelled by hydrocarbons with sulphur impurities, especially at lower temperatures. It is unclear whether the poisoning is fully reversible. One group has found that the poisoning is fully reversible up to 100ppm H_2S concentrations and that the lost performance can be recovered by supplying unpoisoned gas or steam [55]. Another group has found that the poisoning degradation may not be fully recoverable even after poisoning at levels as low as 1ppm. [56]

3.4.5.3.3. Carbon Deposition

Commercial SOFC systems are likely to be fuelled, at least in the short term, by hydrocarbon fuels. SOFC are ideally suited to utilize these fuels due to their high operating temperatures and both internal reforming and direct oxidation of hydrocarbons are possible. However, Ni-based anodes promote the catalytic cracking of hydrocarbons which may result in carbon deposition. The deposited carbon blocks active sites on the anode and thus degrades the performance. The deposition of carbon on the anode surface may also promote the corrosion of the Ni by a process called metal dusting. [57]

Carbon deposition rates are affected by the fuel type, the steam/carbon (S/C) ratio, the temperature, the humidity, the operating current, and the electrode materials. There are three main strategies that can be used to minimize carbon formation on the anode.

The first technique involves changing the properties of the fuel by changing the fuel type or the S/C ratio. Simple hydrocarbon fuels such as methane are much less prone to carbon formation than larger hydrocarbons such as toluene. [58] If the S/C ratio is high (i.e., wet fuel) then carbon deposition is suppressed. [34] This is an effective solution to deal with carbon formation, but is not typically used because steam addition adds complexity to fuel delivery systems and because steam additions dilute the fuel and thus lower the efficiency. [59]

Carbon deposition may also be inhibited by changing the operating conditions of the fuel cell in order to operate under conditions in which carbon formation is not favoured. Murray et al. have investigated carbon deposition on a Ni/YDC/YSZ anode and a Ni/YSZ anode at various temperatures. [60] Carbon deposition from methane generally occurs either by methane pyrolysis,

$$CH_4 \rightarrow C + 2H_2 \qquad \text{Reaction 3-4}$$

or by carbon monoxide disproportionation,

$$2CO \rightarrow C + CO_2 \qquad \text{Reaction 3-5}$$

At high temperatures (>700°C) the methane pyrolysis reaction tends to dominate. At low temperatures, Reaction 3-5 tends to dominate except in cases where the CO to CO_2 ratio is very low. Therefore if the temperature is kept below 700°C to minimize the methane pyrolysis reaction, and the CO/CO_2 ratio is kept low, carbon deposition will not be favoured. When Murray et al. tested cells at these conditions, they found that carbon deposition on both types of cells was eliminated at operating temperatures less than 700°C for both humidified and dry methane fuels. [60]

The final method looks to inhibit carbon formation by choosing anode materials that do not promote carbon deposition. Copper is one of the most popular replacements for Ni. [35] Copper was chosen as a replacement, because it has excellent electrical conductivity and because it does not catalyze the deposition of carbon. [61] Unfortunately, Cu also does not catalyze the oxidation of the fuel and so an oxidation catalyst such as ceria must also be added. It has been seen in various studies that no carbon deposition occurs on Cu/ceria/YSZ anodes even when larger hydrocarbons such as n-decane are used as the fuel;

however, Cu anodes present other difficulties. Cu has a much lower melting point (1083°C) than Ni. This forces the use of complex lower temperature fabrication processes and probably limits these anodes to lower temperature operation in order to limit anode sintering.

In order to address the difficulties with Cu/ceria/YSZ anodes, Ni has been added to enhance catalytic activity and to raise the melting point of the metal. Kim et al. have studied the properties of these cermets with varying amounts of Cu and Ni in order to determine if they have sufficient resistance to carbon deposition. [36] As the Cu/Ni ratio was decreased, the amount of carbon increased, but deposition did not reach as significant a level as in anodes made completely of Ni. Deposition amounts actually seemed to reach a constant value after extended time periods.

The addition of various dopants to Ni may also decrease rates of carbon formation. [62] Alkali additives such as potassium could be used to reduce carbon deposition by increasing the reaction rate of carbon with steam and by neutralizing the acidity of the cathode support. Various transition metals have also been considered as additives to reduce carbon deposition. [62,63]

A $La_{0.8}Sr_{0.2}Cr_{0.97}V_{0.03}O_3$ (LSCV)/YSZ ceramic was investigated as a possible SOFC anode material for cells with hydrocarbon fuel. [45] LSCV was chosen because it is inert to methane cracking and because it is very compatible with other fuel cell materials, as it is commonly used as an interconnect material. Ru was added to the anode to act as a steam reforming catalyst.

3.4.5.4.Cyclic Reduction/Oxidation (Redox)

Since the most common SOFC anode is a cermet (Ni/YSZ), reoxidation of the metallic component of the anode may occur due to seal leakage, fuel supply interruption or system shutdown. In order to reuse a reoxidized cell, it must be reduced again. Thus, cyclic reduction and oxidation (redox) of the anode is likely to occur during SOFC operations.

The reduction and oxidation of nickel will result in large bulk volume changes. The bulk volume of a fully dense NiO sample should contract by 40.9% upon reduction and should expand by 69.2% upon oxidation. (See Appendix 3-1 for calculations.) A porous NiO/YSZ SOFC anode will likely not experience such a drastic volume change due to expansion into the pores, but any volume change that does occur may have a significant effect on the integrity of interfaces within a fuel cell and thus result in significant performance degradation.

System redox solutions, such as the use of a reducing purge gas, are possible, but are cumbersome and expensive. The choice of an anode material that is not susceptible to oxidation such as ceramic oxide materials is another possibility to enhance redox tolerance. However, currently there are no replacement anode materials that exhibit similar performance to the current Ni/YSZ materials system. Therefore, if the anode material remains as Ni/YSZ, then the only way to enhance redox tolerance is to modify the microstructure of the anode. Several groups have begun to evaluate how the mechanical properties of the Ni/YSZ system change after redox cycling. [64,65,66] However, no groups have systematically investigated either the microstructural changes that occur after redox cycling or the degradation in electrochemical performance that occurs after redox cycling. This study will investigate these issues.

3.5. Scope of Thesis

This study will initially characterize the baseline redox tolerance of the standard TSC-2 cells produced at Fuel Cell Energy, Ltd. The investigation is separated into four main areas:

1. A study of the reduction and oxidation kinetics of the Ni/YSZ system using thermogravimetric analysis (TGA).
2. An investigation into the volume changes that occur upon cyclic reduction and oxidation using thermomechanical analysis (TMA).
3. Single cell electrochemical testing of SOFC after redox cycling.
4. An analysis of the microstructural changes that occur after redox cycling using scanning and transmission electron microscopy.

After an initial baseline of redox tolerance is established, several strategies are developed order to enhance the redox tolerance of the cell. The ability of these strategies to improve redox tolerance are characterized using single cell electrochemical testing and electron microscopy and then compared to the baseline redox tolerance.

It is likely that redox cycling causes two distinct types of degradation: mechanical damage due to the expansion of Ni as it oxidizes and the more difficult to characterize microstructural damage. The first type of damage should be easy to characterize, as it likely will cause cracking in the electrolyte or delamination of fuel cell layers. The second type is much more difficult to investigate since there is no general agreement on what constitutes good anode microstructure, so it will be difficult to examine the subtle microstructural changes caused by redox that result in performance degradation. All electrochemical performance tests must be designed in order to separate these two different types of damage.

A theoretical redox depth strategy has been developed in order to better define exactly how much oxidation is occurring. This analysis uses the amount of Ni within the cell and the flow rate of air to predict the amount of time it takes to oxidize the cell to a specific redox depth. (See Appendix 3-2 for calculations.) This analysis assumes that all the oxygen passed through the anode during the redox cycle reacts to form NiO. The validity of this assumption is verified using gas chromatography (GC) analysis of the outlet gas to determine when oxygen is first detected in the outlet gas.

3.6.Summary

Fuels cells are energy generation technologies that cleanly and efficiently produce electricity through electrochemical reactions. SOFC have several advantages over other types of fuel cells including: excellent efficiency, high grade byproduct heat, all solid-state construction and fuel flexibility. There are still many technical challenges resulting from the high operating temperatures and hydrocarbon fuel usage of SOFC that need to be overcome before successful commercialization can occur.

There are two main SOFC cell designs that are currently being developed: tubular and planar. Tubular designs have better mechanical and thermal stability and seem to have less long term degradation issues, but have high fabrication costs and lower inherent performance due to their greater internal resistance losses. Tubular cells also have no issues with high temperature sealing due to the inherent configuration of the design. Planar designs are much easier and cheaper to fabricate and typically have much higher power densities, but these cells require large areas to be sealed with high temperature seals. These cells are also less mechanically and thermally stable, so thermal cycling may be a problem; however, the inherently low resistance losses of planar cells means that these cells can be operated at lower temperatures, which allows less expensive materials to be utilized and reduces long term degradation rates and thermal cycling losses. Hybrid designs, such as the flat tubular design, which incorporate the beneficial aspects of both tubular and planar designs, are being investigated by a few groups.

SOFC electrolytes are typically fully dense YSZ (yttria stabilized zirconia) ceramics. In electrolytes, the major materials issues to be faced are the interactions of the electrolyte with other components and enhancement of low temperature ionic conductivity. Electrolyte material issues are mainly being addressed by developing new electrolyte materials with higher ionic conductivity.

Ceramic or metallic materials can be used as interconnects. At high operating temperatures doped LC ($LaCrO_3$) is frequently used as the interconnect material, but difficulties may arise due to LC's low thermal conductivity and the differential expansion it may exhibit in reducing versus oxidizing atmospheres. At lower operating temperatures ferritic stainless steels are commonly used as interconnects, but oxide scale growth and Cr vapour deposition on the cathode may cause performance degradation. Interconnect materials issues are mainly being addressed by coating the interconnect surface or by the development of new materials.

Glass or glass-ceramic seals are commonly used for planar SOFC. The migration and interaction of seal components and the thermal and chemical degradation of the seals are the primary issues in this system and are being addressed mainly by modifying seal material compositions. High temperature seals are not required for tubular SOFC designs, so sealing requirements are easily met.

The most common cathode material is LSM (strontium doped lanthanum manganite); however, this material interacts with other cell components at temperatures typically used during fabrication and has insufficient performance at low temperatures. LSM can be doped or modified to improve performance, but it is more likely that new cathode materials currently in development will replace LSM, especially for cells operating at lower temperatures.

Anode materials are typically porous Ni/YSZ cermets. While Ni sintering at operating temperatures may be a problem, the most significant anode difficulties such as sulphur poisoning and carbon deposition result from the use of hydrocarbon fuels. Redox cycling is another major anode material challenge that still needs to be overcome. Many of these difficulties can be addressed by optimizing the anode microstructure, the operating conditions or by developing new anode materials such as copper/ceria anodes.

This thesis will examine the challenge of anode redox tolerance and attempt to find ways to improve the redox tolerance of the Ni/YSZ system. The study will first characterize the oxidation and reduction behaviour of Ni/YSZ cermets using

TGA and TMA and will then use single cell electrochemical testing and electron microscopy to develop a baseline of the redox tolerance of SOFC produced by Fuel Cell Energy Ltd. Fuel Cell Energy's standard TSC-2 production process. After this initial baseline testing is completed, several strategies to improve the redox tolerance will be investigated.

3.7. Appendices

3.7.1. Appendix 3-1: Bulk volume changes for a fully dense Ni sample upon redox cycling

$$\text{Volume change} = \frac{\Delta V}{V_i} = \frac{V_f - V_i}{V_i} = \frac{\left(\frac{MW_f}{\rho_f}\right) - \left(\frac{MW_i}{\rho_i}\right)}{\left(\frac{MW_i}{\rho_i}\right)}$$

where: V_f is the final volume (cm^3)
V_i is the initial volume (cm^3)
MW_f is the molecular weight of the final species (g/mol)
MW_i is the molecular weight of the initial species (g/mol)
ρ_f is the density of the final species (g/cm^3)
ρ_I is the density of the initial species (g/cm^3)

Table 1: Physical data for Ni and NiO

[illegible]	[illegible]	[illegible]
Ni	58.7	8.9
NiO	74.7	6.7

For reduction: $NiO \rightarrow Ni + \frac{1}{2}O_2$

$$\frac{\Delta V}{V_i} = \frac{\left(\frac{58.7}{8.9}\right) - \left(\frac{74.7}{6.7}\right)}{\left(\frac{74.7}{6.7}\right)} = -0.408$$

Upon reduction a volume decrease of 40.8% occurs.

For oxidation: $Ni + \frac{1}{2}O_2 \rightarrow NiO$

$$\frac{\Delta V}{V_i} = \frac{\left(\frac{74.7}{6.7}\right) - \left(\frac{58.7}{8.9}\right)}{\left(\frac{58.7}{8.9}\right)} = 0.690$$

Upon oxidation a volume increase of 69.0% occurs.

3.7.2. Appendix 3-2: Redox depth calculations

How much O_2 is required to oxidize the cell to various redox depths?

This analysis will give us an approximate idea of how fast a cell will oxidize when exposed to a certain flow rate of air.

Assumptions: All O_2 is consumed by the oxidation process.
The amount of Ni in the anode functional layer is negligible compared to the amount of Ni present in the anode substrate.
Oxygen behaves as an ideal gas.

Average cell param [illegible]	
Length	100 mm
Width	100 mm
Thickness	1.1 mm
Weight	56 g
Density	5.09 g/cm^3
Volume	11000 mm^3
Wt% NiO in as prepared (oxidized) cell	57 %
Wt% YSZ in as prepared cell	43 %

[illegible]	[illegible]	[illegible]
Ni	58.70	8.91
NiO	74.69	6.70
ZrO2	123.22	5.68
Y2O3	225.81	5.03
O	16.00	-

How much Ni is in the cell?

If the average as prepared (oxidized) cell weight is 56 g and it contains 57 wt% NiO.

Then the amount of NiO is: $m_{NiO} = 0.57*56 = 31.92$ g

For oxidation: $$Ni + \frac{1}{2}O_2 \rightarrow NiO \qquad (1)$$

Therefore the number of moles of NiO or Ni in an average cell is:

$$\text{moles NiO} = \frac{0.57*56}{\text{MW NiO}} = \text{moles Ni} = 0.427349 \text{ moles}$$

How much O_2 is required to oxidize the amount of Ni in the cell?

From Reaction (1) the number of moles of O_2 requred to fully oxidize the amount of Ni in an average cell is: $mol_{O_2} = ½\, mol_{Ni} = 0.213675$ moles

Using the ideal gas law: $n = \frac{PV}{RT}$

where: P is the partial pressure of oxygen in air = 0.21 atm
V is the volumetric flow rate of oxygen = 0.0252 SLPM (0.12 SLPM air)
n is the molar flow rate of oxygen
R is the universal gas constant = 0.082057 atm L / mol
T is the temperature = 298 K

Plugging in the numbers: $n = \frac{0.21 * 0.0252}{0.082057 * 298} = 0.001031$ mol/min

For full oxidation 0.213675 mol of O_2 are required

Therefore full oxidation occurs after: $\frac{0.213675 \text{ mol}}{0.001031 \text{ mol/min}} = 207.34 \text{ min}$

And 20% redox depth is reached in: 207.34 min * 0.20 = 41.47 min

3.8.Bibliography

G.J.K. Acres, *Journal of Power Sources*, **100** (2001) 60.

C.C Appel, N. Bonanos, *Journal of the European Ceramic Society*, **19** (1999) 847.

S.P.S. Badwal, *Solid State Ionics*, **143** (2001) 39.

P. Bance, N.P. Brandon, B. Girvan, P. Holbeche, S. O'Dea, B.C.H. Steele, *Journal of Power Sources*, **131** (2004) 86.

M. Brown, S. Primdahl, M. Mogensen, *Journal of the Electrochemical Society*, **147** (2000) 475.

T. Brylewski, M. Nanko, T. Maruyama, K. Przybylski, *Solid State Ionics*, **143** (2001) 131.

L. Carrette, K.A. Friedrich and U. Stimming, *Fuel Cells*, **1** (2001) 5.

C.M. Chun, J.D. Mumford, T.A. Ramanarayanan, *Journal of the Electrochemical Society*, **147** (2000) 3680.

R. Doshi, V.L. Richards, J.D. Carter, X. Wang, M. Krumpelt, *Journal of the Electrochemical Society*, **146** (1999) 1273.

C.M. D'Souza, N.M. Sammes, *Journal of the American Ceramic Society*, **83** (2000) 47.

R.J. Gorte, H. Kim, J.M. Vohs, *Journal of Power Sources*, **106** (2002) 10.

R.J. Gorte, S. Park, J.M. Vohs, C. Wang, *Advanced Materials*, **12** (2000) 1465.

C.M. Finnerty, N.J. Coe, R.H. Cunningham, R.M. Ormerod, *Catalysis Today*, **46** (1998) 137.

D. Fouquet, A.C. Muller, A. Weber, E. Ivers-Tiffee, *Ionics* **8** (2003) 103.

Fuel Cell Handbook, 6th ed., EG&G Technical Services Inc., 2002.

T. Fukui, S. Ohara, K. Mukai, *Electrochemical and Solid State Letters*, **1** (1998) 120.

T. Fukui, S. Ohara, M. Naito, K. Nogi, *Journal of Power Sources*, **110** (2002) 91.

S. M. Haile, *Acta Materialia*, **51** (2003) 5981.

K. Hassmann, *Fuel Cells*, **1** (2001) 78.

M. Hattori, Y. Takeda, Y. Sakaki, A. Nakanishi, S. Ohara, K. Mukaic, J. Lee, T. Fukui, *Journal of Power Sources*, **126** (2004) 23.

T. Hibino, A. Hashimoto, M. Suzuki, M. Sano, *Journal of the Electrochemical Society*, **149** (2002) A1503.

K. Hipert, D. Das, M. Miller, D.H. Peck, R. Weiss, *Journal of the Electrochemical Society*, **143** (1996) 3642.

M. Hirano, T. Oda, *Journal of the American Ceramic Society*, **85** (2002) 1336.

T. Horita, N. Sakai, T. Kawada, H. Yokokawa, M. Dokiya, *Journal of the Electrochemical Society*, **143** (1996) 1161.

Yin Chang Hsiao, J. R. Selman, *Solid State Ionics*, **98** (1997) 33.

M. Ihara, C. Yokoyama, A. Abudula, R. Kato, H. Komiyama, K. Yamada, *Journal of the Electrochemical Society*, **146** (1999) 2481.

J.T.S. Irvine and A. Sauvet, *Fuel Cells*, **1** (2001) 205.

T. Ishihara, K. Shimose, T. Kudo, H. Nishiguchi, T. Akbay, Y. Takita, *Journal of the American Ceramic Society*, **83** (2000) 1921.

H. Itoh, T. Yamamoto, M. Mori, T. Horita, N. Sakai, H. Yokokawa, M. Dokiya, *Journal of the Electrochemical Society*, **144** (1997) 641.

W.S. Jang, S.H. Hyun, S.G. Kim, *Journal of Materials Science*, **37** (2002) 2535.

Y. Jiang, A.V. Virkar, *Journal of the Electrochemical Society*, **148** (2001) A706.

S.P. Jiang, J.P. Zhang, L. Apateanu, K. Foger, *Journal of the Electrochemical Society*, **147** (2000) 4013.

S.P. Jiang, J.P Zhang, K. Foger, *Journal of the Electrochemical Society*, **147** (2000) 3195.

S.P. Jiang, J.P. Zhang, K. Foger, *Journal of the Electrochemical Society*, **148** (2001) C447.

S.P. Jiang, J.P. Zhang, X.G. Zheng, *Journal of the European Ceramic Society*, **22** (2002) 361.

M.J. Jorgensen, S. Primdahl, C. Bagger, M. Mogensen, *Solid State Ionics*, **139** (2001) 1.

A. Kaiser, J.L Bradley, P.R. Slater, J.T.S. Irvine, *Solid State Ionics*, **135** (2000) 519.

V.V. Kharton, F.M. Figueredo, L. Navarro, E.N. Naumovich, A.V. Kovalevsky, A.A. Yaremchnko, A.P. Viskup, A. Carneiro, F.M.B. Marques, J.R. Frade, *Journal of Materials Science*, **36** (2001) 1105.

K Kieveland, M. Einarsrud, C.R. Schmidt, S. Shamsili, S. Faaland, K. Wiik, T. Grande, *Journal of the American Ceramic Society*, **82** (1999) 729.

H. Kim, C. Lu, W.L. Worrell, J.M. Vohs, R.J. Gorte, *Journal of the Electrochemical Society*, **149** (2002) A247.

H. Kim, S. Park, J.M. Vohs, R.J. Gorte, *Journal of the Electrochemical Society*, **148** (2001) A693.

H. Kim, J.M. Vohs, R.J. Gorte, *Chemistry Communications*, (2001) 2334.

J. Kim, R. Song, K. Song, S. Syun, D. Shin, H. Yokokawa, *Journal of Power Sources*, **122** (2003) 138.

J. Kim, A.V. Virkar, K. Fung, K. Mehta, S.C. Singhal, *Journal of the Electrochemical Society*, **146** (1999) 69.

S.G. Kim, S.P. Yoon, S.W. Nam, S.H. Hyun, S.A Hong, *Journal of Power Sources*, **110** (2002) 222.

L. Kindermann, D. Das, D. Bahadur, R. Weiss, H. Nickel and K. Hilpert, *Journal of the American Ceramic Society*, **80** (1997) 909.

N. Kiratzis, P. Holtappels, C.E. Hatchwell, M. Mogensen, J.T.S. Irvine, *Fuel Cells*, **1** (2001) 211.

J. Koh, B. Kang, H.C. Lim, and Y. Yoo, *Electrochemical and Solid-State Letters*, **4** (2001) A12.

J. Koh, Y. Yoo, J. Park, H.C. Lim, *Solid State Ionics*, **149** (2002) 157.

H. Koide, Y. Someya, T. Yoshida, T. Maruyama, *Solid State Ionics*, **132** (2000) 253.

N. Lahl, D. Bahadur, K. Singh, L. Singheiser, K. Hilpert, *Journal of the Electrochemical Society*, **149** (2002) A607.

J. Larminie and A. Dicks, *Fuel Cell Systems Explained*, John Wiley & Sons Ltd., West Sussex, England, 2000.

P.H. Larsen, P.F. James, *Journal of Materials Science*, **33** (1998) 2499.

J.H. Lee, H. Moon, H.W. Lee, J. Kim, J.D. Kim, K.H. Yoon, *Solid State Ionics*, **148** (2002) 15.

J. Lee, T. Mori, J. Li, T. Ikegami, *Journal of Materials Research*, **16** (2001) 2377.

J. Lee, T. Mori, J. Li, T. Ikegami, M. Komatsu, H. Haneda, *Journal of the American Ceramic Society*, **83** (2000) 1273.

J. Lee, T. Mori, J. Li, T. Ikegami, M. Komatsu, H. Haneda, *Journal of the Electrochemical Society*, **147** (2000) 2822.

K.L. Ley, M. Krumpelt, R. Kumar, J.H. Meiser, I. Bloom, *Journal of Materials Research*, **11** (1996) 1489.

Y. Li, J. Chen, L. Chang, Y. Qin, *Journal of Catalysis*, **178** (1998) 76.

R. Maric, S. Ohara, T. Fukui, T. Inagaki, J. Fujita, *Electrochemical and Solid-State Letters*, **1** (1998) 201.

O.A. Marina, C. Bagger, S. Primdahl, M. Mogensen, *Solid State Ionics*, **123** (1999) 199.

Y. Matsuzaki, I. Yasuda, *Solid State Ionics*, **132** (2000) 261.

Y. Matsuzaki, I. Yasuda, *Solid State Ionics*, **132** (2000) 271.

Y. Matsuzaki, I. Yasuda, *Journal of the Electrochemical Society*, **148** (2001) A126.

N. Minh and T. Takahashi, *Science and Technology of Ceramic Fuel Cells*, Elsevier Science, Amsterdam, The Netherlands, 1995.

Y. Mishima, H. Mitsuyasu, M. Ohtaki, K. Eguchi, *Journal of the Electrochemical Society*, **145** (1998) 1004.

C.S. Montross, H. Yokokawa, and M. Dokiya, *British Ceramic Transactions*, **101** (2002) 85.

M. Mori, Y. Hiei, T. Yamamoto, H. Itoh, *Journal of the Electrochemical Society*, **146** (1999) 4041.

E.P. Murray, T. Tsai, S.A. Barnett, *Nature*, **400** (1999) 649.

H. Negishi, N. Sakai, K. Yamaji, T. Horita, H. Yokokawa, *Journal of the Electrochemical Society* **147** (2000) 1682.

H. Negishi, K. Yamaji, N. Sakai, T. Horita, H. Yanagishita, H. Yokokawa, *Journal of Materials Science*, **39** (2004) 833.

K. Nomura , Y. Mizutani , M. Kawai , Y. Nakamura , O. Yamamoto, *Solid State Ionics*, **132** (2000) 235.

S. Park, R. Craciun, J.M. Vohs and R.J. Gorte, *Journal of the Electrochemical Society*, **146** (1999) 3603.

S. Park, R.J. Gorte, J.M. Vohs, *Journal of the Electrochemical Society*, **148** (2001) A443.

S. Park, J.M. Vohs, R.J. Gorte, *Nature*, **404** (2000) 265.

M. Prica, T. Alston, K. Kendall, in Proc. Solid Oxide Fuel Cells V (U. Stimming, S. C. Singhal, H. Tagawa and W. Lehnert Eds.) The Electrochemical Society Proceedings Series (1997) 619.

S. Primdahl, *PhD Thesis, University of Twente*, (1999).

S. Primdahl and M. Mogensen, *Journal of Applied Electrochemistry*, **30** (2000) 247.

J.M. Ralph, A.C. Schoeler, M. Krumpelt, *Journal of Materials Science*, **36** (2001) 1161.

C.M. Reich, A. Kaiser and J.T.S. Irvine, *Fuel Cells*, **1** (2001) 249.

P. Sarkar, D. De, H. Rho, *Journal of Materials Science*, **39** (2004) 819.

D. Skarmoutsos, F. Tietz and P. Nikolopoulos, *Fuel Cells*, **1** (2001) 243.

D. Simwonis, F. Tietz, D. Stover, *Solid State Ionics*, **132** (2000) 241.

G. Stathis, D. Simwonis, F. Tietz, A. Moropoulou, A. Naoumides, *Journal of Materials Research* **17** (2002) 951.

B.C.H. Steele, *Journal of Materials Science*, **36** (2001) 1053.

B.C.H. Steele, *Nature*, **400** (1999) 619.

Suzuki, Sasaki, Otoshi, Kajimura, Ippommatsu, *Solid State Ionics*, **62** (1993) 125.

S. Taniguchi, M. Kadowaki, H. Kawamura, T. Yasuo, Y. Akiyama, Y. Miyake, T. Saitoh, *Journal of Power Sources*, **55** (1995) 73.

S. Taniguchi, M. Kadowaki, T. Yasuo, Y. Akiyama, Y. Miyake, K. Nishio, *Journal of Power Sources*, **90** (2000) 163.

N. Tikekar, T. Armstrong, A. Virkar, in Proc. Solid Oxide Fuel Cells VIII (S. C. Singhal and M. Dokiya Eds.) *The Electrochemical Society Proceedings Series* (2003) 670.

G. A. Tompsett, C. Finnerty, K. Kendall, T. Alston, N. M. Sammes, *Journal of Power Sources*, **86** (2000) 376.

H. Uchida, S. Arisaka, M. Watanabe, *Solid State Ionics*, **135** (2000) 347.

K. Vels Jensen, S.Primdahl, I. Chorkendorff, M. Mogensen, *Solid State Ionics*, **144** (2001) 197.

P. Vernoux, M. Guillodo, J. Fourletier, A. Hammou, *Solid State Ionics*, **135** (2000) 425.

I. Villarreal, C. Jacobson, A. Leming, Y. Matus, S. Visco and L. De Jonghe, *Electrochemical and Solid-State Letters*, **6** (2003) A178.

D. Waldbillig, A. Wood, D.G. Ivey, *Solid State Ionics*, (2004) In press.

C. Wang, W.L. Worrel, S. Park, J.M. Vohs, R.J. Gorte, *Journal of the Electrochemical Society*, **148** (2001) A864.

A. Weber and E. Ivers-Tiffee, *Journal of Power Sources*, **127** (2004) 273.

T.L. Wen, D. Wang, M. Chen, H. Tu, Z. Lu, Z. Zhang, H. Nie, W. Huang, *Solid State Ionics*, **148** (2002) 513.

K. Wiik, C.R. Schmidt, S. Faaland, S. Shamsili, M. Einarsrud, T. Grande, *Journal of the American Ceramic Society*, **82** (1999) 721.

R. Wilkenhoener, R. Vassen, H.P. Buchkremer, D. Stover, *Journal of Materials Science*, **34** (1999) 257.

J.W. Yan, Z.G. Lu, Y. Jiang, Y.L. Dong, C.Y. Yu and W.Z. Li, *Journal of the Electrochemical Society*, **149** (2002) A1132.

H. Yokokawa, N. Sakai, T. Horita and K. Yamaji, *Fuel Cells*, **1** (2001) 117.

I. Zhitomirsky, A. Petric, *Journal of Materials Science*, **39** (2004) 825.

3.9.References

---

1 Minimum requirements for Industrial teams. Solid State Energy Conversion Alliance (SECA) website Retrieved June 14, 2004 from the World Wide Web: http://www.seca.doe.gov.

2 *Fuel Cell Handbook, 6th ed.*, EG&G Technical Services Inc., 2002.

3 L. Carrette, K.A. Friedrich and U. Stimming, *Fuel Cells*, **1** (2001) 5.

4 J. Kim, R. Song, K. Song, S. Syun, D. Shin, H. Yokokawa, *Journal of Power Sources*, **122** (2003) 138.

5 M. Prica, T. Alston, K. Kendall, in Proc. Solid Oxide Fuel Cells V (U. Stimming, S. C. Singhal, H. Tagawa, W. Lehnert Eds.) *The Electrochemical Society Proceedings Series* (1997) 619.

6 H. Negishi, N. Sakai, K. Yamaji, T. Horita, H. Yokokawa, *Journal of the Electrochemical Society*, **147** (2000) 1682.

7 P. Sarkar, D. De, H. Rho, *Journal of Materials Science*, **39** (2004) 819.

8 SOFC membrane. Retrieved June 22, 2004 from the World Wide Web: http://www.fuelcellenergy.com/site/products/sofc/timeline2.html.

9 D. Waldbillig, A. Wood, D.G. Ivey, *Solid State Ionics*, In press.

10 A. Weber and E. Ivers-Tiffee, *Journal of Power Sources*, **127** (2004) 273.

11 I. Villarreal, C. Jacobson, A. Lemming, Y. Matus, S. Visco, L. De Jonghe, *Electrochemical and Solid-State Letters*, **6** (2003) A178.

12 P. Bance, N.P. Brandon, B. Girvan, P. Holbeche, S. O'Dea, B.C.H. Steele, *Journal of Power Sources*, **131** (2004) 86.

13 K. Nomura , Y. Mizutani , M. Kawai , Y. Nakamura , O. Yamamoto, *Solid State Ionics*, **132** (2000) 235.

14 M. Hattori, Y. Takeda, Y. Sakaki, A. Nakanishi, S. Ohara, K. Mukaic, J. Lee, T. Fukui, *Journal of Power Sources*, **126** (2004) 23.

15 W.S. Jang, S.H. Hyun, S.G. Kim, *Journal of Materials Science*, **37** (2002) 2535.

16 S.G. Kim, S.P. Yoon, S.W. Nam, S.H. Hyun, S.A Hong, *Journal of Power Sources*, **110** (2002) 222.

17 S.P.S. Badwal, *Solid State Ionics*, **143** (2001) 39.

18 M. Hirano, T. Oda, *Journal of the American Ceramic Society*, **85** (2002) 1336.

19 V.V. Kharton, F.M. Figueredo, L. Navarro, E.N. Naumovich, A.V. Kovalevsky, A.A. Yaremchnko, A.P. Viskup, A. Carneiro, F.M.B. Marques, J.R. Frade, *Journal of Materials Science*, **36** (2001) 1105.

20 Y. Mishima, H. Mitsuyasu, M. Ohtaki, K. Eguchi, *Journal of the Electrochemical Society*, **145** (1998) 1004.

21 J.W. Yan, Z.G. Lu, Y. Jiang, Y.L. Dong, C.Y. Yu and W.Z. Li, *Journal of the Electrochemical Society*, **149** (2002) A1132.

22 H. Yokokawa, N. Sakai, T. Horita, K. Yamaji, *Fuel Cells*, **1** (2001) 117.

23 J.M. Ralph, A.C. Schoeler, M. Krumpelt, *Journal of Materials Science*, **36** (2001) 1161.

24 K.L. Ley, M. Krumpelt, R. Kumar, J.H. Meiser, I. Bloom, *Journal of Materials Research*, **11** (1996) 1489.

25 S. Taniguchi, M. Kadowaki, T. Yasuo, Y. Akiyama, Y. Miyake, K. Nishio, *Journal of Power Sources*, **90** (2000) 163.

26 P.H. Larsen, P.F. James, *Journal of Materials Science*, **33** (1998) 2499.

27 N. Lahl, D. Bahadur, K. Singh, L. Singheiser, K. Hilpert, *Journal of the Electrochemical Society*, **149** (2002) A607.

28 J. Kim, A.V. Virkar, K. Fung, K. Mehta, S.C. Singhal, *Journal of the Electrochemical Society*, **146** (1999) 69.

29 J. Larminie and A. Dicks, *Fuel Cell Systems Explained*, John Wiley & Sons Ltd., West Sussex, England, 2000.

30 M.J. Jorgensen, S. Primdahl, C. Bagger, M. Mogensen, *Solid State Ionics*, **139** (2001) 1.

31 K Kieveland, M. Einarsrud, C.R. Schmidt, S. Shamsili, S. Faaland, K. Wiik, T. Grande, *Journal of the American Ceramic Society*, **82** (1999) 729.

32 K. Wiik, C.R. Schmidt, S. Faaland, S. Shamsili, M. Einarsrud, T. Grande, *Journal of the American Ceramic Society*, **82** (1999) 721.

33 L. Kindermann, D. Das, D. Bahadur, R. Weiss, H. Nickel and K. Hilpert, *Journal of the American Ceramic Society*, **80** (1997) 909.

34 R.J. Gorte, H. Kim, J.M. Vohs, *Journal of Power Sources*, **106** (2002) 10.

35 S. Park, R. Craciun, J.M. Vohs and R.J. Gorte, *Journal of the Electrochemical Society*, **146** (1999) 3603.

36 H. Kim, S. Park, J.M. Vohs, R.J. Gorte, *Journal of the Electrochemical Society*, **148** (2001) A693.

37 R.J. Gorte, S. Park, J.M. Vohs, C. Wang, *Advanced Materials*, **12** (2000) 1465.

38 H. Kim, J.M. Vohs, R.J. Gorte, *Chemistry Communications*, (2001) 2334.

39 C.M. Reich, A. Kaiser and J.T.S. Irvine, *Fuel Cells*, **1** (2001) 249.

40 R. Maric, S. Ohara, T. Fukui, T. Inagaki, J. Fujita, *Electrochemical and Solid-State Letters*, **1** (1998) 201.

41 H. Kim, C. Lu, W.L. Worrell, J.M. Vohs, R.J. Gorte, *Journal of the Electrochemical Society*, **149** (2002) A247.

42 O.A. Marina, C. Bagger, S. Primdahl, M. Mogensen, *Solid State Ionics*, **123** (1999) 199.

43 A. Kaiser, J.L Bradley, P.R. Slater, J.T.S. Irvine, *Solid State Ionics*, **135** (2000) 519.

44 S. Hui, A. Petric, *Journal of the European Ceramic Society*, **22** (2002) 1673.

45 P. Vernoux, M. Guillodo, J. Fourletier, A. Hammou, *Solid State Ionics*, **135** (2000) 425.

46 J.T.S. Irvine and A. Sauvet, *Fuel Cells*, **1** (2001) 205.

47 S. Tao, J.T.S. Irvine, *Journal of the Electrochemical Society*, **151** (2004) A252.

48 R. Wilkenhoener, R. Vassen, H.P. Buchkremer, D. Stover, *Journal of Materials Science*, **34** (1999) 257.

49 H. Itoh, T. Yamamoto, M. Mori, T. Horita, N. Sakai, H. Yokokawa, M. Dokiya, *Journal of the Electrochemical Society*, **144** (1997) 641.

50 T. Fukui, S. Ohara, K. Mukai, *Electrochemical and Solid State Letters*, **1** (1998) 120.

51 T. Fukui, S. Ohara, M. Naito, K. Nogi, *Journal of Power Sources*, **110** (2002) 91.

52 J.H. Lee, H. Moon, H.W. Lee, J. Kim, J.D. Kim, K.H. Yoon, *Solid State Ionics*, **148** (2002) 15.

53 D. Skarmoutsos, F. Tietz and P. Nikolopoulos, *Fuel Cells*, **1** (2001) 243.

54 Suzuki, Sasaki, Otoshi, Kajimura, Ippommatsu, *Solid State Ionics*, **62** (1993) 125.

55 Y. Matsuzaki, I. Yasuda, *Solid State Ionics*, **132** (2000) 261.

56 D. Waldbillig, A. Wood, D.G. Ivey, Unpublished work.

57 C.M. Chun, J.D. Mumford, T.A. Ramanarayanan, *Journal of the Electrochemical Society*, **147** (2000) 3680.

58 B.C.H. Steele, *Nature*, **400** (1999) 619.

---

59 M. Ihara, C. Yokoyama, A. Abudula, R. Kato, H. Komiyama, K. Yamada, *Journal of the Electrochemical Society*, **146** (1999) 2481.

60 E.P. Murray, T. Tsai, S.A. Barnett, *Nature*, **400** (1999) 649.

61 Y. Li, J. Chen, L. Chang, Y. Qin, *Journal of Catalysis*, **178** (1998) 76.

62 C.M. Finnerty, N.J. Coe, R.H. Cunningham, R.M. Ormerod, *Catalysis Today*, **46** (1998) 137.

63 Y. Jiang, A.V. Virkar, *Journal of the Electrochemical Society*, **148** (2001) A706

64 N. Tikekar, T. Armstrong, A. Virkar, in Proc. Solid Oxide Fuel Cells VIII (S. C. Singhal and M. Dokiya Eds.) *The Electrochemical Society Proceedings Series* (2003) 670.

65 D. Fouquet, A.C. Muller, A. Weber, E. Ivers-Tiffee, *Ionics* **8** (2003) 103.

66 G. Stathis, D. Simwonis, F. Tietz, A. Moropoulou, A. Naoumides, *Journal of Materials Research* **17** (2002) 951.

Chapter 4: Reduction and Oxidation Kinetics of the Ni/YSZ system

Abstract

The reduction and oxidation kinetics of Ni/YSZ anode substrate samples were studied at temperatures between 400 and 850°C using thermogravimetric analysis. The samples followed linear kinetics during reduction and a reduction activation energy of 78 kJ/mol was calculated. Parabolic kinetics were observed for samples oxidized at low temperatures and for low amounts of mass change. A divergence from parabolic kinetics was observed at oxidation temperatures greater than 700°C. An activation energy of 87 kJ/mol for reoxidation was calculated.

Chapter 4: Reduction and Oxidation Kinetics of the Ni/YSZ system 4-1

List of Figures 4-3
List of Tables 4-3

4. Reduction and oxidation kinetics of the Ni/YSZ system 4-4
  4.1. Literature review 4-4
  4.2. Thermogravimetric analysis (TGA) 4-5
  4.3. Sample preparation 4-5
  4.4. Experimental procedure 4-6
    4.4.1. Constant temperature TGA tests 4-6
    4.4.2. Constant temperature ramp rate TGA tests 4-7
  4.5. Microstructural characterization 4-8
  4.6. Results and discussion 4-8
    4.6.1. Constant temperature reduction tests 4-8
    4.6.2. Constant temperature ramp rate reduction tests 4-12
    4.6.3. Constant temperature reoxidation tests 4-16
    4.6.4. Constant temperature ramp rate reoxidation tests 4-18
    4.6.5. SEM analysis 4-22
  4.7. Summary 4-23
  4.8. Appendices 4-24
    4.8.1. Appendix 4-1: Mass changes upon redox cycling 4-24
  4.9. References 4-26

List of Figures

Figure 4-1: Schematic diagram of a TGA sample. 4-6
Figure 4-2: Image of the TGA setup. 4-6
Figure 4-3: TGA curves for constant temperature reduction tests. 4-10
Figure 4-4: Arrhenius plots for reduction tests. 4-11
Figure 4-5: TGA curves for constant temperature ramp rate reduction tests. 4-12
Figure 4-6: Derivative of the reduction mass change curve vs temperature for different ramp rates. 4-14
Figure 4-7: Plots of $\ln(\alpha/T_m^2)$ vs $1/T$ for T_m values for Ni reduction. 4-15
Figure 4-8: Kinetic plots for constant temperature oxidation tests. 4-17
Figure 4-9: Arrhenius plot for oxidation tests 4-18
Figure 4-10: TGA curves for the constant temperature ramp rate oxidation 4-18
Figure 4-11: Derivative of the oxidation mass change curve vs temperature for different ramp rates. 4-19
Figure 4-12: Plots of $\ln(\alpha/T_m^2)$ vs $1/T_m$ for Ni oxidation. 4-20
Figure 4-13: SEM BSE image TGA samples. 4-22

List of Tables

Table 4-1: Summary of TGA testing conditions 4-8
Table 4-2: NiO reduction activation energy 4-11
Table 4-3: Activation energy from constant temp ramp rate calculations 4-15
Table 4-4: Literature values of NiO reduction activation energy (E_a) 4-16
Table 4-5: Ni oxidation activation energy values 4-20
Table 4-6: Literature values of Ni oxidation activation Energy (E_a) 4-21

4. Reduction and oxidation kinetics of the Ni/YSZ system

Many intermediate temperature (600°C to 800°C) solid oxide fuel cell (SOFC) systems rely on an anode supported design. [1,2] Typical SOFC anodes are fabricated from a nickel oxide/yttria-stabilized zirconia (YSZ) ceramic composite and are reduced in-situ, during operation, to form a Ni/YSZ cermet. Nickel is used as the electrically conductive component of the anode, because it has excellent catalytic activity for CO and H_2 oxidation, electrical conductivity, and mechanical properties, and is relatively inexpensive. [3,4,5] However, the nickel component of the anode may reoxidize in a commercial SOFC system for various reasons, such as the disruption of the fuel supply at operating temperatures. In order to use a reoxidized cell, it must be reduced once more. Thus, cyclic reduction and oxidation (redox) of the anode can occur during SOFC operation.

Since this redox cycling problem will be present in any commercially viable system, a study of the reduction and oxidation kinetics of the NiO/YSZ system will provide valuable insight into the behaviour of SOFC anodes during redox cycling. This chapter discusses the results of thermogravimetric analyses (TGA) of the redox properties of anode-supported SOFC's and the activation energies for both reduction and oxidation calculated from these measurements.

4.1. Literature review

There have been relatively few studies investigating the reduction and oxidation kinetics of the Ni/YSZ system, [6,7,8] but it may be assumed that its reduction and oxidation behaviour will be similar to the well-studied Ni system. Due to the particle size and morphology of the Ni/YSZ samples tested, the kinetics will likely be most similar to studies using Ni particle samples rather than bulk slabs.

The vast majority of studies agree that NiO reduction is first order and the rate has a linear dependence with the partial pressure of hydrogen. [6,9,10] However, Ni oxidation seems to be more complicated especially at temperatures less than 1000°C. Ni oxidation generally follows a parabolic trend at temperatures greater than 1000°C with activation energies typical of the outward bulk diffusion of Ni in NiO. However, at temperatures less than 1000°C many studies have observed that the kinetics tend to diverge from parabolic kinetics and the activation energy for reoxidation decreases. [8,11,12,13,14,15,16,17] This trend indicates that a short-circuiting mechanism, such as transport along grain boundaries and/or dislocations, begins to dominate the kinetics at temperatures less than 1000°C. This observation is supported by the fact that Ni oxidation kinetics seem to be very sensitive to the preparation procedures, especially surface preparation, grain/particle size and impurity levels. Different impurity levels and preparation procedures will lead to a different concentration of short-circuit paths and might explain the large spread in literature values of oxidation activation energy. Divergence from parabolic rates may be caused by inward diffusion of oxygen along grain boundaries, the gaseous transport of oxygen through transient microfissures or grain growth within the film during oxidation, which reduces the number of grain boundaries and thus the amount of grain boundary diffusion.

4.2. Thermogravimetric analysis (TGA)

Thermogravimetric analysis (TGA) investigates the mass change that occurs as a function of time, temperature, or gas atmosphere. TGA was used in this study to monitor the reduction and oxidation kinetics of NiO/YSZ anode substrate samples and reduction and oxidation activation energies will be calculated from TG information.

4.3. Sample preparation

NiO/YSZ TGA samples were fabricated with a coarse microstructure corresponding to the typical microstructure of an anode substrate. Samples were made from powders with a NiO content of 57 wt%. Powders were dispersed to form a slurry, followed by milling to get the proper particle size and morphology and to thoroughly mix the components. After grinding and mixing, the slurry was tape cast to form samples approximately 1 mm in thickness. After tape casting the samples were dried and then sintered in air. Figure 4-1 shows a schematic diagram of a TGA sample.

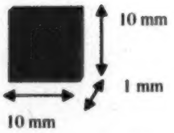

Figure 4-1: Schematic diagram of a TGA sample.

4.4. Experimental procedure

A SETARAM Setsys TGA/TMA system was used for all TGA. TGA was performed in a platinum crucible.

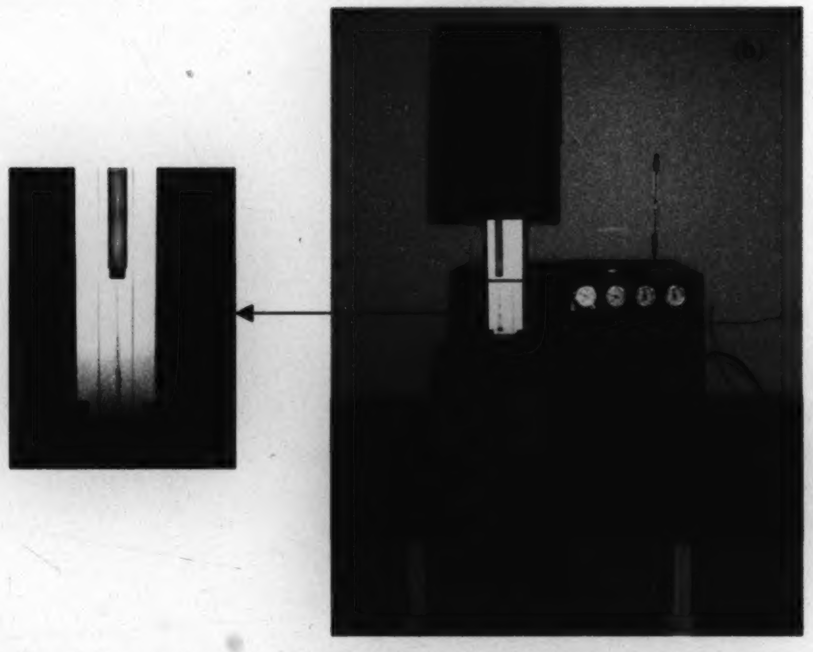

Figure 4-2: a) Close up view of the TGA experimental setup with a Pt crucible; b) image of the overall TGA setup.

Two types of TGA tests were performed: constant temperature reduction/oxidation tests and constant temperature ramp rate reduction/oxidation tests.

4.4.1. Constant temperature TGA tests

During constant temperature tests, samples were heated in an inert atmosphere to the temperature of interest and then were reduced/oxidized at that temperature.

Constant temperature reduction tests were performed at temperatures between 500 and 850°C in 4% H_2 (96% N_2). Ar flow rates of 10 mL/min and 4% H_2 flow rates of 30 mL/min were used for all reduction tests. Oxidation constant temperature TGA was performed at temperatures between 400 and 850°C in air. Ar flow rates of 10 mL/min and air flow rates of 30 mL/min were used for all tests. All oxidation TGA samples were reduced in 4% H_2 (96% N_2) at 850°C for a period of 12 hours before testing.

The following experimental procedure was followed for constant temperature TGA:

1. The sample was heated to the temperature of interest at 10°C/min in Ar.
2. The sample was held at the desired temperature in 4% H_2 (96% N_2) or air until completely reduced/oxidized (as determined by the mass change).
3. The sample was cooled to room temperature in 4% H_2 (for reduction) or air (for oxidation) at a rate of 30°C/min.

During constant temperature tests the sample was heated in an inert atmosphere (Ar) in order to prevent premature oxidation/reduction during heat up. Thus readings taken during the first five minutes of the constant temperature hold may contain significant errors due to the finite amount of time required to change the gas in the furnace chamber from Ar to the reducing/oxidizing gas and instability in the measurements taken during the gas change due to changing flow rates.

4.4.2. Constant temperature ramp rate TGA tests

In order to validate the results of the constant temperature tests and to remove errors introduced due to gas changes during the constant temperature tests, constant temperature ramp rate tests were performed. During these tests, reduced/oxidized samples were heated to temperature at a constant ramp rate in a reducing/oxidizing atmosphere. For reduction tests the samples were heated to 950°C in 4% H_2 (96% N_2) at flow rates of 23 mL/min. For oxidation tests the samples were heated to 1000°C in air at flow rates of 25 mL/min. Ramp rates between 1 and 10°C/min were used for the tests. A summary of the TGA test conditions is shown in Table 4-1.

Table 4-1: Summary of TGA testing conditions

Test	Section	[illegible] Rate	Gas type	[illegible]	[illegible]
Constant temperature (reduction)	Heat up	10	Ar	10	20 to hold temperature
	Hold	-	4% H_2 in N_2	30	500 to 850
	Cool down	30	4% H_2 in N_2	30	Hold temperature to 20
Constant temperature (oxidation)	Heat up	10	Ar	10	20 to hold temperature
	Hold	-	Air	30	400 to 850
	Cool down	30	Air	30	Hold temperature to 20
Constant temperature ramp rate (reduction)	Heat up/Cool down	1 to 10	4% H_2 in N_2	23	20 to 950
Constant temperature ramp rate (oxidation)	Heat up/Cool down	1 to 10	Air	25	20 to 1000

4.5. Microstructural characterization

Scanning electron microscopy (SEM) was used to characterize the microstructural changes that occurred after redox cycling. All SEM images were taken using a LEO 1450 variable pressure SEM operating at 15kV with an Oxford Instruments ultra thin window (UTW) energy-dispersive x-ray (EDX) spectrometer.

4.6. Results and discussion

4.6.1. Constant temperature reduction tests

If nickel reduction follows linear kinetics, a plot of the mass change versus time should be linear with the slope of the line corresponding to the linear rate constant (k). This relation is given in Equation 4-1. The most common practice to find k is to take the slope at the point where the graph is most linear, usually at about 50% conversion. [9]

$$C = kt \qquad \text{Equation 4-1}$$

where: C is the mass change (%)
k is the linear rate constant (%/s)
t is time (s)

Plots of normalized mass change versus time are shown in Figure 4-3. The mass change values were normalized with respect to the theoretical maximum amount of mass change that should occur upon oxidation or reduction. A value of 0 corresponds to an initial condition of 0% reduction or oxidation while a value of 1 corresponds to the condition where the sample is fully reduced or oxidized. During reduction a 57 wt% NiO/YSZ sample should decrease in mass by 12.2%. After oxidation the Ni/YSZ sample should increase in mass by 13.9%. (See Appendix 4-1 for calculations.) The plots show a linear trend at high temperatures (>750°C) and for low mass changes. At lower temperatures (500-750°C) the plots are linear for low mass changes (0.2-0.5), but for larger mass changes there was a divergence from linear behaviour. This divergence, especially at large values of mass change, suggests a change in reaction mechanism. This change may mean that NiO areas are becoming more difficult to reach, i.e., the areas surrounding the NiO become more dense or the porosity more tortuous, which inhibits H_2O removal and thus decreases the reduction rate. [9]

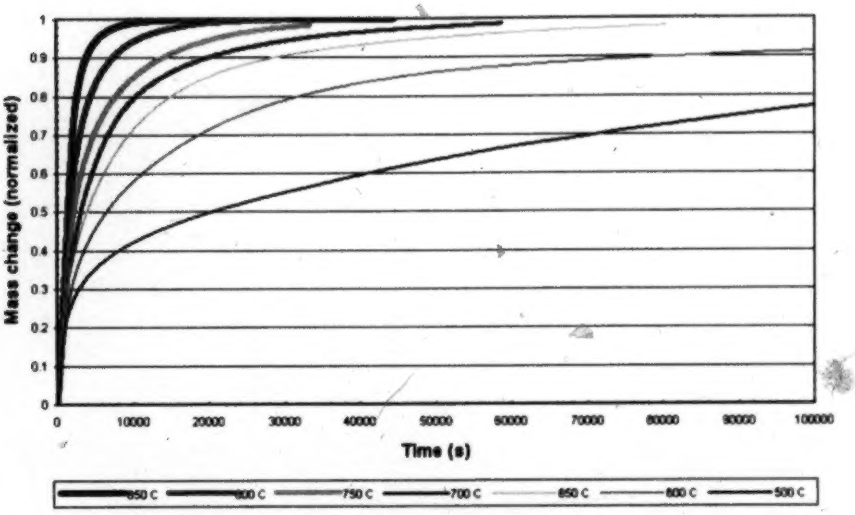

Figure 4-3: TGA curves for constant temperature reduction tests.

The Arrhenius equation (Equation 4-2) can be used to describe the relationship between activation energy, temperature and reduction/oxidation rates.

$$k = k_o e^{\frac{-E_A}{RT}} \qquad \text{Equation 4-2}$$

where: k is the reduction/oxidation rate
k_o is the rate constant
E_a is the activation energy (J/mol)
R is the universal gas constant (8.314 J/mol K)
T is the temperature (K)

The rate constant, k, was determined for normalized mass changes of 0.50, 0.65 and 0.80. By plotting the natural logarithms of these k values versus 1/T in (Figure 4-4) activation energies (E_a) can be calculated from the slope of the line. These values are summarized in Table 4-2. The activation energy appears to increase as the amount of reduction increases, which may indicate that NiO areas become more difficult to reach as the amount of reduction increases.

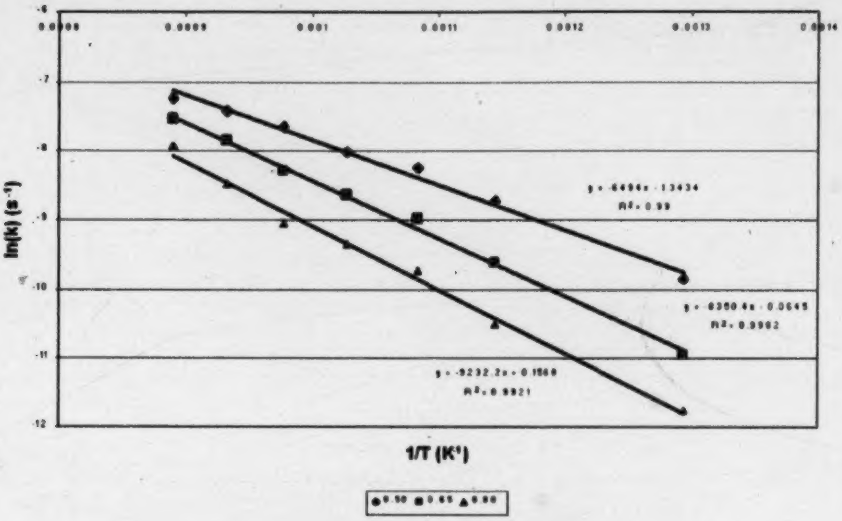

Figure 4-4: Arrhenius plots for reduction tests.

Table 4-2: NiO reduction activation energy

[illegible]	[illegible]	[illegible]
0.50	54	500-850
0.65	69	500-850
0.80	77	500-850

4.6.2. Constant temperature ramp rate reduction tests

Constant temperature ramp rate tests were used to confirm the activation energy values and to determine the minimum temperature at which reduction occurs. These tests are summarized in Figure 4-5.

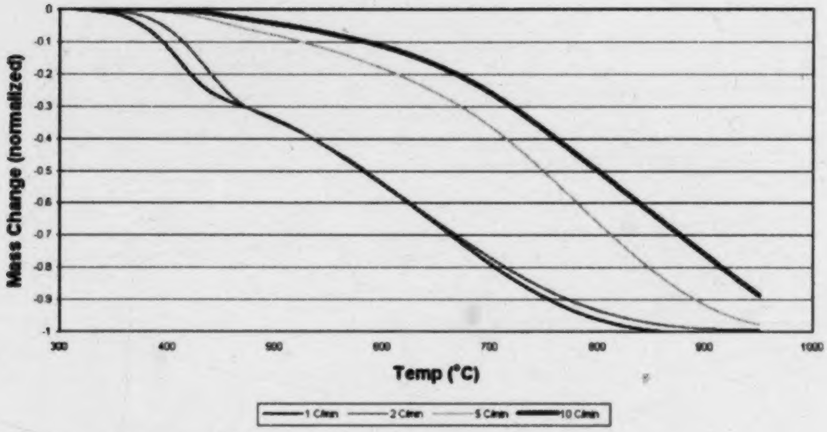

Figure 4-5: TGA curves for the constant temperature ramp rate reduction tests.

Figure 4-5 shows that no reduction occurs until temperatures exceed 300°C and that reduction is very slow until about 375°C. There also appears to be several slope changes that occur during the reduction, which indicates that the reduction rate changes at these temperatures. These slope changes may be related to the variations in calculated activation energies for different amounts of NiO reduction (Table 4-2).

Slope changes during TGA were also reported for NiO/YSZ samples by Fouquet et al. [7] The initial shallower slope (slower reaction) could be attributed to an induction period during which either a nucleation step or, as Fouquet has proposed, chemisorption of H_2 on NiO occurs and the outer surface of the NiO particles reduces to Ni. The second steeper slope (faster rate) corresponds to the autocatalytic condition that occurs after the entire surface has been covered with a thin layer of Ni. During this stage the reaction front progresses inward at a constant rate.

Fouquet et al. compared the reduction of NiO powder to NiO/YSZ bulk ceramics. [7] They found that NiO/YSZ ceramics reduced at a much slower rate and that reduction completion required higher temperatures than NiO powders (>900°C for the bulk ceramics versus ~600°C for the powders), due to the inhibition of transport processes by the YSZ phase. They claim that the process of nickel nucleation on the NiO surface was inhibited by YSZ, as was the progress of the reaction front inside the bulk sample. Thus, NiO/YSZ should have a higher activation energy for reduction than NiO.

The activation energy for NiO reduction for TG tests with a constant temperature ramp rate was calculated using Equation 4-3. [9]

$$\ln\left(\frac{\alpha}{T_m^2}\right) = -\frac{E_a}{RT_m} + \ln\left(\frac{Rk_o}{E_a}\right) \qquad \text{Equation 4-3}$$

where: α is the heating rate (K/min)
T_m is the temperature for the maximum reduction rate (K)
E_a is the activation energy (J/mol)
R is the universal gas constant (8.314 J/mol K)
k_o is the pre-exponential factor in the Arrhenius equation (min^{-1})

If $\ln\left(\frac{\alpha}{T_m^2}\right)$ is plotted against $\frac{1}{T_m}$ the slope will be the value of the activation energy (E_a) divided by the universal gas constant.

The T_m value was taken as the temperature value where the absolute value of the derivative of the weight loss curve (Figure 4-5) is a maximum, as illustrated in Figure 4-6.

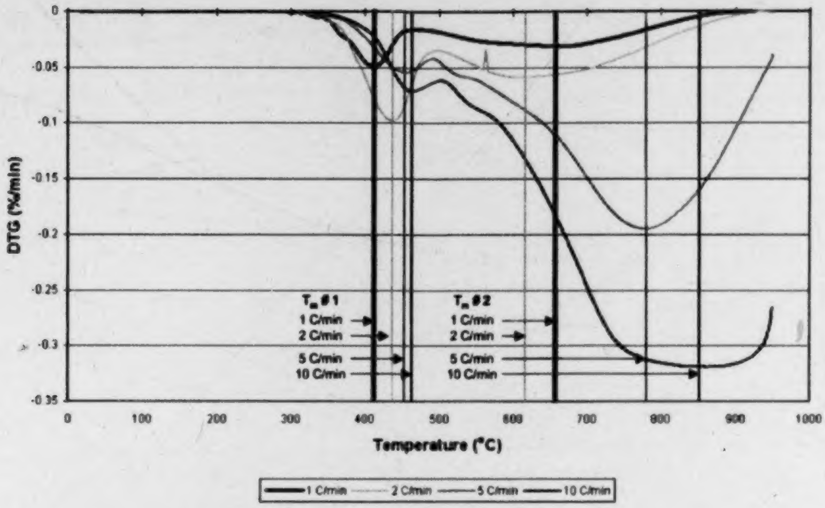

Figure 4-6: Derivative of the reduction mass change curve (DTG) versus temperature for different ramp rates.

Figure 4-6 changes slope several times for a given weight loss curve, which indicates that the limiting reduction mechanism changes for different temperature ranges and ramp rates. The T_m values determined from Figure 4-6 were used in Figure 4-7 to determine the activation energy for reduction. Activation energies for both sets of T_m values were calculated and are summarized in Table 4-3.

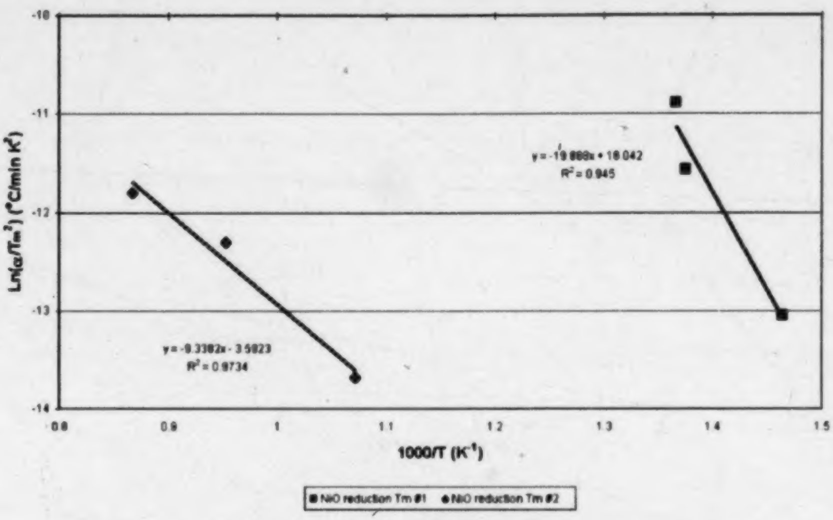

Figure 4-7: Plots of $\ln(\alpha/T_m^2)$ vs 1/T for the 2 sets of T_m values for Ni reduction.

Table 4-3: Activation energy from constant temp ramp rate calculations

NiO reduction (constant temperature)	54-77
NiO reduction 1st slope	165
NiO reduction 2nd slope	78

The activation energy calculated from the first T_m value is quite large (165 kJ/mol). The first peak for slower ramp rates (1 and 2°C/min) is more pronounced compared to faster ramp rates (5 and 10°C/min). The opposite effect occurs, i.e., the second peak is more pronounced, at faster ramp rates (see Figure 4-6). This trend supports the ideas of Fouquet et al. that the initial rate is due to an induction period during which the chemisorption of H_2 on NiO occurs at the outer surfaces of the NiO particles. [7] It would be expected that this induction period would be longer (higher activation energy) and that the duration of this period would decrease at higher temperatures (or faster ramp rates). After this initial induction period, the rate increases (activation energy decreases) and is relatively constant until the majority of reduction occurs. This corresponds to the period where constant inward progress of the reaction front occurs.

There have been many studies of NiO reduction kinetics. The literature work, along with the results from this study, is summarized in Table 4-4.

Table 4-4: Literature values of NiO reduction activation energy (E_a)

Bandrowski et al.	9	Large porous NiO pellet in a packed bed	261-298	52	Linear
Waldbillig et al.	this study	Tape cast NiO/YSZ - constant temperature test	500-850	54-77	Linear
Szekely and Evans	9	Large porous NiO pellet	226-308	65	Linear
Nakajima et al.	9	Powdered NiO sample	277-377	69	Linear
Rao and Rashed	10	Thin NiO slab	300-400	73	Linear
Waldbillig et al.	this study	Tape cast NiO/YSZ -constant temperature ramp rate test	500-950	78	Linear
Richardson et al.	9	Porous NiO powder	220-355	84	Linear
Richardson et al.	9	Porous NiO powder, thin slab	175-300	85	Linear
Tikekar et al.	6	Pressed NiO/YSZ rectangular bar	600-800	94	Linear

4.6.3. Constant temperature reoxidation tests

Nickel oxidation is commonly agreed to approximately follow parabolic kinetics. Therefore, a plot of the mass change versus the square root of time should be linear and the slope of the line should correspond to the parabolic rate constant (k_p). This relation is given in Equation 4-4.

$$C^2 = k_p t \qquad \text{Equation 4-4}$$

where: C is the mass change
k_p is the parabolic rate constant
t is time

Figure 4-8 shows kinetics curves for oxidation. A parabolic trend is apparent at low temperatures, but at high temperatures (>700°C) the curves deviate from parabolic behaviour. At all temperatures deviations from parabolic kinetics also occurred at normalized mass changes higher than ~0.70. Divergence from parabolic trends, especially at temperatures less than 1000°C, has been seen in a number of studies.[8,11-17] In fact, Stathis et al. characterized the oxidation of the Ni/YSZ system as logarithmic in the temperature range of 500-950°C.[8] The divergence from parabolic behaviour is usually attributed to short-circuiting diffusion mechanisms, such as outward Ni diffusion along grain boundaries or dislocations,[11-16] the inward diffusion of oxygen along grain boundaries, the gaseous transport of oxygen through transient microfissures,[16] or grain growth during oxidation which reduces the amount of grain boundary area and thus grain boundary diffusion rates.[11-16]

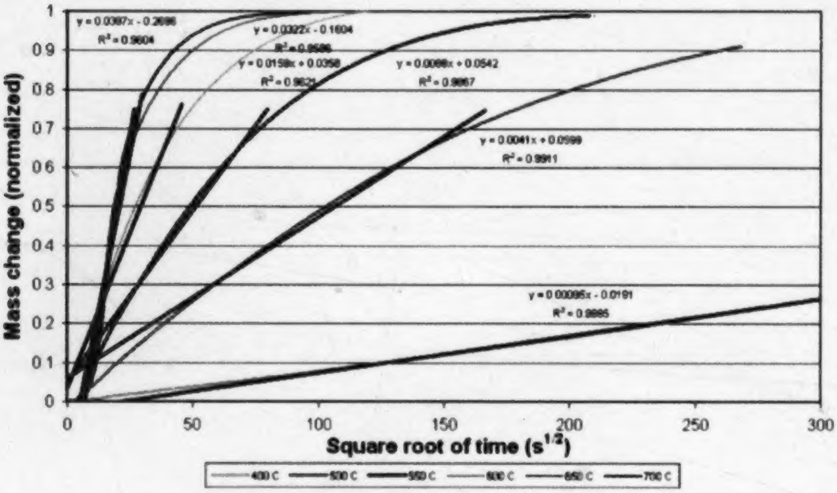

Figure 4-8: Kinetic plots for constant temperature oxidation tests.

It was difficult to get accurate mass change readings at temperatures above 650°C due to the rapidity of the oxidation reaction at these temperatures. The speed of the reaction resulted in an apparent temperature independence in the oxidation rate at temperatures above 650°C. This effect is likely due to experimental setup limitations. Since the sample is heated in Ar, there will be a finite amount of time required to change the gas from Ar to air in the furnace chamber. There is also some instability in measurements during the gas change. The extreme speed of oxidation at temperatures above 650°C results in oxidation being mostly finished before the gas change instabilities are corrected. Therefore, initial readings taken at temperatures above 650°C contain significant errors.

An Arrhenius plot was used to calculate an activation energy for oxidation (Figure 4-9); an activation energy (E_a) for oxidation of 92 kJ/mol was calculated.

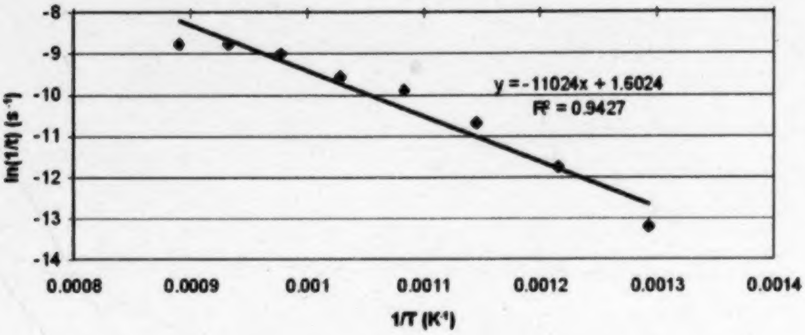

Figure 4-9: Arrhenius plot for oxidation tests.

4.6.4. Constant temperature ramp rate reoxidation tests

Constant temperature ramp rate TG tests were again used to confirm the activation energy value and to determine the minimum temperature at which oxidation will occur. These tests are summarized in Figure 4-10.

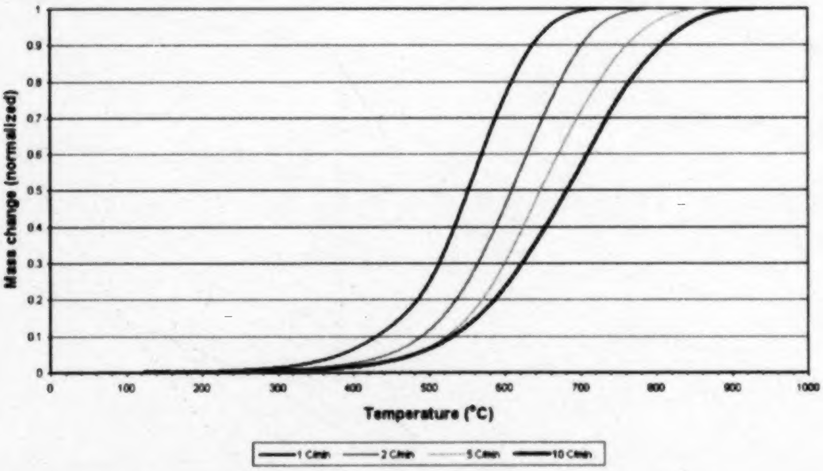

Figure 4-10: TGA curves for the constant temperature ramp rate oxidation tests.

Figure 4-10 shows that no oxidation occurs until above 300°C and that oxidation is very slow until 450-550°C depending on the temperature ramp rate.

There are no major slope changes during the main reoxidation step (middle part of the graph), which indicates that the oxidation rate does not change until diffusional effects become limiting at high values of mass change.

The T_m value for reoxidation was calculated in the same fashion as for reduction, where T_m is the temperature value where the absolute value of the derivative of the weight loss curve is a maximum (Figure 4-11). Only one maximum for each heating rate was obtained. The values of T_m determined from Figure 4-11 were then plotted in Figure 4-12 to determine the activation energy for oxidation; activation energies for Ni oxidation are summarized in Table 4-5.

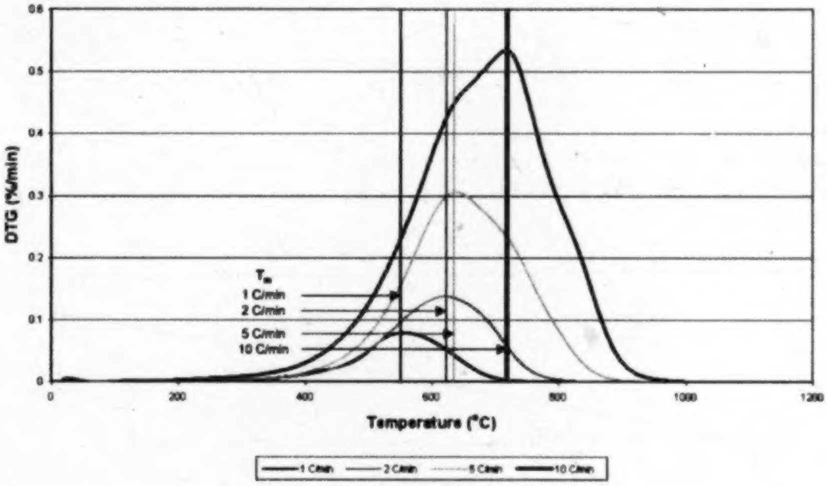

Figure 4-11: Derivative of the oxidation mass change curve versus temperature for different ramp rates.

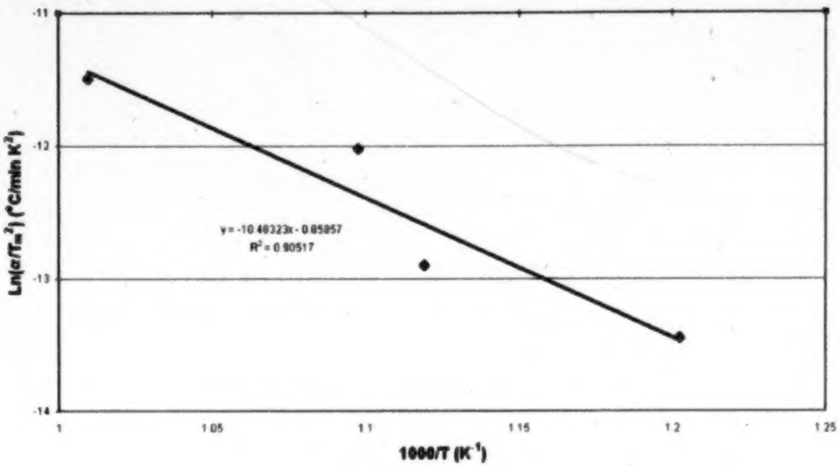

Figure 4-12: Plots of $\ln(\alpha/T_m^2)$ vs $1/T_m$ for Ni oxidation.

Table 4-5: Ni oxidation activation energy values

Ni oxidation (constant temperature)	92
Ni oxidation (constant temperature ramp rate)	87

Fouquet et al. performed TGA while redox cycling a NiO/YSZ cermet heated to 1100°C at a constant temperature ramp rate of 10°C/min. They obtained a very steep, constant slope upon reoxidation, which is consistent with the results seen in this study. [7]

There are very few studies looking at the oxidation of the Ni/YSZ system. According to some sources, it appears that Ni/YSZ oxidizes at a much faster rate than pure Ni powder. [7] Therefore, the activation energy value for Ni/YSZ oxidation is expected to be somewhat lower than that for Ni oxidation. Literature Ni oxidation activation energy values, as well as those determined in this study, are summarized in Table 4-6.

Table 4-6: Literature values of Ni oxidation activation Energy (E_a)

[illegible]	Reference	[illegible]	[illegible]	[illegible]	Kinetics
Suwanwatana et al.	12	Ni particles – 79 nm diameter	250-350	150	Deviation from parabolic
Suwanwatana et al.	12	Ni particles - 0.7 μm diameter	250-350	127	Deviation from parabolic
Suwanwatana et al.	12	Ni particles - 3 μm diameter	250-350	108	Deviation from parabolic
Karmhag et al.	13	Ni particles - 15 nm diameter	135-235	129	Deviation from parabolic
Waldbillig et al.	this study	Tape cast NiO/YSZ - Constant temperature test	400-850	92	Deviation from parabolic
Waldbillig et al.	this study	Tape cast NiO/YSZ - Constant temperature ramp rate test		87	Deviation from parabolic
Karmhag et al.	15	Ni particles - 5 μm diameter	300-700	145	Deviation from parabolic
Tikekar et al.	6	Pressed NiO/YSZ bars	650-800		Parabolic
Fouquet et al.	7	Screen printed NiO/YSZ on YSZ electrolyte			
Stathis et al.	8	Coat mix process - Ni/YSZ	550-650		Logarithmic
Karmhag et al.	14	Ni particles - 158 μm diameter	500-700	183	Deviation from parabolic
Peraldi et al.	11	Polycrystalline bulk Ni - Mechanically polished	450-1000		Deviation from parabolic
Czerwinski and Smeltzer	17	Polycrystalline Ni with CeO_2 - Mechanically polished	600-800	88±17	
Czerwinski and Smeltzer	17	Polycrystalline Ni with CeO_2 - Chemically polished	600-800	100±25	
Haugsrud	16	Polycrystalline Ni – Mechanically polished	500-800	150	Deviation from parabolic
Karmhag et al.	14	Ni particles - 158 μm diameter	800-1200	116	Deviation from parabolic
Haugsrud	16	Polycrystalline Ni – Mechanically polished	1100-1300	200	Parabolic
Peraldi et al.	11	Polycrystalline bulk Ni - Mechanically polished	1000-1200	200±5	Parabolic

4.6.5. SEM analysis

SEM was used to characterize the microstructural changes that occurred after redox cycling. Figure 4-13 shows BSE SEM images of the as prepared (oxidized), reduced and reoxidized microstructures. The YSZ phase is light in colour, with a grain size less than 1 μm, while Ni and NiO particles appear grey and are several microns in size. Areas of porosity are black in the images. After reduction the porosity increases, which is consistent with the NiO volume decrease that should occur upon reduction. After reoxidation, the NiO grains appear spongy with much smaller pores than for the as prepared samples.

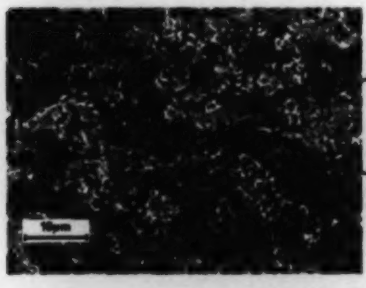

Figure 4-13a: SEM BSE image of an as prepared sample (oxidized).

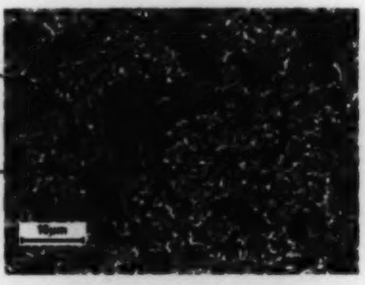

Figure 4-13b: SEM BSE image of a reduced sample.

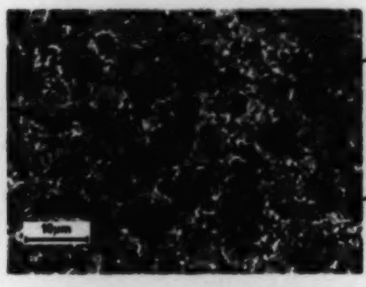

Figure 4-13c: SEM BSE image of a reoxidized sample.

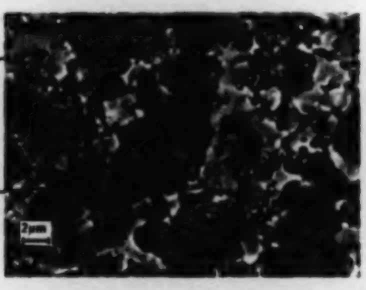

Figure 4-13d: SEM BSE image of the reoxidized sample in (c) at higher magnification.

4.7.Summary

The reduction and oxidation behaviour of tape cast NiO/YSZ ceramics were studied at temperatures between 400 and 850°C. Thermogravimetric analysis was used to examine the reduction and oxidation kinetics of the NiO/YSZ system. Activation energy values of 78 kJ/mol for reduction and 87 kJ/mol for reoxidation were determined. It was confirmed that reduction followed linear kinetics and that reoxidation followed parabolic kinetics at low temperatures and for low amounts of mass change. A divergence from parabolic kinetics was seen at higher temperatures (700 to 850°C) for reoxidation. This divergence has been seen in many other studies for the temperature range studied and is attributed to a combination of outward Ni short-circuit diffusion (e.g., grain boundary diffusion), inward oxygen diffusion through grain boundaries, or gaseous transport of oxygen through transient microfissures.

SEM was used to characterize the microstructure of the as prepared (oxidized), reduced and reoxidized samples. The NiO component of the reoxidized coarse structured samples appeared spongy with many small pores within the NiO particles, indicating that there is a microstructural change on redox cycling.

4.8. Appendices

4.8.1. Appendix 4-1: Mass changes for a 57 wt% NiO / 43 wt% 8YSZ sample upon redox cycling

$$\text{Mass change} = \frac{\Delta m}{m_i} = \frac{m_f - m_i}{m_i}$$

where: m_f is the final mass (g)
m_i is the initial mass (g)

Table 1: Physical data used for calculation

[illegible]	[illegible]	[illegible]
Ni	58.7	0%
NiO	74.7	57%
8YSZ	-	43%

For reduction: $NiO \rightarrow Ni + {}^{1}\!/_{2}O_2$ (1)

For oxidation: $Ni + {}^{1}\!/_{2}O_2 \rightarrow NiO$ (2)

Let the oxidized cell weight be: x
Then the NiO weight is: $m_{NiO} = 0.57x$
And the 8YSZ weight is: $m_{YSZ} = 0.43x$

From Reactions (1) and (2) it can be seen that the number of moles of NiO will be equal to the number of moles of Ni for both reduction and oxidation.

Therefore: $\text{moles NiO} = \dfrac{0.57x}{MW\ \ NiO} = \text{moles Ni}$

Then the weight of Ni in the reduced cell is: $m_{Ni} = \dfrac{0.57x * MW\ \ Ni}{MW\ \ NiO}$

So the total oxidized weight is: $m_{ox} = m_{YSZ} + m_{NiO} = x$
And the total reduced weight is: $m_{red} = m_{YSZ} + m_{Ni}$

For reduction: $m_f = m_{red}$
$m_i = m_{ox}$

Therefore if: $\text{Mass change} = \dfrac{\Delta m}{m_i} = \dfrac{m_f - m_i}{m_i} = \dfrac{m_{red} - m_{ox}}{m_{ox}}$

$$\text{Mass change} = \frac{\left(0.43x + \dfrac{0.57x * \text{MW Ni}}{\text{MW NiO}}\right) - x}{x}$$

Filling in the numbers and canceling out x

$$\text{Mass change} = \frac{\left(0.43 + \dfrac{0.57 * 58.7}{74.7}\right) - 1}{1}$$

Mass change = -0.122

Upon reduction a mass decrease of 12.2% occurs.

For oxidation: $m_i = m_{red}$

$m_f = m_{ox}$

Therefore if: $\text{Mass change} = \dfrac{\Delta m}{m_i} = \dfrac{m_f - m_i}{m_i} = \dfrac{m_{ox} - m_{red}}{m_{red}}$

$$\text{Mass change} = \frac{x - \left(0.43x + \dfrac{0.57x * \text{MW Ni}}{\text{MW NiO}}\right)}{\left(0.43x + \dfrac{0.57x * \text{MW Ni}}{\text{MW NiO}}\right)}$$

Filling in the numbers and canceling out x

$$\text{Mass change} = \frac{1 - \left(0.43 + \dfrac{0.57 * 58.7}{74.7}\right)}{\left(0.43 + \dfrac{0.57 * 58.7}{74.7}\right)}$$

Mass change = 0.139

Upon oxidation the mass increases by 13.9%.

4.9. References

1 L.G.J. de Haart, K. Mayer, U. Stimming & I.C. Vinke, *Journal of Power Sources* **71** (1998) 302.

2 D. Simwonis, A. Naoumidis, F.J. Dias, J. Linke & A. Moropoulou, *Journal of Materials Research* **12** (1997) 1508.

3 J.M. Ralph, A.C. Schoeler & M. Krumpelt, *Journal of Materials Science* **36** (2001) 1161.

4 S.P.S. Badwal, *Solid State Ionics* **143** (2001) 39.

5 J.H. Lee, H. Moon, H.W. Lee, J. Kim & K.H. Yoon, *Solid State Ionics* **148** (2002) 15.

6 N. Tikekar, T. Armstrong, A. Virkar, in Proc. Solid Oxide Fuel Cells VIII (S. C. Singhal and M. Dokiya Eds.) *The Electrochemical Society Proceedings Series* (2003) 670.

7 D. Fouquet, A.C. Muller, A. Weber, E. Ivers-Tiffee, *Ionics* **8** (2003) 103.

8 G. Stathis, D. Simwonis, F. Tietz, A. Moropoulou, A. Naoumides, *Journal of Materials Research* **17** (2002) 951.

9 J.T. Richardson, R. Scates, M. Twigg, *Applied Catalysis A: General* **246** (2003) 137.

10 Y.K. Rao, A.H. Rashed, *Trans. Instn. Min. Metall* **110** (2001) C1.

11 R. Peraldi, D. Monceau, B. Pieraggi, *Oxidation of Metals* **58** (2002) 275.

12 W. Suwanwatana, S. Yarlagadda, J.W. Gillespie, *Journal of Materials Science* **38** (2003) 565.

13 R. Karmhag, G. Niklasson, M. Nygren, *Journal of Applied Physics* **89** (2001) 3012.

14 R. Karmhag, G. Niklasson, M. Nygren, *Journal of Materials Research* **14** (1999) 3051.

15 R. Karmhag, G. Niklasson, M. Nygren, *Journal of Applied Physics* **85** (1999) 1186.

16 R. Haugsrud, *Corrosion Science* **45** (2003) 211.

17 F. Czerwinski and W.W. Smeltzer, *Journal of the Electrochemicial Society* **140** (1993) 2606.

Chapter 5: Volume changes caused by reduction and oxidation of the Ni/YSZ system

Abstract

Ni reduction and oxidation should result in large bulk volume changes. These volume changes may have a significant effect on the integrity of interfaces within a SOFC. Thermomechanical analysis was used to measure the amount of volume change that Ni/YSZ sample exhibited during reduction and oxidation. Two types of samples were tested: one sample type had relatively coarse microstructure similar to the anode substrate while the other sample type had fine microstructure similar to the AFL. Anode substrate samples exhibited no change in dimensions after reduction or oxidation at 750°C. AFL samples did not change dimensions during reduction, but expanded by over 2% after oxidation at 750°C. AFL samples were severely cracked after oxidation. AFL samples oxidized at lower temperatures or containing lower amounts of Ni expanded and cracked less than standard samples during oxidation.

Chapter 5: Volume changes caused by reduction and oxidation of the Ni/YSZ system 5-1

List of Figures 5-3
List of Tables 5-3

5. Volume changes caused by reduction and oxidation of the Ni/YSZ system 5-4
  5.1. Thermomechanical analysis (TMA) 5-4
  5.2. Sample preparation 5-4
  5.3. Experimental procedure 5-6
  5.4. Microstructural characterization 5-7
  5.5. Results and discussion 5-7
    5.5.1. Coarse structured anode samples 5-7
    5.5.2. Fine structured anode samples 5-8
    5.5.3. Literature results 5-11
    5.5.4. SEM analysis 5-13
  5.6. Summary 5-13
  5.7. References 5-15

List of Figures

Figure 5-1: SEM image of a typical anode-supported SOFC. 5-5
Figure 5-2: Image of the TMA setup. 5-6
Figure 5-3: Reduction and oxidation TMA of the coarse structured anode samples. 5-8
Figure 5-4: Image of a oxidized coarse structured TMA sample. 5-8
Figure 5-5: Reduction TMA of the fine structured anode samples. 5-9
Figure 5-6: Oxidation TMA of fine structured anode samples 5-9
Figure 5-7: Images of an oxidized fine structured TMA sample. 5-11
Figure 5-8: SEM image of a fine structured TMA sample compared to the typical microstructure seen in a SOFC AFL layer. 5-13

List of Tables

Table 5-1: Summary of literature length change values 5-12

5. Volume changes caused by reduction and oxidation of the Ni/YSZ system

The reduction and oxidation of nickel will result in large bulk volume changes. In theory, the bulk volume of a fully dense NiO sample should contract by 40.9% upon reduction and the resulting Ni should expand by 69.2% upon oxidation. (See Appendix 5-1 for calculations) A porous NiO/YSZ SOFC anode will likely not experience such a drastic volume change upon reduction or oxidation due to the rigid YSZ skeleton present to prevent shrinkage and the ability of any volume expansion to be accommodated by the pores within the sample. However, any volume change that does occur may have a significant effect on the integrity of interfaces within a fuel cell and thus result in significant performance degradation.

5.1. Thermomechanical analysis (TMA)

Thermomechanical analysis (TMA) measures the change in sample displacement as a function of temperature, time, atmosphere, or applied force. In constant force TMA tests, a hemispheric probe sits on the sample and exerts a small downward force on it. During the test, the sample expands or contracts and thus changes the force measured by the probe. TMA was used to measure the dimensional changes that occur during reduction and oxidation of two types of NiO/YSZ ceramics, samples with a coarse microstructure similar to typical SOFC anode substrate layers and fine structured samples that are similar to the anode functional layer in a typical SOFC.

5.2. Sample preparation

Two types of NiO/YSZ samples were fabricated, one with a coarse microstructure corresponding to the typical microstructure of a SOFC anode substrate and one with a fine microstructure similar to the typical microstructure for a SOFC anode functional layer (AFL). All tested samples contained only one type of microstructure (coarse or fine) and had no additional layers deposited.

An image showing the microstructure of the anode substrate and AFL in a typical SOFC is shown in Figure 5-1. The anode substrate has much coarser Ni particles and larger pores than the finer structured anode functional layer, which has small well-distributed Ni particles and pores. This difference in Ni particle size, pore size and pore distribution will significantly affect the volume expansion behaviour of the two sample types during redox cycling.

Electrolyte
Anode Functional Layer (AFL)
Anode Substrate

Figure 5-1: SEM BSE image of a typical anode-supported SOFC showing the anode substrate layer (coarse microstructure) and anode functional layer (fine microstructure).

Coarse structured samples were made from powders with a NiO content of 57 wt%. Four different fine structured samples were fabricated from powders with a Ni content of 30, 35, 40 and 57 wt% NiO. Coarse structured powders were dispersed to form a slurry, followed by milling to get the proper particle size and morphology and to thoroughly mix the components. Fine structured samples were dispersed to form a slurry and were ground and then milled to achieve the desired particle size and morphology and to thoroughly mix the components. After grinding and mixing, the slurries were tape cast. TMA samples were fabricated by laminating three tape cast layers together. Sample dimensions were approximately 150mm x 10mm x 3mm. After tape casting the samples were dried and then sintered in air.

5.3. Experimental procedure

A SETARAM Setsys TGA/TMA system was used for all TGA and TMA measurements. TMA used a thin alumina probe with a rounded end. An image of the TMA experimental setup is shown in Figure 5-2.

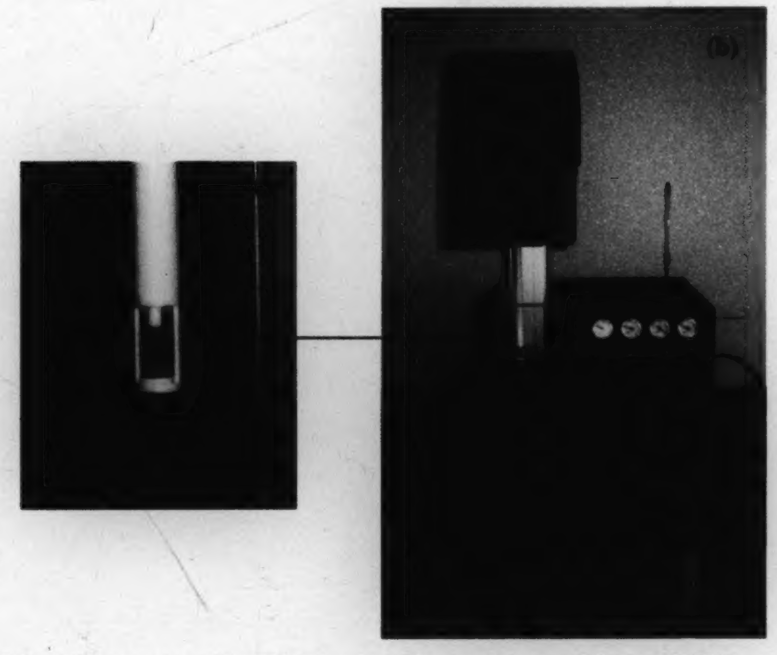

Figure 5-2: a) Close up view of the TMA experimental setup; b) image of the overall TMA setup.

The following experimental procedure was followed for all TMA tests.

1. The sample was loaded with 25 g of weight.
2. It was heated to 600 or 750°C in Ar at a rate of 10°C/min. The Ar flow rate was 15 mL/min.
3. After the desired temperature was reached the furnace atmosphere was changed to either 4% H_2 (96% N_2) for reducing tests or air for oxidizing tests. The sample was held at temperature until complete reduction/oxidation occurred (as determined by the mass change). The flow rate for all gases was 23 mL/min.

4. After the hold the sample was cooled in the same atmosphere as the hold (4% H_2 or air) at a rate of 30°C/min.

Spikes in the TMA measurements occurred at the beginning and end of the constant temperature hold. These spikes are artifacts, likely due to the change in gas flow and temperature ramp rate.

5.4. Microstructural characterization

Scanning electron microscopy was used to confirm that the microstructure of the tested samples resembled the microstructure of a typical SOFC. All SEM images were taken using a LEO 1450 variable pressure SEM operating at 20kV with an Oxford Instruments ultra thin window (UTW) energy-dispersive x-ray (EDX) spectrometer.

5.5. Results and discussion

5.5.1. Coarse structured anode samples

Figure 5-3a and 3b show the amount of displacement, i.e., the volume change that occurs upon reduction and oxidation of the coarse structured anode sample. The figures clearly show that there is basically no change in volume upon either reduction or oxidation at 750°C. This indicates that the rigid YSZ support skeleton counters the large constriction in volume that should occur upon reduction and any oxidation volume expansion is accommodated through internal porosity changes rather than bulk volume change. There was no cracking seen in any of the coarse structured anode TMA samples after reduction or oxidation (Figure 5-4). The initial 0.05-0.2% volume increase in Figure 5-3a and 3b is likely due to the thermal expansion that occurs during the heat up to the reduction/oxidation temperature.

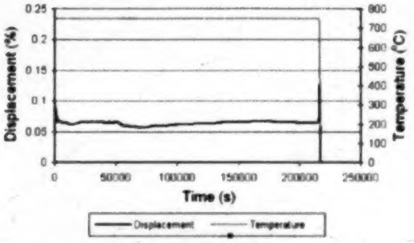

Figure 5-3a: Reduction TMA of a coarse structured anode sample.

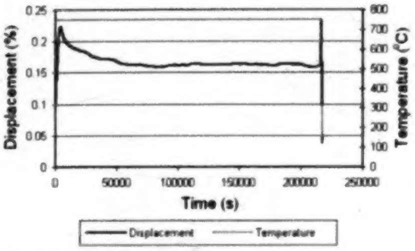

Figure 5-3b: Oxidation TMA of a coarse structured anode sample.

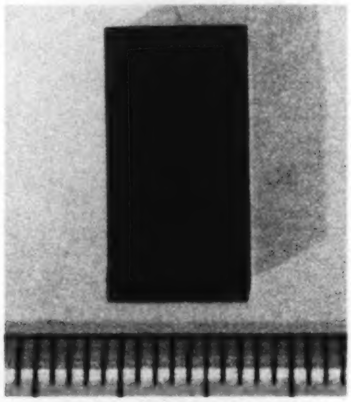

Figure 5-4: Image of an oxidized coarse structured TMA sample. (Graduations are in mm.)

5.5.2. Fine structured anode samples

Figure 5-5 and Figure 5-6 show the amount of displacement that occurs upon reduction and oxidation of the fine structured anode samples. Figure 5-5 shows two tests using a 57 wt% NiO sample, whereas Figure 5-6 includes the coarse microstructured anode substrate for comparison and samples with varying nickel contents (30, 35, 40 wt% NiO).

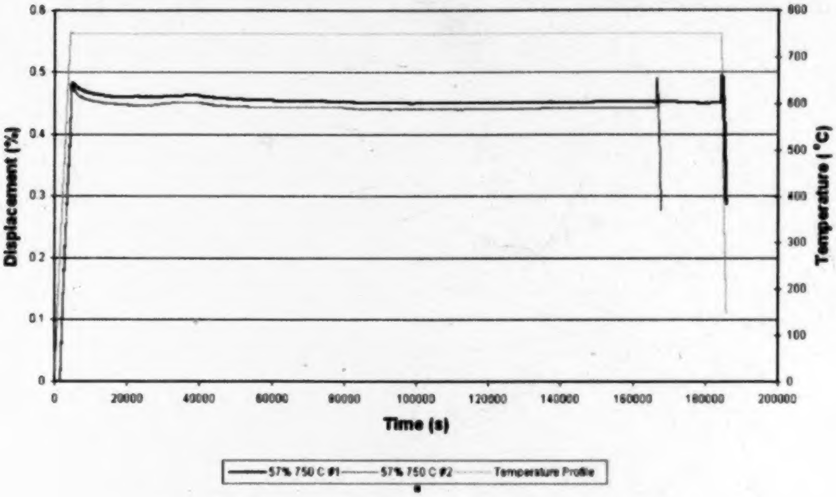

Figure 5-5: Reduction TMA of fine structured anode sample.

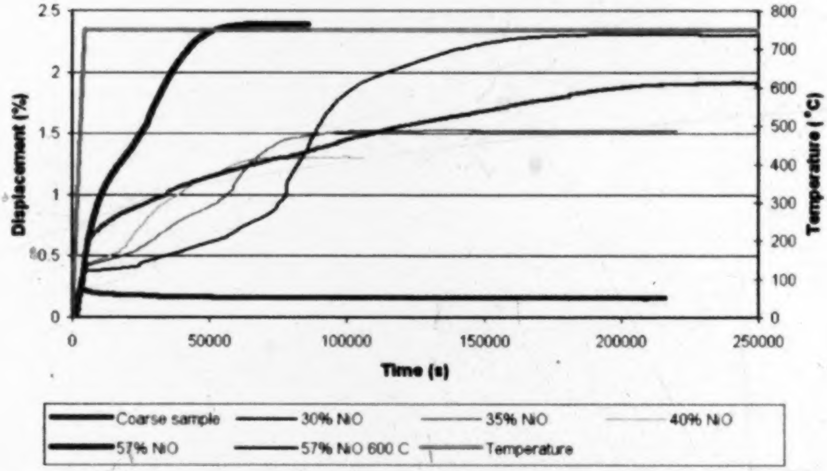

Figure 5-6: Oxidation TMA of fine structured anode sample (with the coarse structured sample as a reference).

After reduction no change in volume or cracking was seen for any of the fine structured samples. However, oxidation at 750°C increased the volume of the 57 wt% NiO sample by 2.0-2.5% while oxidation at 600°C increased the 57 wt% NiO sample volume by 1.5%.

Samples with 30, 35 and 40 wt% NiO were also prepared and tested at 750°C. The 30 wt% sample was slow to oxidize, but expanded nearly as much as the 57 wt% sample. The anomalous behaviour of the 30 wt% sample may be due to the reduced amount of porosity within the sample. The 35 and 40 wt% samples expanded by a much smaller amount than both the 30 and 57 wt% samples upon oxidation. The 40 wt% sample experienced the smallest volume increase of all samples (0.9%).

After oxidation, all the fine structured TMA samples had many cracks (Figure 5-7), which were likely caused by the volume expansion experienced upon oxidation. The fact that fine structured TMA samples expanded and cracked upon oxidation indicates that the small pores in the fine structured samples could not accommodate the amount of Ni volume expansion that occurred during oxidation. The coarse structured TMA samples did not expand or crack, which indicates that the large pores within the sample were able to accommodate the oxidation volume expansion. The sample that was oxidized at 600°C appeared to have fewer cracks than the one oxidized at 750°C, possibly due to the slower rate of oxidation and subsequently lower amount of volume expansion seen at lower oxidation temperatures.

If the cracks formed during testing, there would be some error introduced in the measured expansion values; however, the trend of volume expansion upon oxidation should still be valid. The initial 0.2 to 0.4% volume increase in Figure 5-5 and Figure 5-6 is likely due to the thermal expansion that occurs during the heat up to the reduction/oxidation temperature.

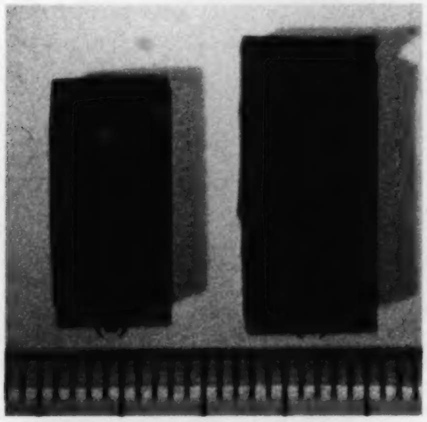

Figure 5-7: Optical microscope images of a) a fine structured TMA sample – oxidized at 600°C and b) a fine structured TMA sample – oxidized at 750°C. (Graduations are in mm.)

5.5.3. Literature results

There have been very few studies investigating the volume changes seen after redox cycling of Ni/YSZ cermets. Even studies examining the same approximate cermet composition can give wildly different results due to differences in sample preparation methods, particle size and morphology, and amount and size of pores present in the sample. This makes it difficult to compare results published by different groups.

Stathis et al. used dilatometry to measure the amount that a 56 wt% NiO / 44 wt% YSZ sample expanded upon oxidation. [1] The sample was fabricated by pressing the powder in a heated metallic die.

The Strathis group found that the length increased by 54% after oxidation at 800°C and 27% after oxidation at 650°C. After oxidation the sample oxidized at 800°C was cracked, while the sample oxidized at 650°C had no cracks. The amount of expansion was significantly higher than the values seen in the present study. This is likely due to the significantly different sample fabrication process, which results in a vastly different microstructure and pore size and distribution.

Fouquet et al. also used dilatometry to examine volume changes that occur as a result of NiO reduction and Ni oxidation in a 65 mol% NiO/ 35 mol% YSZ (~53 wt% NiO / 47 wt% YSZ) ceramic. [2] Samples were prepared by mixing the individual powders together, die pressing them and then sintering them in air.

They found that after redox cycling the samples at 950°C there was no change in length after reduction, but that oxidation caused an increase in length of 0.1 and 0.8% depending on the sintering temperature, particle size of the NiO and YSZ components, the ratio between NiO and YSZ particle sizes and the number of redox cycles. After redox cycling both microcracks in the YSZ matrix and large visible surface cracks were seen. Expansion values were slightly smaller than the results seen for the fine microstructured samples in this study, but are quite similar despite the differences in fabrication methods, particle size and pore size and distribution.

The results from the present study are summarized and compared to Stathis' and Fouquet's results in Table 5-1.

Table 5-1: Summary of literature length change values and values from the present study

Stathis et al.	1	56 wt% NiO / 44 wt% YSZ	1.5	Coat Mix process / pressed powder / sintered in air	650	27	No
Stathis et al.	1	56 wt% NiO / 44 wt% YSZ	1.5	Coat Mix process / pressed powder / sintered in air	800	54	Yes
Fouquet et al.	2	53 wt% NiO / 47 wt% YSZ	0.5	Pressed powder / sintered in air	950	0.4	Yes
Fouquet et al.	2	53 wt% NiO / 47 wt% YSZ	1.4	Pressed powder / sintered in air	950	0.8	Yes
Waldbillig et al.	this study	57 wt% NiO / 43 wt% YSZ	1	Tape cast / lamination / sintered in air	750	2.0 to 2.5	Yes
Waldbillig et al.	this study	57 wt% NiO / 43 wt% YSZ	1	Tape cast / lamination / sintered in air	600	1.5	Yes
Waldbillig et al.	this study	40 wt% NiO / 60 wt% YSZ	1	Tape cast / lamination / sintered in air	750	0.9	Yes
Waldbillig et al.	this study	35 wt% NiO / 65 wt% YSZ	1	Tape cast / lamination / sintered in air	750	1.1	Yes
Waldbillig et al.	this study	30 wt% NiO / 70 wt% YSZ	1	Tape cast / lamination / sintered in air	750	1.9	Yes
Waldbillig et al.	this study	57 wt% NiO / 43 wt% YSZ	5	Tape cast / lamination / sintered in air	750	0	No

5.5.4. SEM analysis

The microstructure of the coarse and fine structured TMA samples were compared to the microstructure of a typical SOFC using an SEM. The structure of both types of samples was very similar to that of typical SOFC components, with similar particle size, porosity and general microstructure. SEM images comparing the microstructure of the fine structured sample to a typical SOFC microstructure are seen in Figure 5-8.

Figure 5-8a: SEM BSE image of the microstructure of a fine structured TMA sample.

2µm
Electrolyte
AFL

Figure 5-8b: SEM BSE image of the typical microstructure seen in a SOFC AFL.

5.6. Summary

The reduction and oxidation behaviour of tape cast NiO/YSZ ceramics was studied at 600°C and 750°C. Thermomechanical analysis showed that coarse structured anode samples experienced no volume change upon reduction or oxidation; however, the fine grained samples increased in volume by 0.9 to 2.5% after oxidation. Decreasing the oxidation temperature or amount of Ni in the sample lowered the amount of oxidation volume expansion in all cases, with the exception of the 30 wt% NiO sample which had a high amount of volume expansion due to its low porosity. The fine structured samples that were oxidized at 750°C had significant amounts of cracking; samples oxidized at 600°C had far fewer cracks.

It would appear from this study that volume expansion of the higher density anode functional layer (AFL) could be a catastrophic failure mechanism when redox cycling anode-supported SOFC's. The stresses that will form in this layer as the nickel component expands upon oxidation, but is constrained by the porous anode substrate and dense electrolyte, may lead to layer delamination or electrolyte cracks. These defects may greatly decrease the performance of the cell. The anode substrate samples studied had high enough porosity to compensate for any volume expansion that occurs.

5.7.References

---

1 G. Stathis, D. Simwonis, F. Tietz, A. Moropoulou, A. Naoumides, *Journal of Materials Research* **17** (2002) 951.
2 D. Fouquet, A.C. Muller, A. Weber, E. Ivers-Tiffee, *Ionics* **8** (2003) 103.

Chapter 6: A baseline characterization of SOFC redox tolerance by electrochemical methods

Abstract

The single cell testing facilities at FCE were used to characterize the baseline electrochemical performance and redox tolerance of standard TSC-2 cells using commercially realistic testing configurations. Two types of electrochemical tests were performed: I-V curves and steady-state hold tests. Cell performance decreased slightly after each redox cycle, but significant degradation did not occur until after the 2 hour redox cycle. After the redox cycles were complete, the overall cell performance degraded by 9.4% for I-V curve tests and by 7.9% for steady-state hold tests. The redox tolerance baseline developed during this testing will be compared against the performance of cells that have been modified to enhance their redox tolerance.

Chapter 6: A baseline characterization of SOFC redox tolerance by electrochemical methods 6-1

List of Figures 6-3
List of Tables 6-3

6. A baseline characterization of SOFC redox tolerance by electrochemical methods 6-4
  6.1. Sample preparation 6-4
  6.2. Test station description 6-6
  6.3. Experimental procedure 6-6
    6.3.1. Heat up and initial reduction 6-7
    6.3.2. Performance characterization 6-7
    6.3.3. Redox cycling 6-8
    6.3.4. Cool down 6-8
  6.4. Results and discussion 6-10
    6.4.1. I-V curves 6-10
    6.4.2. Steady-state holds 6-13
    6.4.3. Verification of redox depth assumptions 6-14
  6.5. Summary 6-15
  6.6. References 6-17

List of Figures

Figure 6-1: TSC-2 cell manufacturing process diagram. 6-5
Figure 6-2: FCE's single cell testing stations. 6-6
Figure 6-3: I-V curves comparing the performance before and after redox cycling. 6-10
Figure 6-4: Summary of the cumulative percent degradation per redox cycle for I-V tests. 6-11
Figure 6-5: Comparison of I-V curves measured before and after steady-state holds. 6-12
Figure 6-6: Steady-state holds comparing the performance before and after redox cycling 6-13
Figure 6-7: Summary of the cumulative percent degradation per redox cycle for the steady-state tests. 6-14
Figure 6-8: Voltage behaviour during oxidation. 6-15

List of Tables

Table 6-1: Summary of the redox testing procedure 6-1

6. A baseline characterization of SOFC redox tolerance by electrochemical methods

A baseline characterization of the electrochemical performance degradation after redox cycling was performed using the single cell testing facilities at Fuel Cell Energy Ltd. (FCE). The test methods and equipment have been developed by FCE over the last five years and provide a very stable and reproducible platform to test the cell's initial performance and baseline the amount of performance degradation that occurs after cyclic reduction and oxidation (redox). During these tests, the cell's initial performance was characterized and then a small amount of air was blown over the anode in order to reoxidize the cell. The cell was then reduced and the electrochemical performance was remeasured.

A redox depth method was developed in order to determine the length of redox times to use. The term redox depth has been defined as the amount of Ni in the anode that will be oxidized over a certain time period by a fixed flow rate of air, i.e., a fixed amount of oxygen. 100% redox depth indicates that enough oxygen has been supplied that 100% of the Ni in the cell should be oxidized. For these redox tests, cells were oxidized to 10, 20, 30, 60 and 100% redox depths. Redox depth calculations can be found in Appendix 3-2.

6.1. Sample preparation

FCE's standard TSC-2 cell manufacturing process is made up of three major unit operations: tape casting, screen printing and co-firing. Figure 6-1 shows the cell manufacturing process diagram.

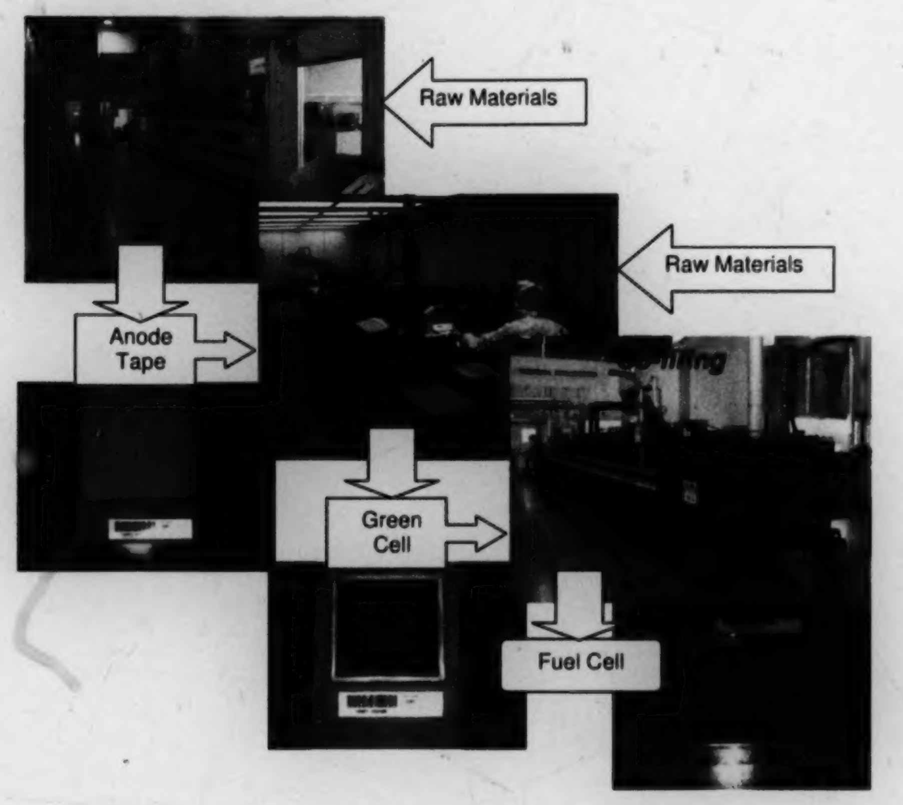

Figure 6-1: TSC-2 cell manufacturing process diagram. [1]

The anode substrate is made via a single layer tape cast process. Powders are dispersed to form a slurry, followed by milling to get the proper particle size and morphology and to thoroughly mix the components. After grinding and mixing, the slurries are tape cast on FCE's 20 m tape caster. The cast tape is dried and then cut into individual pieces.

After the tape is cut, the other fuel cell layers are screen printed onto each anode substrate piece. All subsequent layers (anode functional layer, electrolyte and cathode) are printed directly onto the green (unfired) substrate. After the layers are printed, the tape is cut to the appropriate cell size.

The final processing step involves one-step co-firing of all cell components. This action combines binder burnout, high temperature co-sintering and cooling into a single firing step.

6.2. Test station description

FCE has a number of custom designed single cell test stations (shown in Figure 6-2). Each test stand is fully automated and controlled using Labview and is able to reliably test a fuel cell under a number of conditions. The test configuration for the experiments used stainless steel test jigs with cross flow fuel (H_2) and oxidant (air) delivery. Standard TSC-2 10x10cm (81cm^2 active area) production cells, perovskite cathode contact materials, Ni anode contact materials and tape cast alumina seals were used for all tests. This testing setup provides a commercially realistic testing configuration, as there are no precious metal contact materials or current collectors used, and no special furnace or sealing configurations are required.

Power densities as high as 1.4 W/cm^2 have been achieved at 0.7 V and 750°C using this testing configuration.

Test Stations

Figure 6-2: FCE's single cell testing stations. [2]

6.3. Experimental procedure

Each single cell test consisted of six main steps: heat-up, reduction, current-voltage (I-V) curves, steady state holds, redox cycling and cool down.

6.3.1. Heat up and initial reduction

Tested cells were slowly heated from room temperature to 800°C in N_2. Upon reaching temperature the cell was reduced by introducing H_2 into the anode cavity. During reduction the N_2 flow was gradually decreased and the H_2 flow gradually increased until 2 SLPM of H_2 was flowing. After a period of four hours the cells were completely reduced.

6.3.2. Performance characterization

After reduction the cell temperature was reduced to 750°C and the initial performance was characterized. Two different types of electrochemical tests were used in order to fully characterize the performance: current-voltage (I-V) curves and steady state utilization holds.

6.3.2.1. Current-voltage (I-V) curves

During an I-V curve high fuel and air flows were used and the current was stepped at 2 minute intervals from 0A to 60A (0.74A/cm^2). 4A current steps were used. Tests were performed at 750°C using H_2 fuel with a humidity of 2.5%. These tests have three main purposes:

1. To characterize the OCV of the cell in order to ensure that there is little cross-leak or electronic conductivity in the electrolyte and that there is a good seal between components.
2. To measure the final performance of the cell at 60A.
3. To examine the shape of the curve in order to roughly determine the amount of activation, ohmic and mass transport losses and whether the proportion of each type of loss changes after redox cycling.

6.3.2.2. Steady-state utilization holds

A steady-state utilization hold is performed to examine the electrochemical performance of the cell at a fixed current and fuel/air utilization. The tests were performed at 750°C and 40.5A (0.5 A/cm^2) in H_2 with 2.5% humidity. A fuel utilization of 54% and air utilization of 27% was used for the tests. The current was stepped at five-second intervals, in 0.5A steps, to the maximum current. Steady-state holds were used to ensure that the measured performance was stable and to measure the amount of performance degradation after redox cycling for intermediate utilization conditions both of which may be affected by mechanical damage to cell functional layers.

6.3.3. Redox cycling

Redox cycling tests involved blowing a low flow rate of air across the anode in order to slowly oxidize the nickel. The small air flow simulates the condition where the fuel supply is interrupted and air leaks into the anode cavity. After redox cycling the cell was rereduced at 750°C. After rereduction was complete, I-V curves and steady-state hold tests were performed in order to characterize the effect of the redox cycle on the electrochemical performance of the cell.

Redox cycles of 20 minutes (10% redox depth), 40 minutes (20% redox depth), 60 minutes (30%), 120 minutes (60%), 240 minutes (120% i.e. excess air flow) and 360 minutes (180% i.e. excess air flow) were performed during the redox tests. Redox depth calculations are found in Appendix 3-2.

6.3.4. Cool down

After all the redox cycles were completed, the cell was cooled down in a N_2 environment to preserve the microstructural changes induced by the redox test.

The entire testing procedure for the redox baseline tests is summarized in Table 6-1.

Table 6-1: Summary of the redox testing procedure

1	Heat up	20 to 800	6	0	-	400	0	0	400	-	Initial heat up in N_2
2	Initial reduction	800	4	0	-	400 to 2000	0	400 to 2000		2.5	The ratio of N_2 flow to H_2 flow is gradually decreased as the reduction proceeds until 2 SLPM of H_2 is flowing.
3	I-V curve	750	-	60	0.6	2000	0	2000	0	2.5	High fuel and air flows are used and the current is increased by 4A every 2 minutes from 0A to 60A.
4	Steady state hold	750	24	40.5	0.6	2689.2	0	565	690	2.5	A fuel utilization of 54% and air utilization of 27% was used for the tests. The current is stepped at five-second intervals, in 0.5A steps to the maximum current. After reaching 40.5A it was held at this condition for 24 hours.
5	Redox cycling	750	20 min 40 min 1 hour 2 hour 4 hour 6 hour	0	-	0	120	0	0	-	Six redox cycles are performed in a standard test - 20 min, 40 min, 1 hr, 2 hrs, 4 hrs, 6 hrs. After redox cycling the cells are reduced and I-V curves and steady state holds are performed in order to determine the amount of performance degradation.
6	Reduction	750	0.5	0	-	1000 to 2000	0	1000 to 2000		2.5	The ratio of N_2 flow to H_2 flow is gradually decreased as the reduction proceeds until 2 SLPM of H_2 is flowing. This is a much faster reduction because the cell is not entirely oxidized after the redox cycle.
7	I-V curve	750	-	60	0.6	2000	0	2000	0	2.5	Measures the amount of degradation after redox cycling.
8	Steady-state hold	750	24	40.5	0.6	2689.2	0	565	690	2.5	Measures the amount of degradation after redox cycling.
9	Redox cycling	750	20 min 40 min 1 hour 2 hour 4 hour 6 hour	0	-	0	120	0	0	-	Next redox cycle.
10	Repeat	Repeat steps 6 to 10 until all the desired redox cycles have been performed.									
11	Cool down	750 to 20	3	0	-	800	0	0	800	-	Final cool down in N_2 to preserve redox cycled microstructure.

6.4. Results and discussion

After redox cycling, current-voltage (I-V) curves and steady state holds were used in order to characterize the amount of electrochemical performance degradation that occurred. All tests were performed at 750°C.

6.4.1. I-V curves

The shape of an I-V curve will give an approximate break down of the activation, ohmic and mass transport losses that are occurring during the test. As well, this test is an important measure of the cell's performance under higher current but low utilization conditions. The I-V curve for one of the baseline redox tests (test 101278) is shown in Figure 6-3. It can be seen in the figure that the performance decreases slightly after each redox cycle, but that significant amounts of degradation do not occur until after the 2 hour redox cycle. The overall shape of the I-V curve does not significantly change after redox cycling, which suggests that redox cycling does not predominantly introduce one type of loss. It can also be seen in the figure that the current during this test does not reach the limit of mass transport losses, therefore only activation and ohmic losses are present in this test.

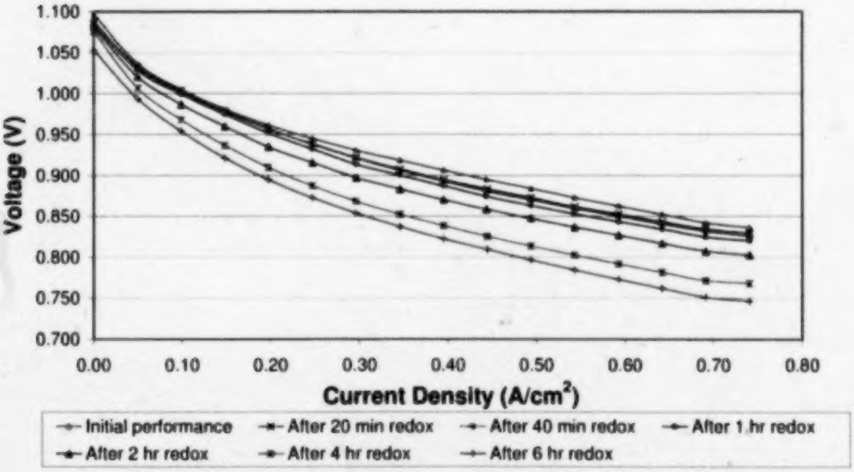

Figure 6-3: I-V curves comparing the performance before and after redox cycling.

The amount of cumulative percent voltage degradation per redox cycle for the baseline I-V curve tests is shown in Figure 6-4. It can be seen in the figure that the performance degrades only slightly until after the 2 hour redox cycle and that the biggest drop in performance occurs after the 4 hour redox cycle. This largest drop may occur at this point during the test, because it is the first redox cycle that fully oxidizes the cell. The average cumulative amount of voltage degradation after the standard redox test is 0.089 ± 0.001V or 10.9 ± 0.1%.

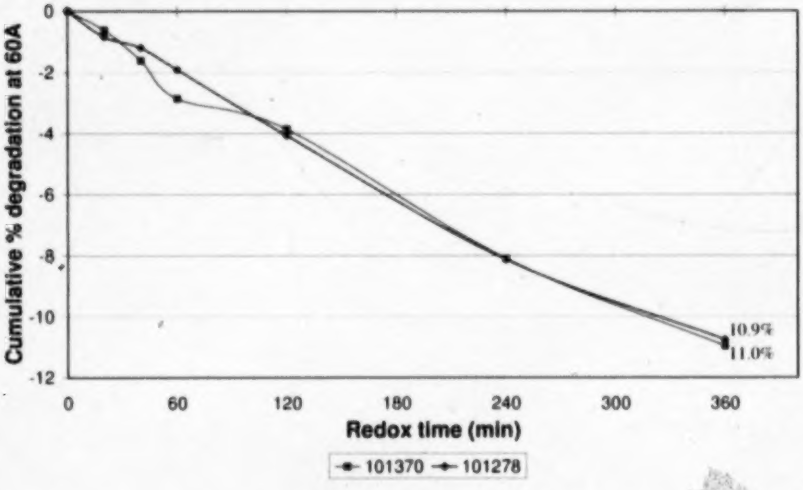

Figure 6-4: Summary of the cumulative percent degradation per redox cycle for all the baseline I-V curve tests.

After longer redox cycles (4 and 6 hours) the sample's open circuit voltage (OCV) seemed to be lower than the initial OCV. Lowered OCV values may indicate either electrolyte cracks and leaks or incomplete reduction after redox cycling. A second I-V curve test was performed after the steady-state hold in order to determine whether the OCV degradation was recoverable (incomplete reduction) or permanent (electrolyte cracks and leaks). The I-V curve measured after the 4 hour redox cycle and before the steady-state hold is compared to the I-V curve measured after the steady-state hold in Figure 6-5. The OCV measured during the second I-V curve test, after the steady state hold, was much higher

(~25 mV) than the OCV measuring during the first I-V test. The performance measured at 60 A was slightly better (2-5 mV) in some tests, the same in other tests, slightly worse (1 to 3 mV) in other tests, but OCV values always increased. This may indicate that complete rereduction has not occurred after longer redox cycles. The 60 A performance values taken before the hold were still very similar to those measured after the steady-state hold and therefore are still representative of the actual performance values. The fact that the OCV value does not decrease after redox cycling indicates that redox cycling does not damage the cell electrolyte or the seals. Therefore, any performance degradation that does occur is likely due to microstructural changes within the cell caused by redox cycles.

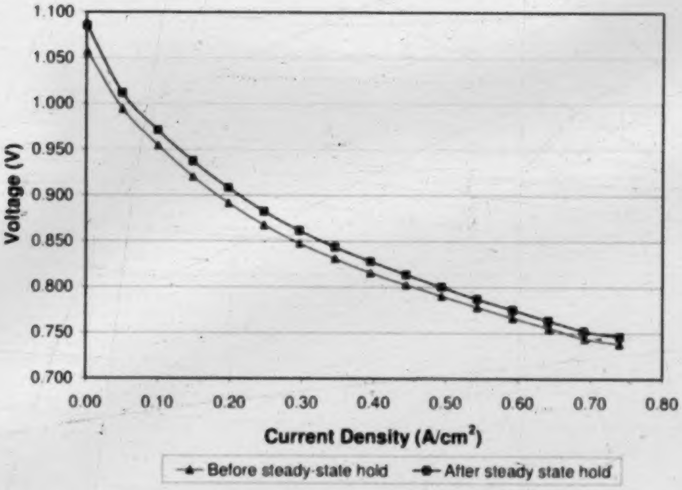

Figure 6-5: Comparison of I-V curves measured before and after steady-state holds.

For a few tests, the OCV was significantly degraded (<1.0 V) after the 6 hour redox cycle. When the cell and jig were analyzed after testing significant oxide formation on the jigs was observed. This oxidation indicates that leakage through the electrolyte and burning of the leaked fuel caused localized heating and thus increased the oxidation rate. The low OCV seen during testing and fuel leakage during post-test analysis indicates that catastrophic failure of the electrolyte caused by oxidation is possible after 6 hour redox cycles.

6.4.2. Steady-state holds

Steady-state holds were performed at lower currents and intermediate utilization conditions to ensure that the measured performance was stable and to provide another measure of the amount of performance degradation after redox cycling. The steady-state hold test for one baseline redox test is shown in Figure 6-6. The degradation behaviour of the sample is similar to the trend seen during I-V tests. The performance decreases slightly after each redox cycle, but significant amounts of degradation do not really occur until after the 2 hour redox cycle. The cell performance seems to increase at the beginning of the steady-state hold tests after the 4 and 6 hour redox cycles which supports the idea that the samples were not completely rereduced after the longer redox cycles.

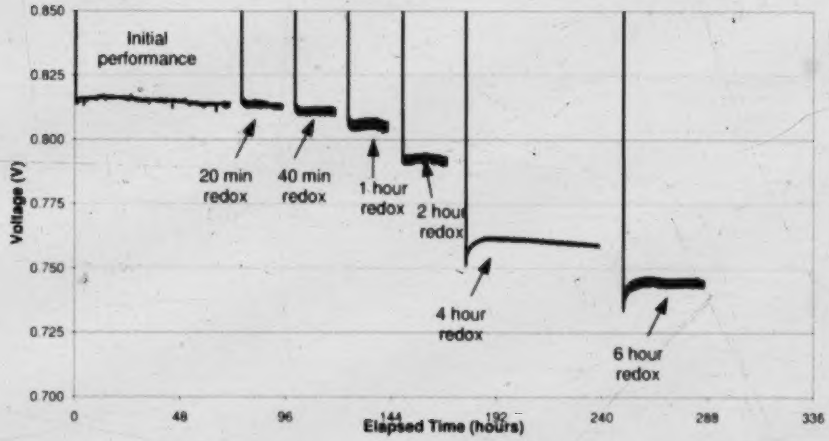

Figure 6-6: Steady-state hold comparing the performance before and after redox cycling.

The amount of cumulative voltage degradation per redox cycle for the baseline steady-state hold tests is shown in Figure 6-7. It can be seen in Figure 6-6 and Figure 6-7 that the largest performance drop occurs after the 4 hour redox cycle which is similar to the results seen during the I-V curve test. The average cumulative amount of voltage degradation after the standard redox test is 0.072 ± 0.004V or 8.9 ± 0.6%.

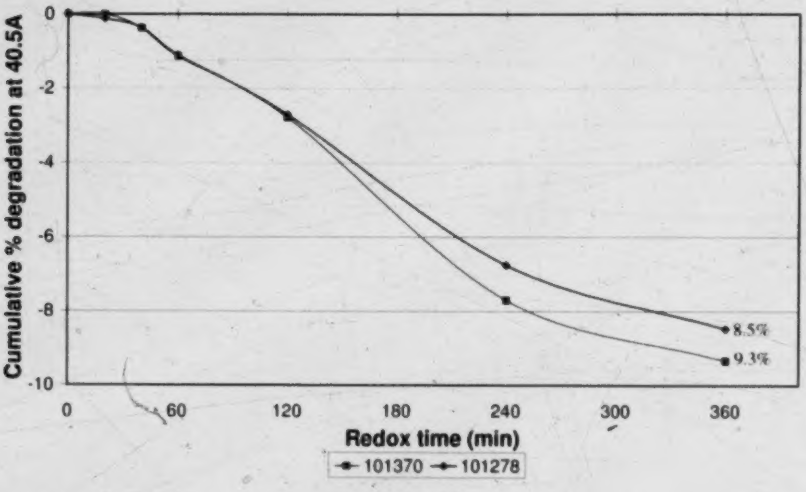

Figure 6-7: Summary of the cumulative percent degradation per redox cycle for all the baseline steady-state tests.

6.4.3. Verification of redox depth assumptions

The validity of the redox depth approach was verified using two methods: by observing the behaviour of the cell voltage during oxidation, i.e., the length of time required for the voltage to decrease to a value of 0 V and by measuring the amount of oxygen in the fuel outlet stream during oxidation, using gas chromatography.

6.4.3.1. Voltage behaviour during oxidation

Figure 6-8 shows the behaviour of the voltage during oxidation at OCV. The voltage initially rapidly decreases until it reaches a value of approximately 0.7. The voltage then decreases at a fairly constant rate until it reaches a value of 0 V after about 3.5 hours. A voltage value of 0 should indicate that the cell is mostly oxidized, i.e., there should be no electrical connection between Ni/NiO particles. This supports the redox depth calculations that show that 100% redox depth should occur after 207 minutes (3.45 hours) (see Appendix 3-2). It can be seen in Figure 6-8 that 4 and 6 hour redox cycles will result in complete oxidation of the cell during baseline redox tests.

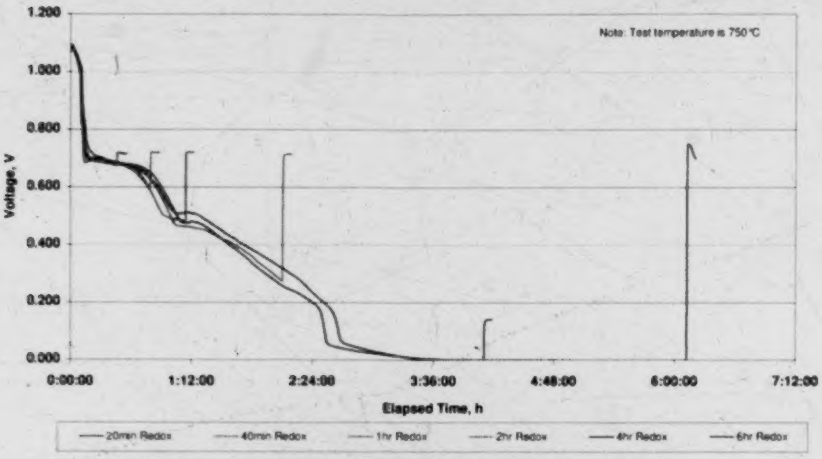

Figure 6-8: Voltage behaviour during cell oxidation.

6.4.3.2.Gas chromatography (GC) analysis

Gas chromatography (GC) analysis was performed in order to measure the amount of oxygen present in the anode outlet stream during oxidation. The testing found that during oxidation at 750°C there was no oxygen present in the anode exhaust until after approximately 2 hours of oxidation. After 2 hours an oxygen concentration of about 1% O_2 was present in the outlet stream. The amount of oxygen gradually increased until the oxygen content was about 20% after 6 hours. This indicates that the calculated time to redox depths greater than 60% will be slightly lower than the actual time since some of the oxygen is released in the outlet gas stream rather than being used up to oxidize the Ni in the cell. The time calculated for redox depths lower than 60% (120 minutes) should be accurate.

6.5.Summary

The single cell testing facilities at FCE were used to provide a baseline of the electrochemical performance degradation seen after redox cycling. Two types of electrochemical tests were performed: I-V curves and steady-state holds. I-V curve tests were used to characterize the open circuit voltage (OCV), the shape of the polarization curve and the cell performance at 60 A current with low fuel and air utilization. Steady-state hold tests examined the cell performance at 40.5 A current with 54% fuel and 27% air utilizations and looked at the longer term stability of this performance. After several redox cycles during which air was directly passed over the fuel cell anode in order to oxidize it, the cell performance was evaluated and compared to the initial performance values. The basic shape of the I-V curve and the OCV were basically unchanged after redox cycling for the majority of tests after a cumulative redox time of 780 to 850 minutes, but the 60A performance was degraded by 9.4 ± 1.6%. Slightly less cumulative degradation (7.9 ± 2.0%) after redox cycling was seen for steady-state hold tests. This baseline of cell redox degradation will be used to evaluate the performance of cells that have been modified to have enhanced redox tolerance.

6.6. References

1. E. Tang, F. Martell, R. Brulé, K. Marcotte and B. Borglum, in Proc. Solid Oxide Fuel Cells VIII (S. C. Singhal and M, Dokiya Eds.) *The Electrochemical Society Proceedings Series* (2003) 935.

2. Retrieved July 21, 2004 from the World Wide Web:http://www.fce.com/site/products/sofc/timeline2.html.

Chapter 7: Characterizing the microstructural changes induced by redox cycling with electron microscopy

Abstract

SEM and TEM were used to characterize the microstructural changes caused by redox cycling. Redox cycling significantly changed the microstructure of the cell anode substrate. Initially, as prepared (oxidized) samples had an anode substrate composed of NiO particles several microns in size, YSZ grains about 1 micron in size and intergranular porosity. Using SEM, it was observed that the anode substrate porosity increased significantly after reduction and a spongy NiO structure was formed after reoxidation. TEM analysis indicated that very fine intragranular pores formed within the Ni grains after reduction and, upon reoxidation, the very fine (<100 nm) randomly oriented NiO grains nucleated and grew. The change in the AFL microstructure was more difficult to characterize due to the very fine structure of this layer. The AFL appeared to be more porous after reduction and quite dense after reoxidation. Some microstructural damage was observed in cells after redox cycling. Vertical cracks in the electrolyte, likely caused by AFL oxidation volume expansion and damage to the AFL microstructure, were observed in some redox cycled samples.

Chapter 7: Characterizing the microstructural changes induced by redox cycling with electron microscopy

Chapter 7: Characterizing the microstructural changes induced by redox cycling with electron microscopy 7-1

List of Figures 7-3

7. Characterizing the microstructural changes induced by redox cycling with electron microscopy 7-5
- 7.1. Sample preparation 7-5
- 7.2. Scanning electron microscopy (SEM) 7-5
  - 7.2.1. Equipment 7-5
  - 7.2.2. Microscopy techniques 7-5
  - 7.2.3. Sample preparation 7-7
- 7.3. Transmission electron microscopy (TEM) and scanning transmission electron microscopy (STEM) 7-7
  - 7.3.1. Equipment 7-7
  - 7.3.2. Microscopy techniques 7-7
  - 7.3.3. Sample preparation 7-8
- 7.4. Redox treatment of anode substrate samples 7-10
- 7.5. Redox treatment of fuel cell samples 7-10
- 7.6. Results and discussion – Anode substrate samples 7-11
  - 7.6.1. As prepared microstructure 7-11
  - 7.6.2. Reduced microstructure 7-13
  - 7.6.3. Reoxidized microstructure 7-18
  - 7.6.4. Rereduced microstructure 7-20
- 7.7. Results and discussion – Fuel cell samples 7-22
  - 7.7.1. As prepared microstructure 7-22
  - 7.7.2. Reduced microstructure 7-22
  - 7.7.3. Reoxidized microstructure 7-23
  - 7.7.4. Rereduced microstructure 7-24
  - 7.7.5. STEM of fuel cell samples 7-24
  - 7.7.6. Visual examination of fuel cell samples 7-26
  - 7.7.7. Damage caused by redox cycling 7-29
- 7.8. Summary of redox microstructural changes 7-30
  - 7.8.1. Anode substrate samples 7-30
  - 7.8.2. Fuel cell samples 7-32
- 7.9. Bibliography 7-34
- 7.10. References 7-34

List of Figures

Figure 7-1: Schematic of the TEM sample preparation process. 7-9
Figure 7-2: Optical micrograph of a TEM specimen. 7-10
Figure 7-3: BSE SEM image of a fresh fractured, as prepared sample. 7-11
Figure 7-4: Higher magnification BSE SEM image of an as prepared sample. 7-11
Figure 7-5: BSE SEM image of a polished, as prepared (oxidized) sample 7-11
Figure 7-6: BF TEM image of an as prepared sample. 7-12
Figure 7-7: EDX spectrum of a NiO grain in an as prepared sample. 7-12
Figure 7-8: EDX spectrum of an YSZ grain in an as prepared sample. 7-12
Figure 7-9: BSE SEM image of a fresh fractured, partially reduced sample. 7-13
Figure 7-10: EDX spectrum of NiO grain shown in Figure 7-9. 7-13
Figure 7-11: EDX spectrum of Ni rim indicated in Figure 7-9. 7-13
Figure 7-12: BSE SEM image of a fresh fractured, fully reduced sample. 7-14
Figure 7-13: Higher magnification SEM image of a fully reduced sample. 7-14
Figure 7-14: BSE SEM image of a polished, reduced sample. 7-14
Figure 7-15: HAADF STEM image of a reduced sample (inverted contrast). 7-16
Figure 7-16: BF TEM image of a reduced sample. 7-16
Figure 7-17: Schematic diagram of electron beam diffraction. 7-17
Figure 7-18: Schematic diagram of multiple diffraction in Ni/NiO/Ni layers. 7-18
Figure 7-19: BSE SEM image of a reoxidized sample. 7-18
Figure 7-20: Higher magnification BSE SEM image of a reoxidized sample. 7-18
Figure 7-21: BSE SEM image of a polished, reoxidized sample. 7-19
Figure 7-22: BSE SEM image of a polished, partially reoxidized sample with EDX spectra from site 14.2 and site 14.3 in the figure. 7-19
Figure 7-23: HAADF STEM image of a reoxidized sample 7-20
Figure 7-24: BF TEM image of a reoxidized sample. 7-20
Figure 7-25: HAADF STEM image of a rereduced sample 7-21
Figure 7-26: BF TEM image of a rereduced sample. 7-21
Figure 7-27: HAADF STEM image (inverted contrast) of rereduced sample. 7-22
Figure 7-28: SEM BSE image of an as prepared anode-supported SOFC. 7-22
Figure 7-29: SEM BSE image of a reduced anode-supported SOFC. 7-23
Figure 7-30: SEM BSE image of a polished reduced anode-supported SOFC. 7-23
Figure 7-31: SEM BSE image of a reoxidized anode-supported SOFC. 7-23
Figure 7-32: SEM image of a polished, reoxidized anode-supported SOFC. 7-23
Figure 7-33: Higher magnification SEM BSE image of a reoxidized anode-supported SOFC. 7-24
Figure 7-34: SEM BSE image of a rereduced anode-supported SOFC. 7-24
Figure 7-35: SEM image of a polished, rereduced anode-supported SOFC 7-24
Figure 7-36: HAADF STEM image of an oxidized fuel cell sample showing the AFL-electrolyte interface. 7-25
Figure 7-37: HAADF STEM image of an oxidized fuel cell sample showing the AFL-anode substrate interface. 7-25
Figure 7-38: Higher magnification HAADF STEM image of an oxidized fuel cell sample showing the AFL-electrolyte interface. 7-26
Figure 7-39: EDX spectrum from point 1 in Figure 7-38. 7-26

Figure 7-40: EDX spectrum from point 2 in Figure 7-38. 7-26
Figure 7-41: Image of the anode side of an as prepared cell. 7-27
Figure 7-42: Image of the anode side of a reduced cell after testing. 7-27
Figure 7-43: Image of anode side of a partially reoxidized redox cycled cell.. 7-27
Figure 7-44: Image of the anode side of a fully reoxidized redox cycled cell.. 7-27
Figure 7-45: Cross-sectional view of a partially reoxidized cell. 7-29
Figure 7-46: SEM image of an anode-supported SOFC after redox cycling.... 7-29
Figure 7-47: SEM image of an anode-supported SOFC after redox cycling. 7-29
Figure 7-48: SEM image of an anode-supported SOFC after redox cycling. 7-30
Figure 7-49: Higher magnification SEM image of Figure 7-48. 7-30
Figure 7-50: SEM BSE image of a fresh fractured as prepared sample. 7-31
Figure 7-51: SEM BSE image of a fresh fractured reduced sample. 7-31
Figure 7-52: SEM BSE image of a fresh fractured reoxidized sample............ 7-31
Figure 7-53: SEM BSE image of the reoxidized sample in Figure 7-52 at higher magnification. 7-31
Figure 7-54: BF TEM image of an as prepared sample. 7-32
Figure 7-55: BF TEM image of a reduced sample. 7-32
Figure 7-56: BF TEM image of a reoxidized sample. 7-32
Figure 7-57: BF TEM image of a rereduced sample. 7-32
Figure 7-58: SEM BSE image of an as prepared anode-supported SOFC. 7-33
Figure 7-59: SEM BSE image of a reduced anode-supported SOFC. 7-33
Figure 7-60: SEM BSE image of a reoxidized anode-supported SOFC........... 7-33
Figure 7-61: SEM BSE image of a rereduced anode-supported SOFC........... 7-33

7. Characterizing the microstructural changes induced by redox cycling with electron microscopy

The microstructure of anode supported SOFCs produced by FuelCell Energy's (FCE) standard TSC-2 cell fabrication process was characterized using scanning and transmission electron microscopy. Initially the study looked at the effect of redox cycles on single layer samples with a microstructure similar to an anode substrate. Since the anode substrate is by far the thickest layer in an anode supported SOFC it may have a significant effect on the overall redox tolerance of the cell. The second study looked at the microstructural changes of actual fuel cells after multiple redox cycles in a single cell test stand. For both types of samples the general microstructure of the as prepared (oxidized) cells was first examined. This microstructure formed the baseline for comparison with the microstructure seen after reduction, reoxidation and rereduction.

7.1. Sample preparation

Anode substrate samples were fabricated from a single layer tape cast sheet. The method used to produce the samples was identical to the anode substrate fabrication process used for fuel cell samples. Fuel cell samples were prepared using FCE's standard TSC-2 cell fabrication process as detailed in Section 6.1.

7.2. Scanning electron microscopy (SEM)

7.2.1. Equipment

Scanning electron microscopy was used to characterize the microstructural changes that occurred after redox cycling. All SEM images were taken using a LEO 1450 variable pressure SEM operating at 15kV with an Oxford Instruments ultra thin window (UTW) energy-dispersive x-ray (EDX) spectrometer.

7.2.2. Microscopy techniques

Scanning electron microscopy (SEM) uses an electron beam that is scanned across the surface of the sample. The resulting image is built up from the signal derived from each scanned area. These signals are formed from electrons that are elastically or inelastically scattered by the sample one or more times. The scattered electrons emerge from the top surface of the sample and are collected by one of several different types of detectors.

The main SEM imaging technique used during this study was back-scattered electron (BSE) imaging. BSE are electrons from the primary beam that are elastically scattered back to escape from the sample surface. Typically, BSE are the result of multiple elastic scattering events each of which alters the electron path a small amount. The cumulative effect of all of these events alters the path enough to allow the electrons to reflect back from the incident surface of the sample. BSE are a very important imaging signal in the SEM because they are sensitive to both sample composition and topography. In order to separate these signals a polished sample is often used to reduce the effect of topography. A BSE image of a polished sample with minimal topographic effects will be brighter in areas composed of atoms with a higher atomic number and less intense in areas where lower atomic number species are present.

Energy dispersive x-ray analysis (EDX) was another important microscopy technique used in this study. EDX uses the characteristic x-rays produced by inelastic scattering of the electron beam within the sample to identify the elements that are present. Characteristic x-rays are produced when the electron beam interacts with an inner shell electron of an atom within the sample. The inner shell electron is ejected, which leaves the atom in an excited state with a vacancy in the inner electron shell. The atom then relaxes to its ground state by allowing an electron from the outer electron shell to fill the inner shell vacancy. The amount of energy produced as the atom relaxes can be released in two ways: another outer shell electron can be ejected to produce an Auger electron, or the energy can be released as a photon of electromagnetic radiation called a characteristic x-ray. This characteristic x-ray will have a very specific energy, which is characteristic of the atomic species and electron shell that produced it and which therefore can be used to identify the element present.

7.2.3. Sample preparation

All samples examined in the SEM were cross-sections that were prepared as fresh fractures by breaking the cell into pieces. Some samples were examined as fresh fractures after a thin gold coating was applied to minimize charging effects. Other fracture samples were mounted in epoxy and polished with SiC paper, diamond paste and an Al_2O_3 suspension in order to provide a flat, easy to image surface.

7.3. Transmission electron microscopy (TEM) and scanning transmission electron microscopy (STEM)

7.3.1. Equipment

TEM images were obtained using a JEOL-2010 TEM with a Noran UTW EDX spectrometer or a Tecnai F20 field emission gun (FEG) TEM/STEM with an EDAX Phoenix UTW EDX spectrometer.

7.3.2. Microscopy techniques

Two significantly different imaging modes were used for imaging - TEM mode and STEM mode - although both modes use a sample that is thin enough to be transparent to electrons. In TEM mode a fixed electron beam passes through the sample and either the unscattered electrons or a portion of the scattered electrons that emerge from the sample are selected and projected onto a screen. In STEM mode the electron beam is scanned across the sample and an image is built up from each of the scanned areas in the exact same method used in SEM. The major difference between SEM and STEM is that STEM typically uses signals that pass through to emerge from the bottom of the sample, whereas SEM typically uses signals that reflect and emerge from the incident sample surface.

In TEM mode, bright-field (BF) imaging methods were used. BF images are formed by selecting the direct beam, i.e., the beam that passes directly through the sample with no or minimal scattering. The selected beam is then projected onto a phosphor screen. In a BF image, areas that are thicker or that have higher atomic number will be less intense while areas that are thinner or are composed of lower atomic number species will be brighter.

In STEM mode, a high angle annular dark field (HAADF) detector was used to form images. This detector has a large hole in the middle and is centered around the optic axis of the beam. It collects electrons that are scattered at relatively high angles and produces an image with approximately inverted contrast when compared to TEM bright field images.

EDX and electron diffraction were used to identify the elements present in the samples. EDX in a TEM uses the same principles as in an SEM but has a better resolution due to the smaller interaction volume for an electron transparent TEM specimen. Electron diffraction occurs when the crystallographic planes within a sample diffract the electron beam, which produces a diffraction pattern. The spacing of the spots or rings in the pattern will correspond to the spacing of the crystallographic planes of the component (or components) present in the selected area. Since these spacings will be unique for each phase they can be used to identify the phases present in the sample. Two methods to form electron diffraction patterns were used in this study: selected area diffraction (SAD) and convergent beam electron diffraction (CBED). The SAD technique uses an aperture to select a specific area of the image to form the diffraction pattern. The pattern forms a series of sharply defined spots (for single crystalline areas) or rings (for polycrystalline areas). SAD is typically limited to areas larger than about 0.5 microns in size. CBED techniques use a converging electron beam to form the diffraction pattern and therefore can analyze much smaller areas; however, the converging beam means that disks are formed in the pattern rather than discrete spots.

7.3.3. Sample preparation

Both planar and cross-sectional TEM samples were prepared. Cross-sectional samples were prepared by gluing together sectioned pieces using epoxy. After gluing, both sample types were prepared in a similar fashion. The basic TEM sample preparation method used mechanical polishing, dimpling and sputtering techniques. A 3 mm diameter disk was cut from a sample using an ultrasonic cutter. The disk was then ground and polished to a thickness of less than 200 microns using 320 and 600 grit silicon carbide paper. After polishing, the disk was dimpled to a central thickness of less than 20 μm using a bronze wheel and diamond paste. In a dimpler, a rotating wheel was used to grind a dimple-like depression on each side of the sample. This resulted in a sample with a thick outer edge for mechanical support and a thin central area. After dimpling, an ion mill was used to sputter away the mechanical damage induced by polishing/dimpling and to further thin the sample to perforation. Argon ions accelerated at 5-6 keV, impinging at 15° to the sample surface, were utilized for sputtering. The thin area around the hole was 100-200 nm in thickness and thus electron transparent. A diagram showing the sample preparation process is given in Figure 7-1. An optical micrograph of a typical TEM specimen is shown in Figure 7-2.

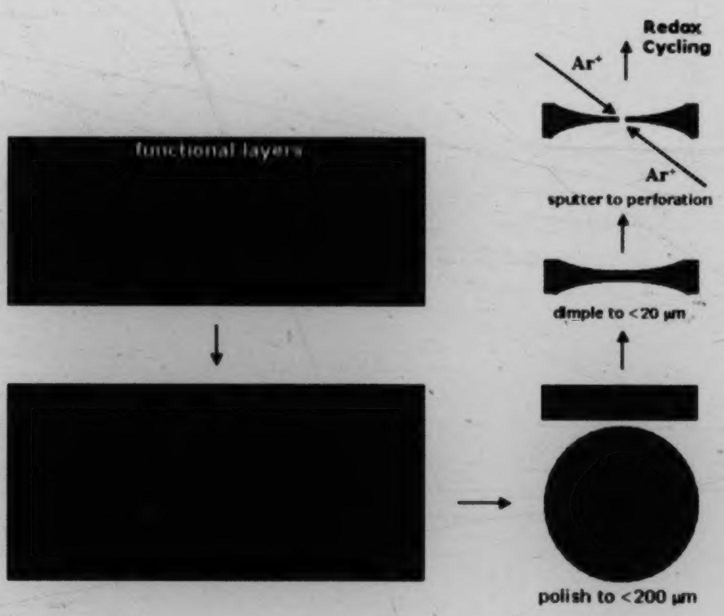

Figure 7-1: Schematic of the TEM sample preparation process.

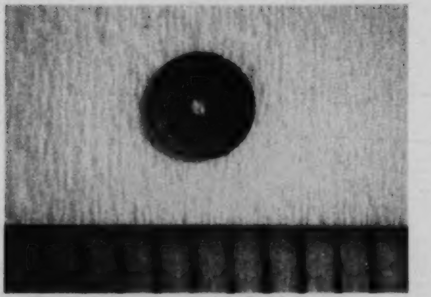

Figure 7-2: Optical micrograph of a TEM specimen. Graduations are 1 mm apart.

7.4. Redox treatment of anode substrate samples

After the TEM samples were prepared, they were reduced in 5% hydrogen (95% argon or nitrogen) and oxidized in air at a temperature of 700°C for varying amounts of time to simulate redox cycling conditions. Two treatment conditions were desired: full reduction/oxidation and partial reduction/oxidation. After redox treatment, the samples were carbon coated using a carbon evaporator in order to provide sufficient electrical conductivity for TEM imaging.

7.5. Redox treatment of fuel cell samples

Fuel cell samples were redox cycled in single cell test stands at 750°C. Standard cells were oxidized by flowing air through the anode chamber for 20, 40, 60, 120, 240 and 360 minutes. Between each oxidation, the cell was reduced over a period of 4 hours in hydrogen and the performance was measured electrochemically. Chapter 6 gives more detail about the baseline redox single cell tests. After all the redox cycles were completed, the cells were either cooled to room temperature in a reduced state or were reoxidized for a period of time and then cooled in nitrogen to preserve the reoxidized microstructure. The samples were removed from the single cell test jigs, were visually examined and then were sectioned to prepare either SEM or TEM samples.

7.6. Results and discussion – Anode substrate samples

7.6.1. As prepared microstructure

Figure 7-3 shows a back-scattered electron (BSE) SEM image of a fresh fractured, as prepared (oxidized) microstructure and Figure 7-4 shows the same area at higher magnification. The YSZ phase is light in colour, with a grain size around 1µm, while the NiO grains appear grey and are several microns in size. Figure 7-5 is a polished as prepared sample. In the figure, the grey NiO component is readily distinguished from the white YSZ phase and the black pores.

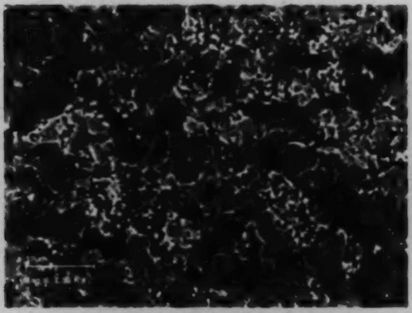

Figure 7-3: BSE SEM image of a fresh fractured, as prepared (oxidized) sample.

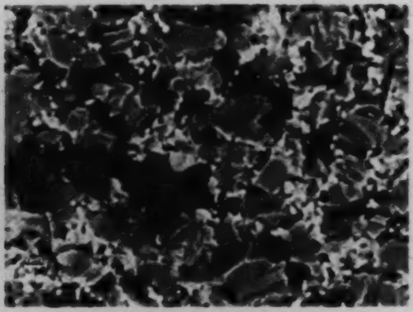

Figure 7-4: Higher magnification BSE SEM image of a fresh fractured, as prepared (oxidized) sample.

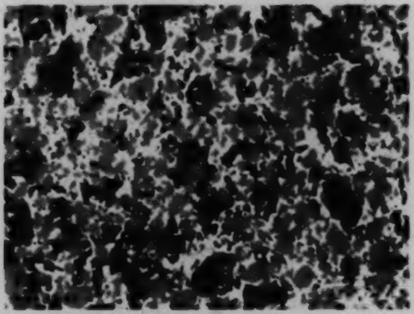

Figure 7-5: BSE SEM image of a polished, as prepared (oxidized) sample.

Figure 7-6 is a bright field (BF) TEM image of an as prepared sample and provides confirmation of the SEM results. The pores and holes in a BF image appear white. Selected area electron diffraction (SAD) (insets in Figure 7-6) and energy dispersive x-ray analysis (EDX) techniques (Figure 7-7 and Figure 7-8) were used to confirm the phases present, i.e., NiO and YSZ. The Si and Fe peaks in Figure 7-7 are artifacts from TEM sample preparation.

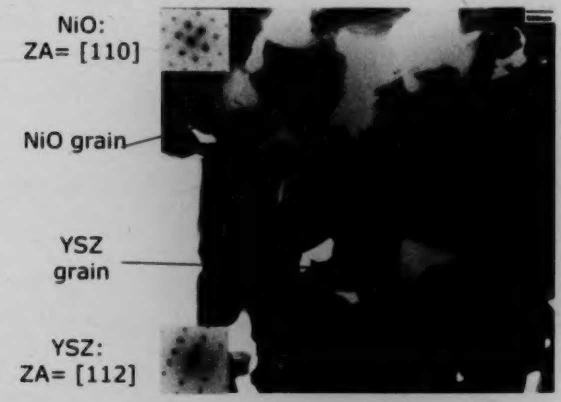

Figure 7-6: BF TEM image of an as prepared sample.

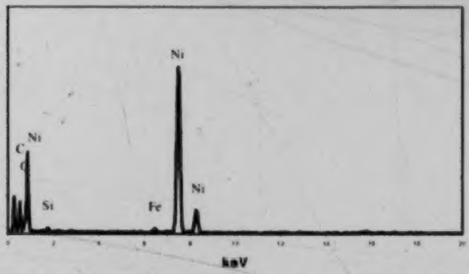

Figure 7-7: EDX spectrum of a NiO grain in an as prepared sample.

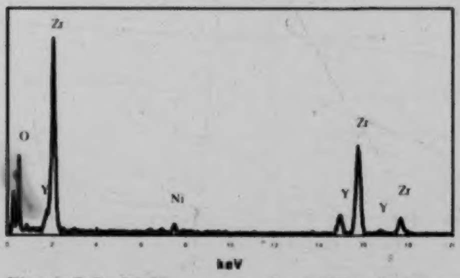

Figure 7-8: EDX spectrum of an YSZ grain in an as prepared sample.

7.6.2. Reduced microstructure

Figure 7-9 is a BSE SEM image of a partially reduced fresh fractured anode. The sample was heated to 950°C in 5% H_2 (95% Ar) for a period of six hours. A thin, lighter coloured rim of nickel can clearly be seen around the NiO grains. This identification was confirmed by EDX analysis as shown in Figure 7-10 and Figure 7-11. Gold peaks in the EDX spectra are due to a thin gold layer deposited on the sample to enhance electrical conductivity.

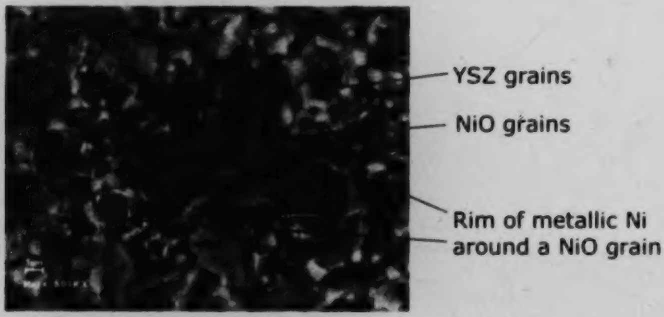

Figure 7-9: BSE SEM image of a fresh fractured, partially reduced sample.

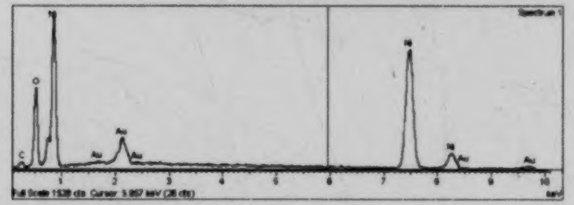

Figure 7-10: EDX spectrum of NiO grain shown in Figure 7-9.

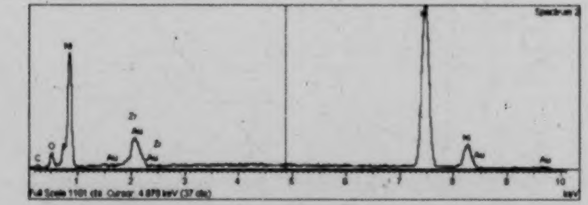

Figure 7-11: EDX spectrum of Ni rim indicated in Figure 7-9. The weak O peak arises from the adjacent NiO grain.

Figure 7-12 and Figure 7-13 are BSE SEM images of a fully reduced, fresh fractured anode at two different magnifications. Figure 7-13 shows the individual Ni grains, which are several microns in size, in a larger Ni particle and the small YSZ grains, which are completely unaffected by the entire reduction process. It is apparent from the images that the amount of porosity has increased after reduction. Figure 7-14 shows a polished reduced sample. It is more difficult to differentiate between the two phases in the reduced sample than in oxidized sample. In the figure, the Ni component is light grey in colour while the YSZ is white. The polished reduced sample looks like it has less porosity than the as prepared sample; however, this is likely an artefact due to Ni smearing during the polishing process.

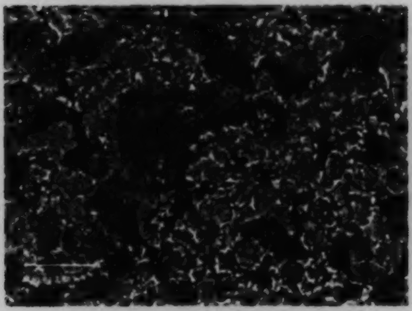

Figure 7-12: BSE SEM image of a fresh fractured, fully reduced sample.

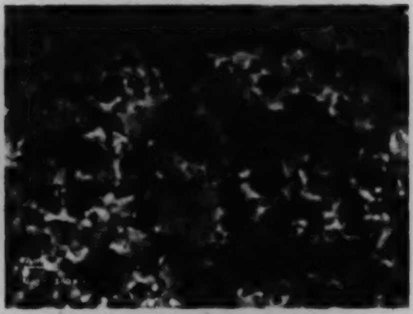

Figure 7-13: Higher magnification BSE SEM image of a fresh fractured, fully reduced sample.

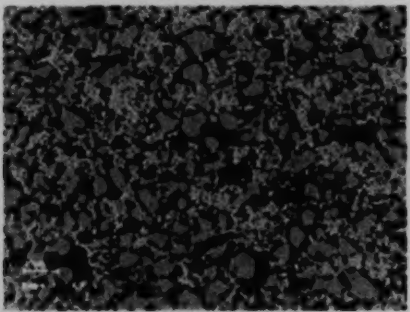

Figure 7-14: BSE SEM image of a polished, reduced sample.

Characterizing the microstructural changes induced by redox cycling with electron microscopy

Figure 7-15 is a high angle annular dark field (HAADF) STEM image, with inverted contrast to resemble a bright field image, of a partially reduced NiO/YSZ anode. This image clearly shows the distribution of reduced Ni and unaffected YSZ within the sample. The sample had been heated to 700°C in 5% H_2 for five minutes. Figure 7-16 is a BF TEM micrograph of the same sample at higher magnification. The image shows the presence of small (50 nm) intragranular pores within the larger Ni grain. The grain, which is several microns in size, is single crystalline, as illustrated by the SAD pattern in the inset. The intragranular porosity likely helps to accommodate the large volume change (~40%) associated with NiO reduction to Ni without overstressing the YSZ particles, which are unaffected by the reduction process.

The diffraction pattern of the partially reduced sample (inset of Figure 7-16) contains satellite spots, which indicate that multiple diffraction is occurring. The more intense spots in the diffraction pattern correspond to nickel while the satellite spots correspond to both Ni and NiO reflections. The presence of satellite spots indicates that the grain is only partially reduced and that Ni is growing epitaxially on the parent NiO grain. Diffraction patterns of several orientations from various grains were obtained and all patterns contained satellite spots. When the sample is fully reduced the satellite spots disappear, leaving only a single Ni pattern.

Epitaxial growth of Ni on the NiO grains is somewhat unexpected due to the large mismatch (15.6%) in lattice parameters between Ni and NiO, [1] but not unheard of, as Kuhlenbeck and Freund have reported epitaxial growth of NiO on Ni substrates for ultrathin films. [2]

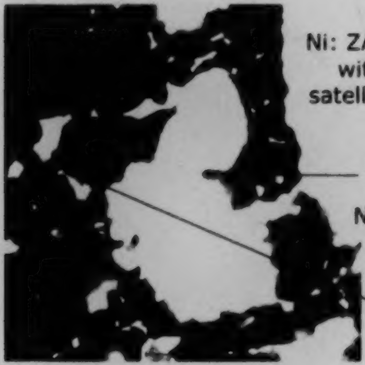

Figure 7-15: HAADF STEM image of a reduced sample (inverted contrast).

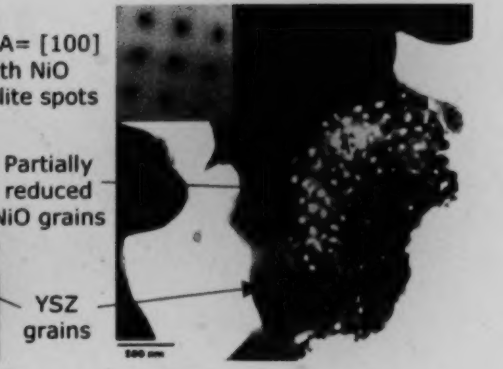
Ni: ZA= [100] with NiO satellite spots
Partially reduced NiO grains
YSZ grains
100 nm

Figure 7-16: BF TEM image of a reduced sample.

Figure 7-17 and Figure 7-18 are schematic diagrams to explain the concept of multiple diffraction. In a partially reduced sample, the outer part of the sample will be Ni with an inner core of NiO. The Ni spots in the diffraction pattern are more intense than the NiO spots, which indicates that the Ni layers are thicker than the NiO layer, i.e., the sample is almost fully reduced.

As the electron beam passes through the specimen it can be diffracted multiple times when it passes through each Ni and NiO layer. This results in a number of large primary spots and satellite spots clustered around the primary spots, as shown in Figure 7-18a. The red beam in Figure 7-17 is the incident (undiffracted) electron beam, a significant portion of which passes directly through the sample. The blue beam in Figure 7-17 occurs when the upper or lower Ni layers diffract part of the red incident beam. This diffraction results in the intense primary spots on the diffraction pattern as shown in Figure 7-18b. The yellow spots occur when the incident beam is diffracted as it passes through the NiO layer. The fact that these spots are in the same orientation as the primary blue spots provides evidence that Ni is growing epitaxially on NiO. The yellow NiO spots are shown in Figure 7-18c. Other layers within the sample can rediffract the diffracted beams as shown by the green and purple beams. The green spots on the pattern occur when the yellow beam, initially diffracted by the NiO layer, is diffracted again by the lower Ni layer. This results in a Ni pattern shifted as shown in Figure 7-18d. The green and blue patterns have the same spacing, which indicates that they both arise from Ni layer diffraction. The shifting that occurs for the green pattern indicates that this pattern arises from a previously diffracted beam, which is rediffracting, rather than from the incident beam. The purple spots on the diffraction pattern occur when the NiO layer rediffracts the blue beam, initially diffracted by the upper Ni layer. This results in shifted NiO spots on the diffraction pattern as shown in Figure 7-18e. The purple and yellow patterns have the same spacing, which indicates that they both arise from NiO diffraction. The shift observed for the purple pattern indicates that this pattern arises from a previously diffracted Ni beam rediffracting, rather than the incident beam. Rediffraction can occur multiple times and in multiple orientations resulting in the many satellite spots seen in Figure 7-18f. Even more satellite spots are possible.

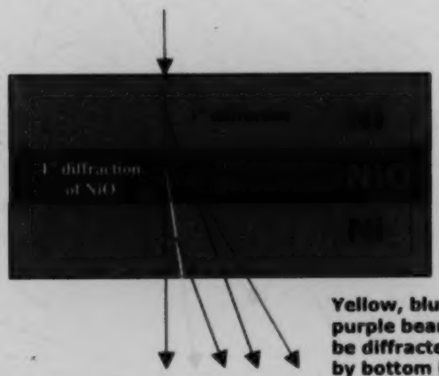

Yellow, blue and purple beams can be diffracted again by bottom Ni layer

Figure 7-17: Schematic diagram of electron beam diffraction.

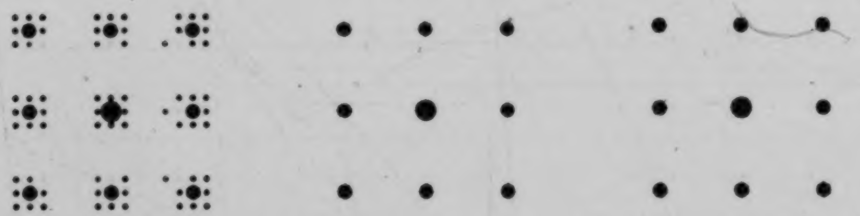

(a) (b) (c)

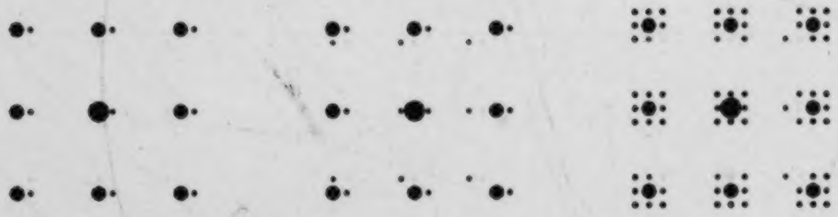

(d) (e) (f)

Figure 7-18: Schematic diagram of multiple diffraction in the Ni/NiO/Ni layers. Each diagram is explained in the text.

7.6.3. Reoxidized microstructure

Figure 7-19 and Figure 7-20 are BSE SEM images of fully reoxidized, fresh fracture anode samples. After reoxidation the NiO grains appear spongy with much smaller pores than the as prepared, oxidized samples before redox cycling. Figure 7-21 shows a polished, reoxidized anode sample. In the image, NiO areas are grey while YSZ areas are white. Figure 7-22 shows a polished, partially reoxidized anode sample with EDX spectra. The EDX spectra confirm the presence of both Ni and NiO. In the figure the darker grey areas are NiO, the lighter grey areas are Ni and the white areas are YSZ.

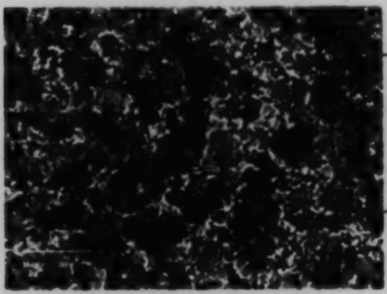

Figure 7-19: BSE SEM image of a reoxidized sample.

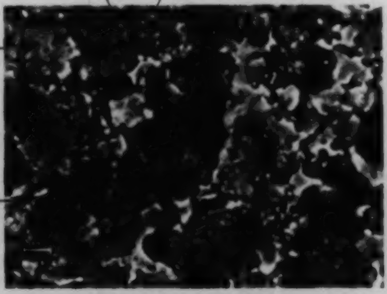

Figure 7-20: Higher magnification BSE SEM image of a reoxidized sample.

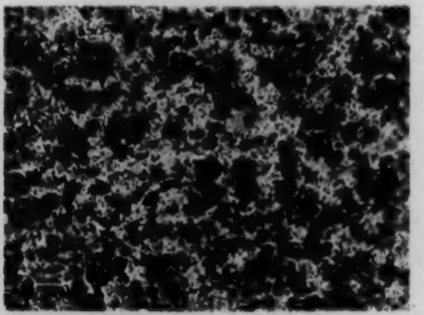

Figure 7-21: BSE SEM image of a polished, reoxidized sample.

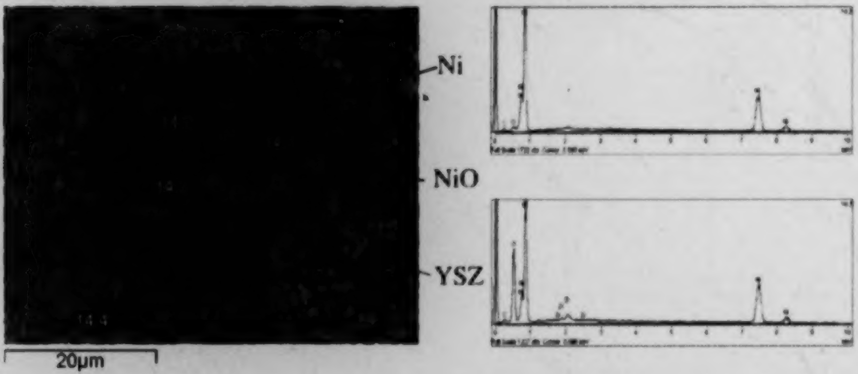

Figure 7-22: BSE SEM image of a polished, partially reoxidized sample with EDX spectra from site 14.2 and site 14.3 in the figure.

TEM images (Figure 7-23 and Figure 7-24) of reoxidized samples show an interesting result – the formation of very fine grains of NiO less than 100 nm in size. The YSZ grains appear to be unaffected by the reduction and reoxidation process. These samples were fully reduced for a period of five hours at 700°C and then reoxidized for 15 minutes at 700°C

The presence of the fine NiO grains was confirmed by the appearance of the polycrystalline ring diffraction pattern seen in the inset of Figure 7-24. The pattern shows little orientation effects, indicating that preferred growth of NiO grains on the Ni does not occur. This sample was completely reoxidized as no additional Ni rings were observed in the diffraction pattern.

The grain refinement that occurs upon reoxidation may be due to the large number of intragranular pores that occur after reduction. These pores provide many nucleation sites for the NiO grains to form and thus promote the formation of small randomly oriented grains.

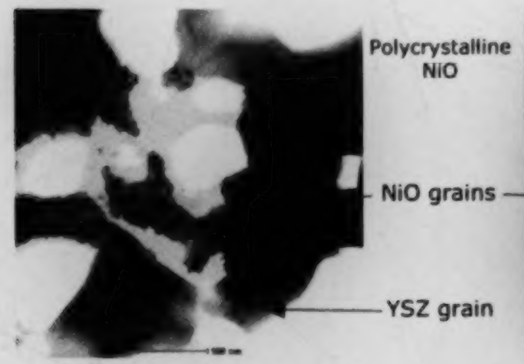

Figure 7-23: HAADF STEM image of a reoxidized sample (inverted contrast).

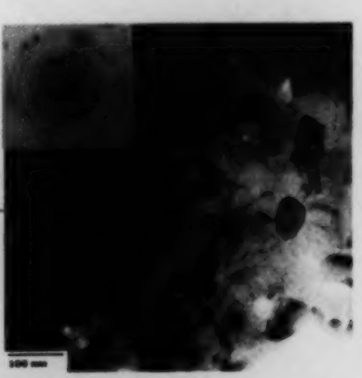

Figure 7-24: BF TEM image of a reoxidized sample.

7.6.4. Rereduced microstructure

After rereduction the overall Ni grain size remains small (<200 nm) as can be seen in Figure 7-25 and Figure 7-26. The presence of fine Ni grains was confirmed by the polycrystalline ring diffraction patterns seen in the inset of Figure 7-26. No preferred orientation was evident. The sample was completely reduced as no additional NiO rings were observed in the diffraction pattern. These samples were fully reduced for a period of 5 hours, fully reoxidized for a period of 8 hours and then rereduced for 1 hour. All treatments were performed at 700°C.

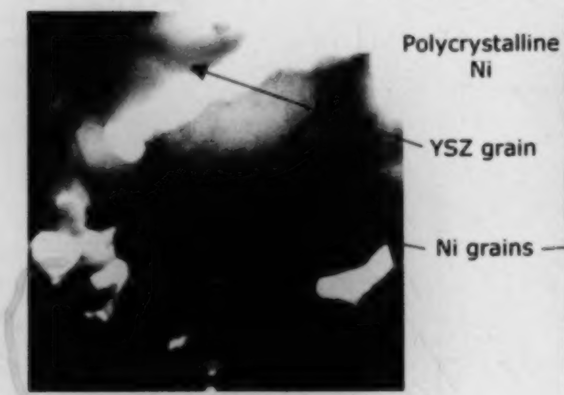

Figure 7-25: HAADF STEM image of a rereduced sample (inverted contrast).

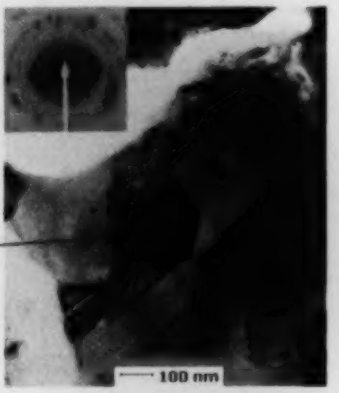

Figure 7-26: BF TEM image of a rereduced sample.

Figure 7-27 shows a HAADF STEM image of a rereduced sample and convergent beam electron diffraction (CBED) patterns from individual grains. CBED allows diffraction patterns of very small areas to be formed. In this case, CBED patterns of adjoining grains were taken without additional tilting in order to study the orientation relationships between five adjoining grains. Grains 1 and 2 have almost identical patterns and are very close to a [103] zone axis. Grains 3, 4, and 5 do not form recognizable patterns, which indicates that they are far from a zone axis and thus have significantly different orientations than grains 1 and 2 and from each other. These five grains, and the surrounding ones, originate from the same large initial NiO grain. After reoxidation and rereduction, though, any orientation relationships are lost.

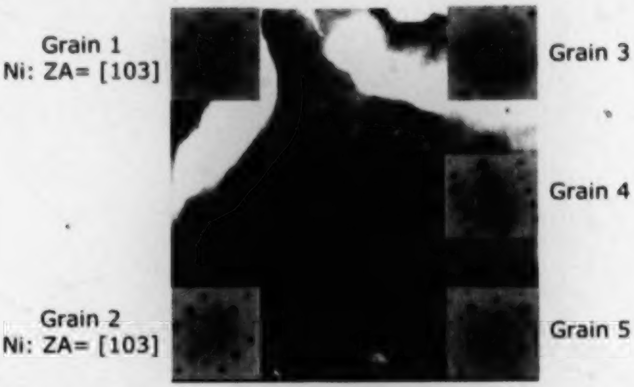

Figure 7-27: HAADF STEM image (inverted contrast) of rereduced sample with embedded CBED patterns.

7.7. Results and discussion – Fuel cell samples

7.7.1. As prepared microstructure

A BSE image of a fresh fractured, as prepared fuel cell sample is shown in Figure 7-28. In the figure, the AFL and anode substrate microstructure are fully oxidized and not very porous.

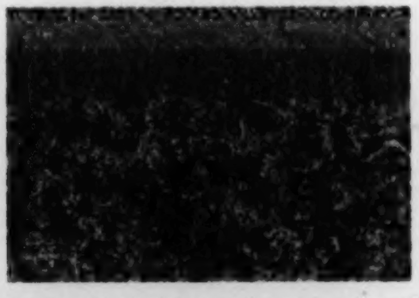

Figure 7-28: SEM BSE image of a fresh fractured, as prepared (oxidized) anode-supported SOFC.

7.7.2. Reduced microstructure

The microstructure of a reduced full cell sample is shown in Figure 7-29 and Figure 7-30. Figure 7-29 is a fresh fractured sample while Figure 7-30 is a polished sample. It is apparent in the figures that the amount of porosity in both the anode and AFL is increased after reduction.

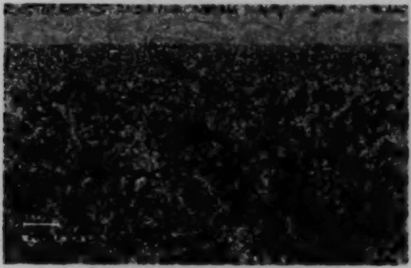

Figure 7-29: SEM BSE image of a fresh fractured, reduced anode-supported SOFC.

Figure 7-30: SEM BSE image of a polished, reduced anode-supported SOFC.

7.7.3. Reoxidized microstructure

Reoxidized fuel cell samples are shown in Figure 7-31 and Figure 7-32. In the polished sample (Figure 7-32), it is easy to see the reoxidized areas in the anode substrate and the dense, oxidized AFL. Figure 7-33 shows a higher magnification image of a fresh fractured reoxidized sample. The spongy structure typical of reoxidized samples can be seen in the figure.

Figure 7-31: SEM BSE image of a fresh fractured, reoxidized anode-supported SOFC.

Figure 7-32: SEM BSE image of a polished, reoxidized anode-supported SOFC.

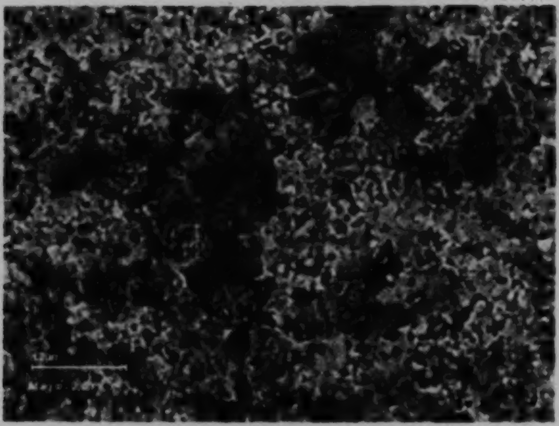

Figure 7-33: Higher magnification SEM BSE image of a fresh fractured, reoxidized anode-supported SOFC showing spongy NiO structure.

7.7.4. Rereduced microstructure

Figure 7-34 and Figure 7-35 illustrate the microstructure of the fuel cell samples after rereduction. The microstructure is more porous in rereduced samples than in as prepared or reoxidized samples, but looks very similar to that for reduced samples.

Figure 7-34: SEM BSE image of a fresh fractured, rereduced anode-supported SOFC.

Figure 7-35: SEM BSE image of a polished, rereduced anode-supported SOFC.

7.7.5. STEM of fuel cell samples

STEM images were taken of fuel cell samples in order to provide a microstructural baseline. Figure 7-36 and Figure 7-37 show the anode functional layer – electrolyte and the anode functional layer – anode substrate interfaces respectively for an oxidized sample. The figures show the large difference in microstructure and porosity between the three layers. There is virtually no porosity in the electrolyte, only small, well distributed pores. NiO and YSZ grains are visible in the anode functional layer, with larger pores and coarser NiO particles in the anode substrate. Note that the horizontal crack in the electrolyte in Figure 7-36 was likely introduced during STEM sample preparation not during cell fabrication or redox testing.

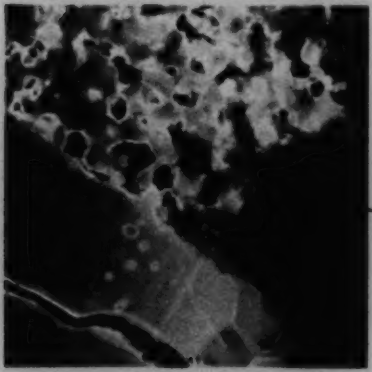

Figure 7-36: HAADF STEM image of an oxidized fuel cell sample showing the AFL-electrolyte interface.

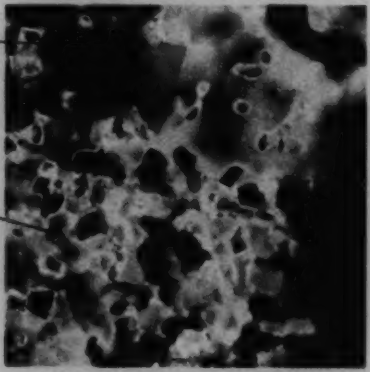

Figure 7-37: HAADF STEM image of an oxidized fuel cell sample showing the AFL-anode substrate interface.

Figure 7-38 shows a higher magnification image of the oxidized anode functional layer – electrolyte interface. The EDX spectra in Figure 7-39 and Figure 7-40 confirm that the two components are NiO and YSZ and illustrate the TEM's ability to do EDX analysis of very small areas compared to the SEM.

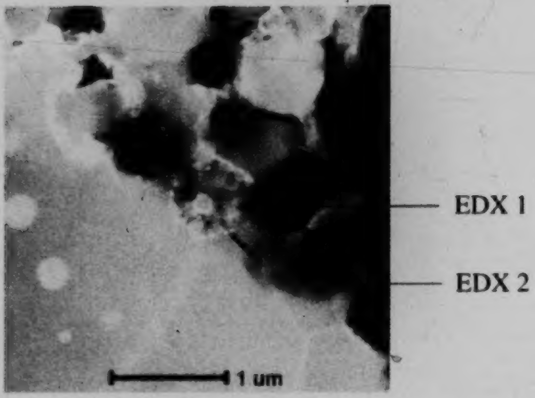

Figure 7-38: Higher magnification HAADF STEM image of an oxidized fuel cell sample showing the AFL-electrolyte interface.

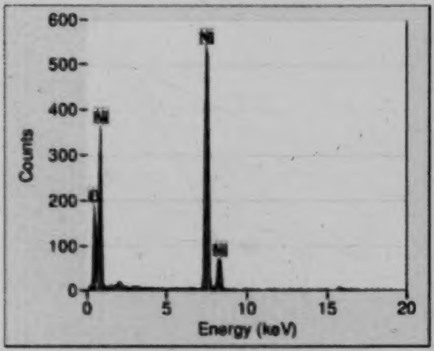

Figure 7-39: EDX spectrum from point 1 in Figure 7-38.

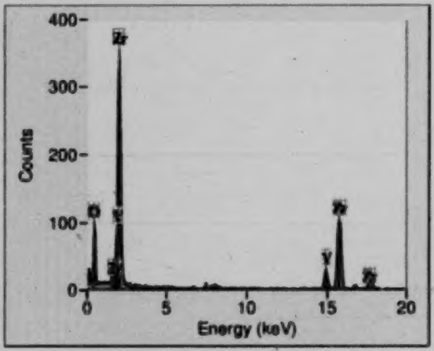

Figure 7-40: EDX spectrum from point 2 in Figure 7-38.

7.7.6. Visual examination of fuel cell samples

After redox cycling was complete, cells were either cooled down in a reduced state or were reoxidized for various amounts of time and then cooled down in nitrogen to preserve the microstructure in this oxidized state. Before examining the cells in the SEM or TEM, the cells and other test components (anode contact, test jigs, etc.) were visually examined during an "autopsy". Figure 7-41 to Figure 7-44 show images of the anode of the cell before and after testing. Initially, the cell is bright green, which indicates that the cell is fully oxidized. After reduction, the cell has become a uniform grey colour indicating that full reduction has occurred. Figure 7-43 and Figure 7-44 show the cell after redox cycling. The cell in Figure 7-43 was oxidized for 1 hour and then cooled in N_2, which gives a partially reoxidized microstructure. The area of the cell that is reoxidized is green (NiO) while the part of the cell that remains reduced is grey (Ni). The fully reoxidized cell shown in Figure 7-44 was oxidized for 4 hours and then cooled in N_2. The uniform green of the anode surface indicates that this cell is fully oxidized.

Figure 7-41: Image of the anode side of an as prepared cell.

Figure 7-42: Image of the anode side of a reduced cell after testing.

← Direction of air flow during redox cycling

Figure 7-43: Image of the anode side of a partially reoxidized redox cycled cell.

Figure 7-44: Image of the anode side of a fully reoxidized redox cycled cell.

Figure 7-45 shows a cross-sectional view of a polished, partially reoxidized sample fractured in the direction of air flow during reoxidation. The cell was fractured, stacked up into four layers, mounted in epoxy and then polished. The cross-section of the cell in the image runs from the top left corner of the image to the bottom right image corner. In the image the anode side of the cell is on top while the cathode side of the cell is on the bottom of each section. The cell cathode is not visible due to the low magnification of the image. The cell is fully oxidized at the cell edges (top left and bottom right corners) due to leakage in from the seals. It can be seen in the image that a gradient of oxidation exists from the air-in to the air-out side of the cell. Near the air-in side, the cell is completely reoxidized (green) and the amount of oxidation progressively lessens on moving to the air-out side until the cell is completely reduced (grey).

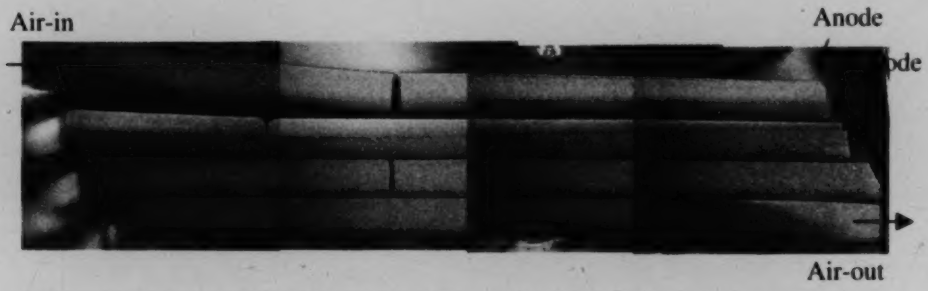

Figure 7-45: Cross-sectional view of a partially reoxidized cell. The cell was fractured and stacked up into four layers.

7.7.7. Damage caused by redox cycling

Figure 7-46 and Figure 7-47 show electrolyte cracking caused by redox cycling. These cracks are likely caused by the volume expansion exhibited by the AFL during oxidation. TMA shows that neither the anode substrate, nor the electrolyte, changes dimensions during oxidation so as the AFL expands during oxidation, it is constrained by the electrolyte and anode substrate layers, and stress builds up. If these stresses become too severe, the dense electrolyte may break causing fractures like those seen in the figures below. Electrolyte fractures will significantly decrease the OCV, performance and lifetime of fuel cells by allowing fuel and oxidant gases to mix and combust.

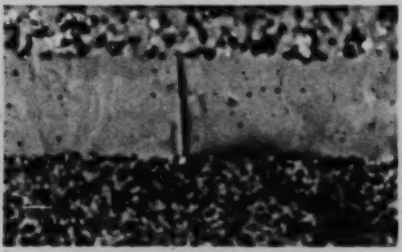

Figure 7-46: SEM BSE image of a fresh fractured anode-supported SOFC after redox cycling. Note the large vertical crack in the electrolyte.

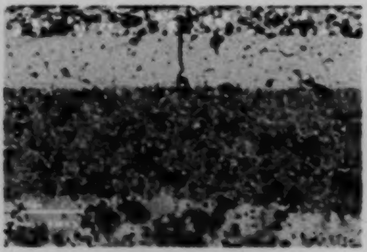

Figure 7-47: SEM BSE image of a polished anode-supported SOFC after redox cycling. Note the vertical crack in the electrolyte and oxidation of the AFL and anode substrate surrounding the crack.

Figure 7-48 and Figure 7-49 show another form of damage caused by redox cycling, i.e., microstructural damage. The sample shown in the figure was redox cycled, rereduced and cooled in nitrogen. It can be seen in the figures that the redox process has damaged the AFL microstructure and that the anode substrate near the damage is oxidized while the rest of the anode substrate remains in a reduced state.

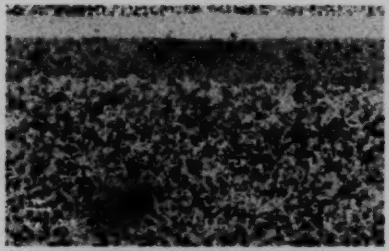

Figure 7-48: SEM BSE image of a polished anode-supported SOFC after redox cycling. Note the oxidation of the AFL and anode substrate in one small area near the electrolyte surrounded by reduced areas.

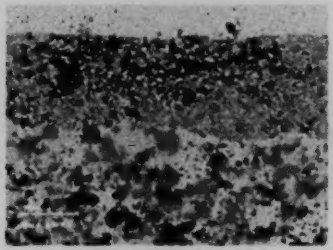

Figure 7-49: Higher magnification SEM image of Figure 7-48.

7.8.Summary of redox microstructural changes

7.8.1. Anode substrate samples

Figure 7-50 to Figure 7-53 show a summary of BSE SEM images of fresh fractured samples in the as prepared (oxidized), reduced and reoxidized conditions. In all the images, the YSZ phase is light in colour, with a grain size less than 1 μm in, while Ni and NiO particles appear grey and are several microns in size. Areas of porosity are black in the images. After reduction the porosity increases, which is consistent with the NiO volume reduction that should occur upon reduction. After reoxidation, the NiO particles appear spongy with much smaller pores than for the as prepared samples. This microstructural change is especially apparent in the higher magnification image in Figure 7-53.

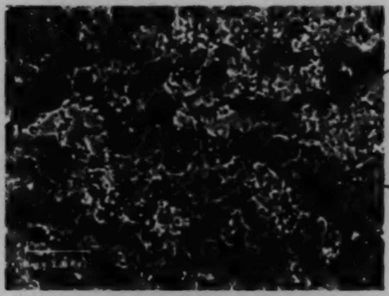

Figure 7-50: SEM BSE image of a fresh fractured as prepared sample (oxidized).

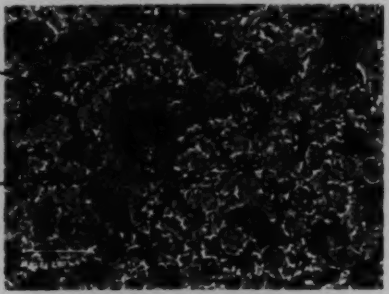

Figure 7-51: SEM BSE image of a fresh fractured reduced sample.

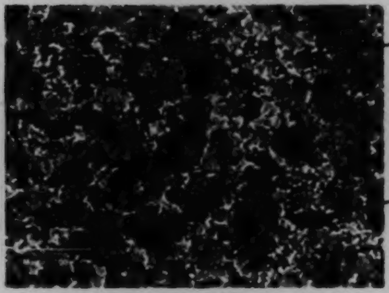

Figure 7-52: SEM BSE image of a fresh fractured reoxidized sample.

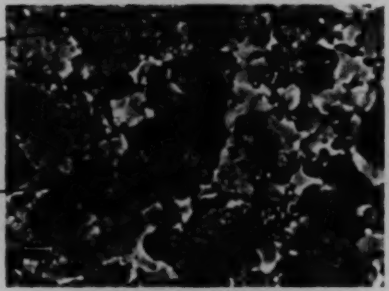

Figure 7-53: SEM BSE image of the reoxidized sample in Figure 7-52 at higher magnification.

The TEM images shown in Figure 7-54 to Figure 7-57 summarize the significant microstructural changes observed in more detail. In the as prepared condition the anode consists of NiO particles several microns in size, YSZ grains about one micron in size and intergranular porosity. After the first reduction, the overall Ni grain size remains the same as the consumed NiO and epitaxial growth of Ni crystals on NiO grains is observed. The amount of intergranular porosity increases and very fine (50 nm) intragranular pores are formed throughout the Ni grains. This increase in the amount of porosity is expected due to the large volume change that occurs upon reduction. When samples are reoxidized the NiO particles in the SEM images appear spongy with much smaller pores than the as received, oxidized samples. The reoxidized anode consists of fine (<100 nm), randomly oriented grains of NiO. The grain refinement that occurs upon reoxidation is likely due to the large number of intragranular pores that occur upon reduction, which serve as nucleation sites. Rereduced samples were also very fine grained (<200 nm) and contained significant amounts of small intergranular porosity. The YSZ grains were unaffected by the redox cycles.

Figure 7-54: BF TEM image of an as prepared sample.

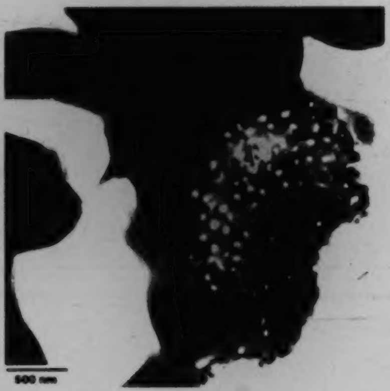

Figure 7-55: BF TEM image of a reduced sample.

Figure 7-56: BF TEM image of a reoxidized sample.

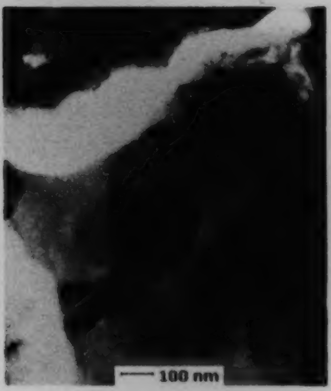

Figure 7-57: BF TEM image of a rereduced sample.

7.8.2. Fuel cell samples

SEM analysis of fuel cell samples (Figure 7-58 to Figure 7-61) confirmed the results seen in anode substrate samples. Both AFL and anode substrate layers were initially quite dense in the as prepared sample, but were made significantly more porous by reduction. After reoxidation the samples were again quite dense and the NiO in the anode substrate showed the same spongy microstructure as seen in anode substrate samples. Upon rereduction the microstructure was very similar to that seen in reduced samples.

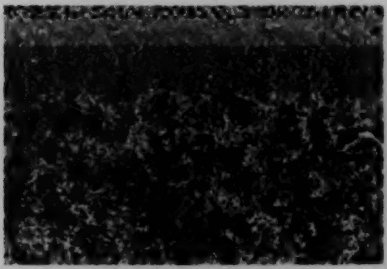

Figure 7-58: SEM BSE image of a fresh fractured, as prepared (oxidized) anode-supported SOFC.

Figure 7-59: SEM BSE image of a fresh fractured, reduced anode-supported SOFC.

Figure 7-60: SEM BSE image of a fresh fractured, reoxidized anode-supported SOFC.

Figure 7-61: SEM BSE image of a fresh fractured, rereduced anode-supported SOFC.

7.9.Bibliography

J. L. Goldstein, D. E. Newbury, P. Echlin, D. C. Joy, A. D. Romig Jr., C. E. Lyman, C. Fiori, E. Lifshin, *Scanning Electron Microscopy and X-Ray Microanalysis*, Plenum Press, New York, 1992.

D. B. Williams and C. B. Carter, *Transmission Electron Microscopy A Textbook for Materials Science*, Plenum Press, New York, 1996.

7.10. References

---

1 K. Tu, J.W. Mayer & L.C. Feldman, *Electronic Thin Film Science for Electrical Engineers and Materials Scientists*, Macmillan Publishing Company, New York, 1976, pp 167-174.

2 H. Kuhlenbeck, H.J. Freund, in: D.A. King, D.P. Woodruff (Eds.), *Growth and Properties of Ultrathin Epitaxial Layers*, Elsevier, Amsterdam, 1997 (Chapter 9).

Chapter 8: Enhancing the redox tolerance of SOFC

Abstract

The knowledge gained from TGA, TMA and baseline electrochemical testing was used to develop and evaluate cells with microstructural modifications designed to enhance redox tolerance.

The effect of oxidation temperature on cell redox tolerance was investigated at 600, 650 and 700°C and compared to baseline cell tests at 750°C. Redox cycling at 700°C enhanced the cell redox tolerance by over 50% while cycling at 600°C decreased the amount of redox degradation between 80 and 90% for a given volume of air passed into the anode chamber.

Nanosize carbon black pore formers were incorporated into the AFL paste in order to increase the porosity of the AFL. However, these cells had unstable performance and rapid degradation rates.

The Ni content of the AFL was functionally graded in order to decrease the amount of oxidation volume expansion near the electrolyte while still maintaining good conductivity and thermal expansion properties near the anode substrate. Grading the AFL increased the redox tolerance of the cell by 10 to 40% depending on the AFL composition.

A fine microstructured layer was printed on the bottom of the anode substrate to act as an oxidation barrier. Under the reducing conditions typical of operation, the barrier layer is porous to allow the fuel to pass through. If oxidizing conditions occur, the layer rapidly oxidizes and densifies in order to slow down the rate which oxygen penetrates into the anode. Cells with an oxidation barrier had a 40% improvement in redox tolerance for redox cycles up to 4 hours in length; however, the redox tolerance after the 6 hour cycle was only slightly improved. This indicates that the oxidation barrier does not completely stop the flow of oxygen into the cell.

Chapter 8: Enhancing the redox tolerance of SOFC 8-1

List of Figures 8-3
List of Tables 8-4

8. Enhancing the redox tolerance of SOFC 8-5
  8.1. Low temperature redox cycling 8-5
    8.1.1. Background 8-5
    8.1.2. Sample preparation 8-5
    8.1.3. Electrochemical results 8-5
    8.1.4. Microstructural results 8-9
    8.1.5. Voltage behaviour during oxidation 8-10
    8.1.6. GC analysis 8-10
  8.2. Increasing AFL porosity 8-11
    8.2.1. Background 8-11
    8.2.2. Sample preparation and characterization 8-11
    8.2.3. Electrochemical results 8-13
    8.2.4. Voltage behaviour during oxidation 8-15
  8.3. Functionally grading the AFL composition 8-15
    8.3.1. Background 8-15
    8.3.2. Sample preparation and characterization 8-15
    8.3.3. Electrochemical results 8-16
    8.3.4. Voltage behaviour during oxidation 8-19
  8.4. Blocking air flow with an oxidation barrier 8-19
    8.4.1. Background 8-19
    8.4.2. Sample preparation and characterization 8-20
    8.4.3. Electrochemical results 8-21
    8.4.4. High current results 8-24
    8.4.5. Microstructural results 8-25
    8.4.6. Voltage behaviour upon oxidation 8-27
    8.4.7. GC analysis 8-28
  8.5. Summary 8-29

List of Figures

Figure 8-1: Summary of the cumulative percent degradation per redox cycle for I-V curve tests for cells redox cycled at various temperatures...... 8-6
Figure 8-2: Summary of the cumulative percent degradation per redox cycle for steady-state tests for cells redox cycled at various temperatures.. 8-7
Figure 8-3: Summary of the cumulative percent OCV degradation per redox cycle for cells redox cycled at various temperatures.................... 8-9
Figure 8-4: BSE SEM image of the anode substrate of a cell reoxidized at 600°C.......... 8-9
Figure 8-5: BSE SEM image of the anode substrate of a cell reoxidized at 750°C.......... 8-9
Figure 8-6: BSE SEM image of a fully reoxidized cell after a redox cycle at 600°C.......... 8-10
Figure 8-7: SEM image of the carbon black particles used as pore formers.. 8-11
Figure 8-8: SEM image of a cell with an AFL containing pore formers........ 8-12
Figure 8-9: BSE SEM image of an as prepared cell with a regular AFL. 8-12
Figure 8-10: SEM image of a reduced cell with an AFL with pore formers.... 8-12
Figure 8-11: BSE SEM image of a reduced cell with a regular AFL. 8-12
Figure 8-12: BSE SEM image of a reoxidized cell with an AFL with pore formers.......... 8-12
Figure 8-13: BSE SEM image of a reoxidized cell with a regular AFL.......... 8-12
Figure 8-14: Summary of cumulative percent degradation per redox cycle for I-V curve tests for cells with an AFL layer containing pore formers. 8-14
Figure 8-15: Summary of the cumulative percent degradation per redox cycle for steady-state tests for cells with an AFL layer containing pore formers.......... 8-14
Figure 8-16: BSE SEM image of a cell with a functionally graded AFL......... 8-16
Figure 8-17: SEM image of a reduced cell with a functionally graded AFL ... 8-16
Figure 8-18: Summary of the cumulative percent degradation per redox cycle for I-V curve tests for cells with a graded AFL. 8-17
Figure 8-19: Summary of the cumulative percent degradation per redox cycle for steady-state tests for cells with a graded AFL............................ 8-18
Figure 8-20: Schematic diagram of a fuel cell with an oxidation barrier layer. 8-20
Figure 8-21: BSE SEM image of a fuel cell with an oxidation barrier............ 8-21
Figure 8-22: Summary of the cumulative percent degradation per redox cycle for I-V curve tests for cells with an oxidation barrier....................... 8-22
Figure 8-23: Summary of the cumulative percent degradation per redox cycle for steady-state tests for cells with an oxidation barrier. 8-23
Figure 8-24: High current and utilization results for a cell with an oxidation barrier. 8-25
Figure 8-25: BSE SEM image of the surface of a 57wt% NiO oxidation barrier layer in the reduced condition. 8-26
Figure 8-26: BSE SEM image of the surface of a 57wt% NiO oxidation barrier layer in the reoxidized condition. 8-26

Figure 8-27: BSE SEM image of the surface of a 75wt% NiO oxidation barrier layer in the reoxidized condition. 8-26
Figure 8-28: Cross sectional BSE SEM image of a 57wt% NiO oxidation barrier in the as prepared condition 8-27
Figure 8-29: Cross sectional BSE SEM image of a 57wt% NiO oxidation barrier in the reduced condition. 8-27
Figure 8-30: Cross sectional BSE SEM image of a 57wt% NiO oxidation barrier in the reoxidized condition. 8-27
Figure 8-31: Cross sectional BSE SEM image of a 75wt% NiO oxidation barrier in the reoxidized condition. 8-27
Figure 8-32: Voltage behaviour during cell oxidation for baseline cell tests. .. 8-28
Figure 8-33: Voltage behaviour during oxidation for a cell with an oxidation barrier. 8-28

List of Tables

Table 8-1: Summary of the amount of cumulative degradation for the I-V curve tests for cells redox cycled at various temperatures 8-7
Table 8-2: Summary of the amount of cumulative degradation for the steady-state hold tests for cells redox cycled at various temperatures 8-8
Table 8-3: Summary of the amount of cumulative degradation for the I-V curve tests for cells with a graded AFL 8-18
Table 8-4: Summary of the amount of cumulative degradation for the steady-state hold tests for cells with a graded AFL 8-19
Table 8-5: Summary of the amount of cumulative degradation for the I-V curve tests for cells with an oxidation barrier 8-22
Table 8-6: Summary of the amount of cumulative degradation for the steady-state hold tests for cells with an oxidation barrier 8-23
Table 8-7: Summary of the amount of cumulative degradation after 4 hour redox cycles for cells with an oxidation barrier 8-24
Table 8-8: Summary of the percent enhancement in redox tolerance for all methods of redox tolerance enhancement 8-31

8. Enhancing the redox tolerance of SOFC

The knowledge gained during the TGA, TMA and baseline electrochemical tests performed during the initial stages of this study was used to develop cells that have been modified in order to enhance their redox tolerance. The modified cell's electrochemical behaviour and microstructure were compared to the baseline of cell redox tolerance that was developed earlier. Four strategies to enhance redox tolerance were developed: redox cycling at lower temperatures, increased AFL porosity, functionally grading the composition of the AFL and the addition of an oxidation barrier to the bottom of the cell.

8.1. Low temperature redox cycling

8.1.1. Background

TGA showed that the reaction kinetics of nickel oxidation were very temperature dependent, therefore the rate of anode oxidation should be dramatically decreased at lower redox temperatures. As well, TMA found that the amount of volume expansion is decreased at lower oxidation temperatures, which indicates that redox cycles at lower temperatures should result in smaller amounts of nickel volume expansion during oxidation and thus less cell layer delamination and electrolyte cracking. In order to test these trends, redox tests were performed at 700, 650 and 600°C with standard TSC-2 cells and compared to the baseline redox tests at 750°C.

8.1.2. Sample preparation

Cells were prepared using FCE's standard TSC-2 procedure, which was explained in more detail in Section 6.1.

8.1.3. Electrochemical results

Standard redox cycling tests were performed at 600, 650, 700 and 750°C. The results of the I-V curve tests and steady-state hold tests are shown in Figure 8-1 and Figure 8-2 respectively.

Table 8-1 and Table 8-2 summarize the redox conditions and the amount of total cumulative degradation after redox cycling. The figures show that there is a very clear relationship between redox temperature and the amount of performance degradation. It appeared that just by decreasing the redox temperature 50°C (from 750 to 700°C) the amount of degradation could be decreased by 50% or more. If the redox temperature is decreased to 600°C the amount of cumulative degradation after the 6 hour redox cycle is less than 1% for steady-state hold tests. Another interesting trend seen was that the performance actually increased slightly after the 20 and 40 minute redox cycles. This phenomenon might be attributed to a slight enhancement in the anode contact or microstructure after brief redox cycles, which boosts the cell's performance.

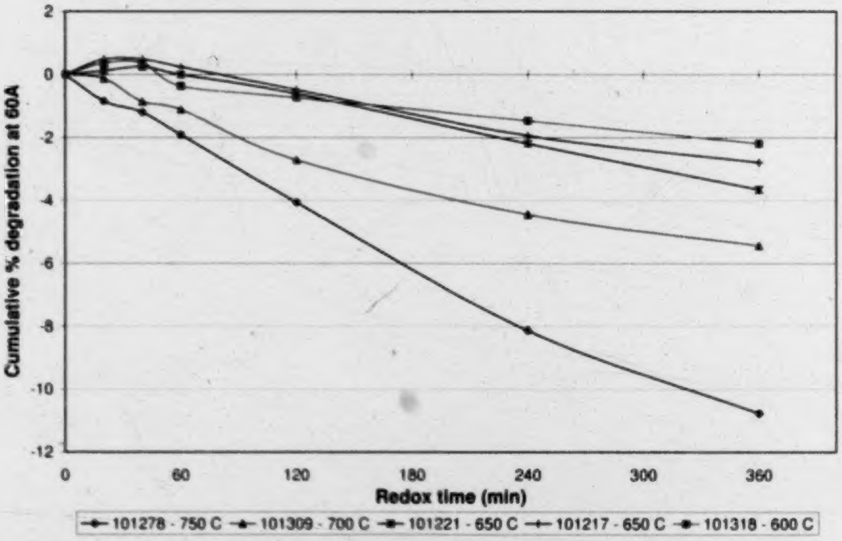

Figure 8-1: Summary of the cumulative percent degradation per redox cycle for I-V curve tests for cells redox cycled at various temperatures.

Table 8-1: Summary of the amount of cumulative degradation for the I-V curve tests for cells redox cycled at various temperatures

[illegible]	[illegible]	[illegible]	[illegible]	[illegible]	[illegible]	[illegible]
101278	750	-0.090	-10.8	6	20, 40, 60, 120, 240, 360	840
101309	700	-0.044	-5.4	6	20, 40, 60, 120, 240, 360	840
101221	650	-0.030	-3.7	6	20, 40, 60, 120, 240, 360	840
101217	650	-0.023	-2.8	6	20, 40, 60, 120, 240, 360	840
101318	600	-0.018	-2.2	6	20, 40, 60, 120, 240, 360	840

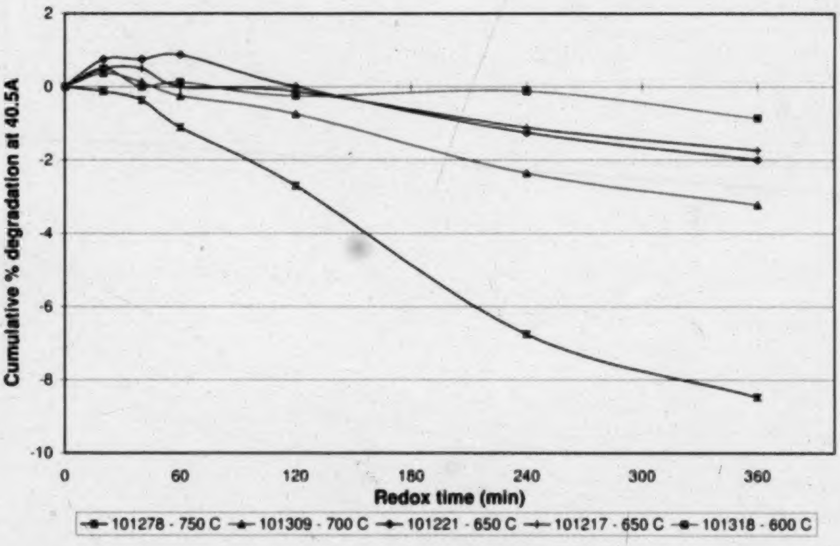

Figure 8-2: Summary of the cumulative percent degradation per redox cycle for steady-state tests for cells redox cycled at various temperatures.

Table 8-2: Summary of the amount of cumulative degradation for the steady-state hold tests for cells redox cycled at various temperatures

101270	750	-0.069	-8.5	6	20, 40, 60, 120, 240, 360	840
101308	700	-0.026	-3.2	6	20, 40, 60, 120, 240, 360	840
101221	650	-0.016	-2.0	6	20, 40, 60, 120, 240, 360	840
101217	650	-0.014	-1.7	6	20, 40, 60, 120, 240, 360	840
101318	600	-0.007	-0.9	6	20, 40, 60, 120, 240, 360	840

Redox cycling at temperatures lower than 750°C seemed to decrease the amount of OCV degradation after longer redox cycles (4 and 6 hours). This decrease in degradation may be caused by a decrease in the amount of oxidation volume expansion that occurs at lower temperatures as seen during TMA. If the AFL expands less after oxidation, there should be fewer electrolyte cracks after redox cycling and therefore the OCV should be higher. The amount of OCV degradation after redox cycling for baseline and lower temperature tests is shown in Figure 8-3. There is clearly much less OCV degradation for tests that have been redox cycled at temperatures lower than 750°C.

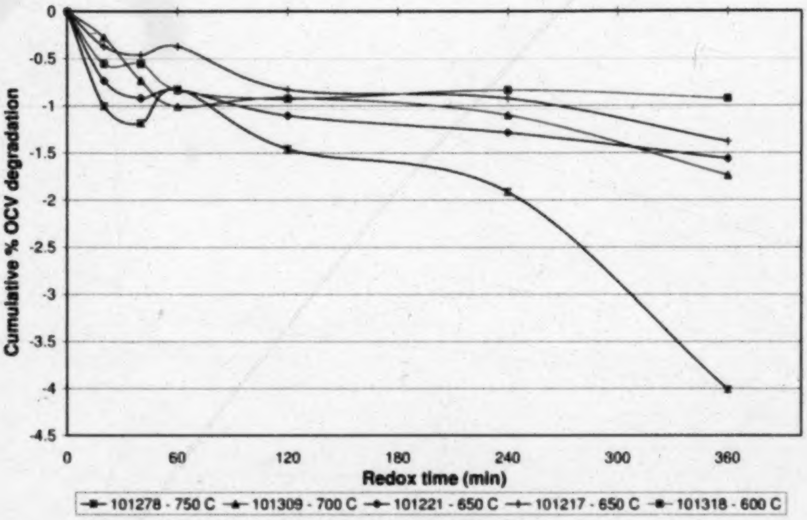

Figure 8-3: Summary of the cumulative percent OCV degradation per redox cycle for cells redox cycled at various temperatures.

8.1.4. Microstructural results

The microstructure of cells redox cycled at 750°C was compared to cells cycled at lower temperatures using SEM. The microstructure for all the cells was very similar regardless of the redox temperature. All cells exhibited the spongy NiO structure after reoxidation as seen in Figure 8-4 and Figure 8-5.

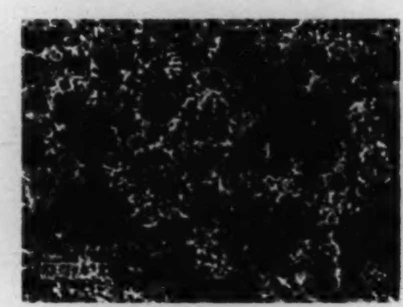

Figure 8-4: BSE SEM image of the anode substrate of a cell reoxidized at 600°C.

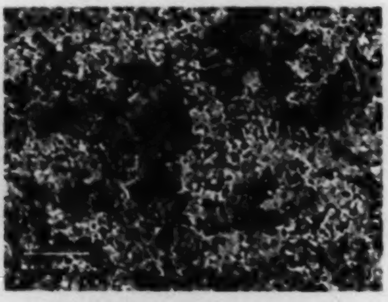

Figure 8-5: BSE SEM image of the anode substrate of a cell reoxidized at 750°C.

8.1.5. Voltage behaviour during oxidation

The majority of tests redox cycled at lower temperatures followed the same voltage decrease during oxidation trend as cells redox cycled at 750°C, i.e., the cell voltage decreased to 0 V after approximately 3.5 hours. The one exception was the redox test at 600°C. This test reached 0 V after approximately 1.5 hours. Upon analysis of the cell in the SEM, it was found that the cell was oxidized throughout the cell, all the way to the AFL (Figure 8-6), which accounts for the rapid voltage drop to zero. This evenly distributed oxidation may be a result of the slow oxidation kinetics at 600°C, which allowed oxygen to penetrate farther into the cell before reacting.

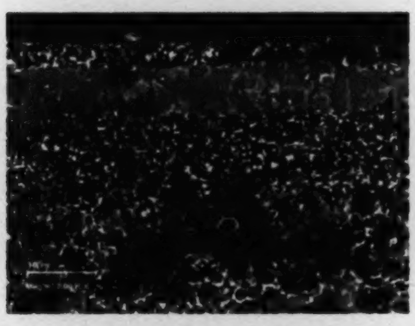

Figure 8-6: BSE SEM image of the cross section of a fully reoxidized cell after a one hour redox cycle at 600°C.

8.1.6. GC analysis

GC testing of the anode outlet gas during oxidation at 600°C was compared with the baseline results at 750°C. For redox at 600°C, approximately 1% oxygen was present in the anode outlet gas after about 1.5 hours of oxidation while for baseline tests at 750°C about 2 hours was needed to reach this gas composition. This may indicate that the slower oxidation rate seen at lower temperatures allows oxygen to pass through the anode chamber without reactions with the cell sooner than for baseline tests at 750°C.

8.2. Increasing AFL porosity

8.2.1. Background

TMA studies showed all fine microstructured AFL type samples expanded and cracked during oxidation regardless of oxidation temperature, while none of the coarse microstructured anode substrate samples expanded or cracked. One of the biggest differences in the microstructure of the AFL when compared to the anode substrate is the size, distribution and amount of porosity. In the current AFL, the expanding Ni is constrained by the YSZ support skeleton and eventually fractures this skeleton as the stresses induced by oxidation expansion increase to a critical level. But if the porosity of the AFL is increased, any volume increase due to oxidation may be accommodated by filling this added porosity rather than by fracturing the YSZ skeleton. Therefore extra porosity within the AFL should reduce the amount of layer delamination and cracking that occurs due to redox and thus increases the redox tolerance.

8.2.2. Sample preparation and characterization

Cells were prepared using FCE's standard TSC-2 procedure, which was explained in more detail in Section 6.1. A small amount of carbon black was added to the anode functional layer paste in order to increase its porosity. The carbon black particles (Figure 8-7) were fairly spherical with an average diameter of less than 1 μm.

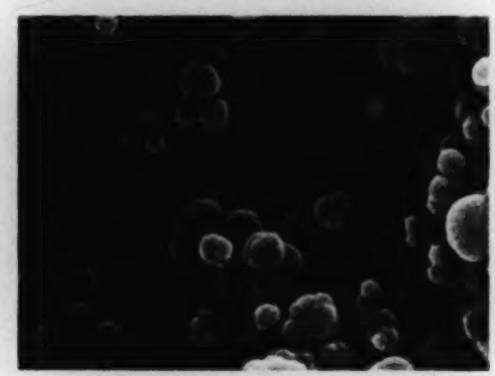

Figure 8-7: SEM image of the carbon black particles used as pore formers.

Figure 8-8 to Figure 8-13 are SEM images comparing a cell with pore formers in the AFL to a cell with a regular AFL. It can be seen in all the figures that the cells with pore formers have a much more porous AFL than the standard cells and thus should have better redox tolerance.

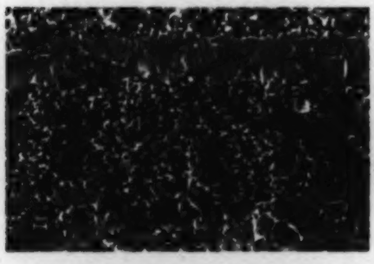

Figure 8-8: BSE SEM image of an as prepared cell with an AFL containing pore formers.

Figure 8-9: BSE SEM image of an as prepared cell with a regular AFL.

Figure 8-10: BSE SEM image of a reduced cell with an AFL containing pore formers.

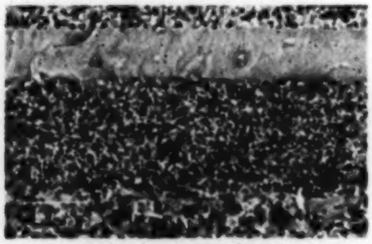

Figure 8-11: BSE SEM image of a reduced cell with a regular AFL.

Figure 8-12: BSE SEM image of a reoxidized cell with an AFL containing pore formers.

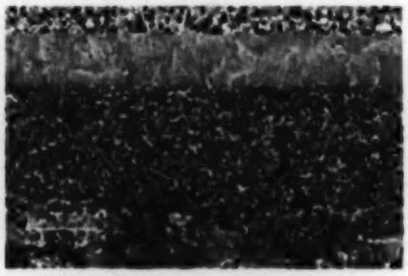

Figure 8-13: BSE SEM image of a reoxidized cell with a regular AFL.

8.2.3. Electrochemical results

Redox single cell test results for cells with an AFL layer containing pore formers were compared with baseline redox tests in Figure 8-14 and Figure 8-15. Even before redox cycling, these cells exhibited extremely rapid degradation, which made the separation of redox cycling losses from other sources of degradation an impossible task. The degradation rate was so rapid that tests 101302 and 101306 were stopped after the 1 hour redox cycle. Even the best pore former test (101290) had only marginally better redox tolerance than the redox baseline cell.

The rapid degradation and high redox losses indicate that the either the fabrication method or microstructure of these samples was not sufficiently optimized. The poor results may have been caused by cell defects introduced during fabrication; for example the carbon black pore former could have burnt out through the electrolyte and increased the amount of cross leak through this layer. The other possibility is that the microstructure of the sample may not be sufficiently optimized in order to provide stable performance. The added porosity in the AFL may be so large that there are fewer triple phase boundary areas, which resulted in decreased cell performance. Another possibility is that the increased amount of porosity has interrupted the continuity of the Ni particle network and thus decreased the electronic conductivity of the AFL and increased the ohmic losses.

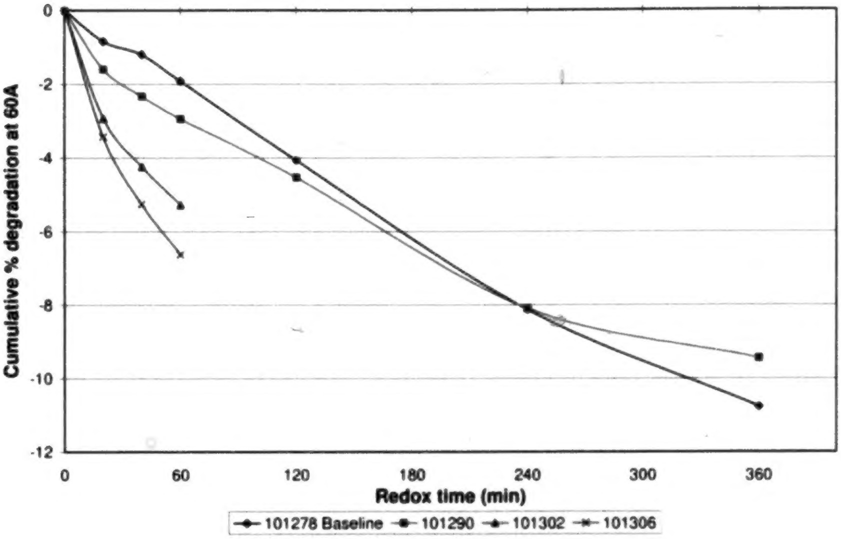

Figure 8-14: Summary of the cumulative percent degradation per redox cycle for I-V curve tests for cells with an AFL layer containing carbon black pore formers.

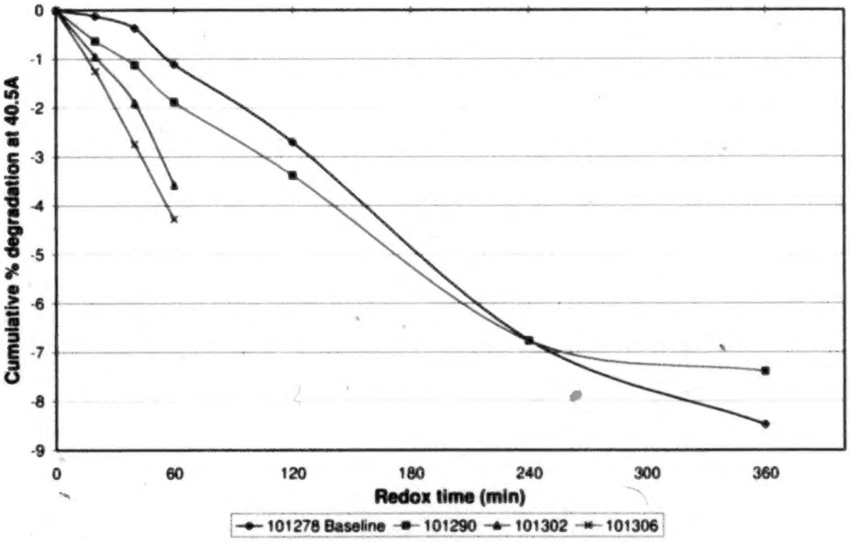

Figure 8-15: Summary of the cumulative percent degradation per redox cycle for steady-state tests for cells with an AFL layer containing carbon black pore formers.

8.2.4. Voltage behaviour during oxidation

The voltage behaviour during oxidation of these cells followed the same trend as baseline redox cycled cells. The cell voltage decreased to 0 V after approximately 3.5 hours.

8.3. Functionally grading the AFL composition

8.3.1. Background

TMA tests with AFL samples, containing more than 30wt% and less than 57wt% NiO, expanded less than standard 57wt% NiO samples upon oxidation. Therefore, if the amount of Ni in the AFL is reduced, less oxidation expansion might occur and thus the redox tolerance might be increased. The amount of Ni in the AFL must be high enough to ensure that the AFL has sufficient electronic conductivity, triple phase boundary length and porosity, but should be as low as possible in order to minimize the amount of oxidation volume expansion. In order to best satisfy these conflicting requirements, the Ni content in the AFL can be functionally graded so that the Ni content is high near the anode substrate to provide good electronic conductivity and thermal expansion match with the anode substrate and lower near the electrolyte so the layer expands less during oxidation and to better match electrolyte thermal expansion.

8.3.2. Sample preparation and characterization

Cells were prepared using FCE's standard TSC-2 procedure (see Section 6.1) except a modified paste was used for the second anode functional layer. All samples had a two layer AFL structure with the first layer (next to the anode substrate) consisting of a regular 57wt% NiO paste and the second layer (next to the electrolyte) consisting of a paste containing a lower amount of NiO. The total thickness of the graded anode functional layer was approximately the same as a regular cell. Three types of samples were fabricated: samples with a NiO content of 40wt% in the second anode functional layer, samples with a NiO content of 45wt% and samples with a NiO content of 50wt%. An SEM image of the first sample type in the as prepared and reduced condition is shown in Figure 8-16 and Figure 8-17 respectively.

Electrolyte
AFL 2 – 40 wt% NiO
AFL 1 – 57 wt% NiO
Anode substrate

Figure 8-16: BSE SEM image of an as prepared cell with a functionally graded AFL.

Figure 8-17: BSE SEM image of a reduced cell with a functionally graded AFL

8.3.3. Electrochemical results

The three types of graded AFL samples (40, 45 and 50wt% NiO) were redox cycled and compared to the baseline redox tests. I-V curve tests and steady-state hold test results are shown in Figure 8-18 and Figure 8-19. The redox testing conditions are summarized along with the total amount of cumulative degradation after redox cycling in Table 8-3 and Table 8-4. It can be seen in the figures that all graded AFL samples had better redox tolerance than standard cells.

Cells with an AFL with 40wt% NiO had unexpected redox behaviour. These cells had very rapid initial degradation rates and then had a drastic performance improvement after the 2 hour redox cycle. This behaviour was quite unexpected, but may have been caused by an enhancement in the connectivity of the Ni particle network, which improved the electronic conductivity of the AFL. Since the Ni content in the AFL was quite low in these samples it might actually be too low to provide stable initial performance. When the Ni in the AFL was oxidized, it expanded into the porosity in the AFL and may have come into better contact with the surrounding Ni particles. Upon reduction, the Ni particles may have maintained some of this enhanced contact, which improved the performance after redox cycling. On average, grading the AFL with 40wt% NiO enhanced the redox tolerance of the cell by about 42%, but the initial unstable performance means that higher Ni contents are likely necessary to ensure stable initial performance.

Cells with graded AFLs with Ni contents of 45 and 50wt% NiO also had enhanced redox tolerance compared to baseline cells and exhibited a rise in performance after the 20, 40 and 60 minute redox cycles. This performance increase was similar to that seen during lower temperature redox tests and thus may be ascribed to the same enhancement in contact or microstructure that improved the performance of those cells. On average grading the AFL with 45wt% NiO enhanced the redox tolerance of the cell by between 10 and 30% and grading the AFL with 50wt% NiO enhanced the redox tolerance of the cell by about 10%.

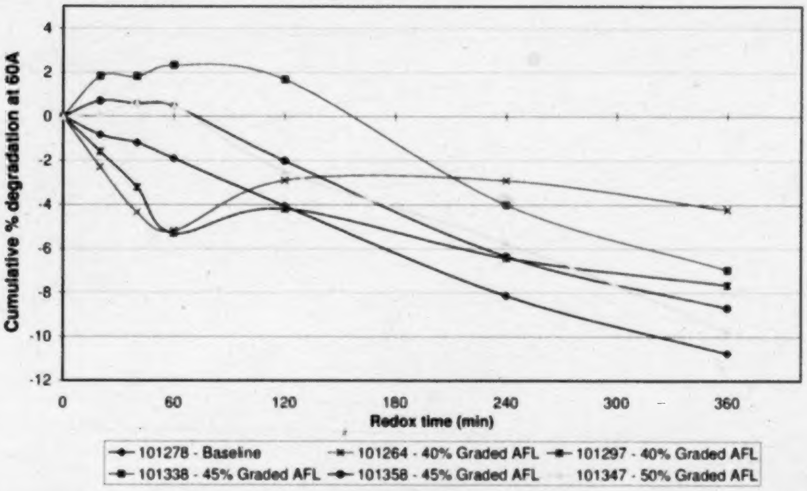

Figure 8-18: Summary of the cumulative percent degradation per redox cycle for I-V curve tests for cells with a graded AFL.

Table 8-3: Summary of the amount of cumulative degradation for the I-V curve tests for cells with a graded AFL

[illegible]	[illegible]	[illegible]	[illegible]	[illegible]	[illegible]	[illegible]
101278	Normal (57wt% NiO)	-0.090	-10.9	6	20, 40, 60, 120, 240, 360	840
101347	50wt% NiO / 57wt% NiO	-0.083	-9.7	6	20, 40, 60, 120, 240, 360	840
101358	45wt% NiO / 57wt% NiO	-0.070	-8.7	6	20, 40, 60, 120, 240, 360	840
101338	45wt% NiO / 57wt% NiO	-0.054	-6.5	6	20, 40, 60, 120, 240, 360	840
101297	40wt% NiO / 57wt% NiO	-0.062	-7.5	6	20, 40, 60, 120, 240, 360	840
101264	40wt% NiO / 57wt% NiO	-0.035	-4.2	6	20, 40, 60, 120, 240, 360	840

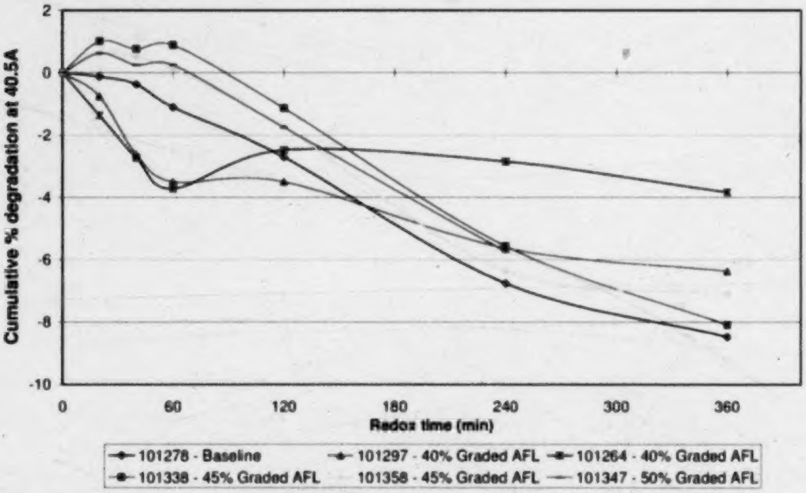

Figure 8-19: Summary of the cumulative percent degradation per redox cycle for steady-state tests for cells with a graded AFL.

Table 8-4: Summary of the amount of cumulative degradation for the steady-state hold tests for cells with a graded AFL

101278	Normal (57wt% NiO)	-0.069	-8.5	6	20, 40, 60, 120, 240, 360	840
101347	50wt% NiO / 57wt% NiO	-0.028	-5.7	5	20, 40, 60, 120, 240	480
101369	45wt% NiO / 57wt% NiO	-0.057	-7.1	6	20, 40, 60, 120, 240, 360	840
101339	45wt% NiO / 57wt% NiO	-0.064	-8.1	6	20, 40, 60, 120, 240, 360	840
101287	40wt% NiO / 57wt% NiO	-0.051	-6.4	6	20, 40, 60, 120, 240, 360	840
101384	40wt% NiO / 57wt% NiO	-0.031	-3.8	6	20, 40, 60, 120, 240, 360	840

After the six hour redox cycle, the cell in test 101347 had a very low OCV (1.001 V) and a voltage less than 0.6 V during the steady state hold test. This likely indicates that the electrolyte or seals had catastrophically failed, which prevented the cell from achieving 50% fuel and 25% air utilizations required during the steady state test.

8.3.4. Voltage behaviour during oxidation

The voltage behaviour during oxidation of these cells followed the same trend as baseline redox cycled cells. The cell voltage decreased to 0 V after approximately 3.5 hours.

8.4. Blocking air flow with an oxidation barrier

8.4.1. Background

The paste used for the anode functional layer (AFL) has a much finer microstructure and smaller pores than the anode substrate. In oxidizing conditions, a layer of this paste printed on the bottom of the cell will rapidly oxidize due to the fine microstructure and become very dense due to volume expansion upon oxidation filling the small pores. This dense layer will act as an oxidation barrier reducing the amount of air flowing into the anode, and thus slowing down the oxidation rate. In reducing conditions, the bottom layer will be porous and therefore will not interfere with cell operation. Thus this barrier should enhance the redox tolerance of the cell for short redox cycles by reducing the rate at which oxygen penetrates into the cell.

8.4.2. Sample preparation and characterization

Cells were prepared using FCE's standard TSC-2 procedure, which was explained in more detail in Section 6.1. Before the cell was co-fired, an oxidation barrier layer was printed on the bottom of the cell. A schematic diagram describing the location of the oxidation barrier layer in relation to the other fuel cell layers is shown in Figure 8-20. A low magnification BSE SEM image showing a fuel cell with an oxidation barrier layer is shown in Figure 8-21. Two types of samples were prepared: one sample had an oxidation barrier with exactly the same composition (57wt% NiO) and microstructure as the cell anode functional layer; the other sample had a higher Ni content (75wt% NiO) oxidation barrier layer in order to provide a more porous reduced layer and a more dense oxidized layer. The oxidation barrier layer was about 14 μm thick after firing.

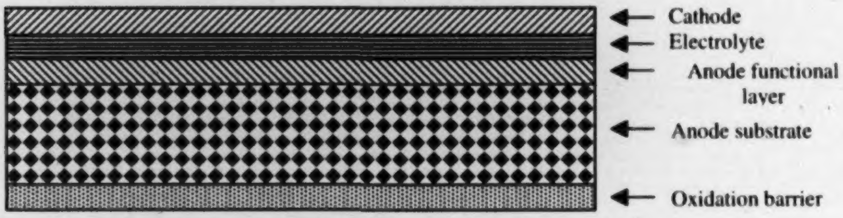

Figure 8-20: Schematic diagram of a fuel cell with an oxidation barrier layer.

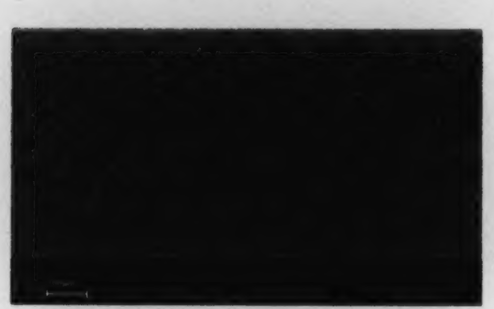

Figure 8-21: Low magnification BSE SEM image of a fuel cell with an oxidation barrier.

8.4.3. Electrochemical results

Redox single cell test results for samples with an oxidation barrier are compared to baseline cell results in Figure 8-22 and Figure 8-23. Table 8-5 and Table 8-6 summarize the testing conditions and the cumulative amount of degradation after redox cycling. It can be seen in the figures, that the amount of degradation after redox cycling is significantly reduced for cells with an oxidation barrier for redox cycles up to 4 hours in length. After the 6 hour redox cycle, the redox tolerance of the oxidation barrier cells was equivalent or slightly better than baseline cells. This trend indicates that the redox tolerance for cells with an oxidation barrier is enhanced for intermediate redox times (1 to 4 hours) due to a lowering of the rate that oxygen penetrates into the anode. However, oxygen is not completely prevented from entering the cell, so that complete oxidation and the subsequently high amount of degradation will still occur for longer redox times. The amount of time required for complete oxidation has just been lengthened for oxidation barrier cells. The two types of samples with oxidation barriers appeared to have about the same redox tolerance, even though one sample had an oxidation barrier with a much higher amount of Ni.

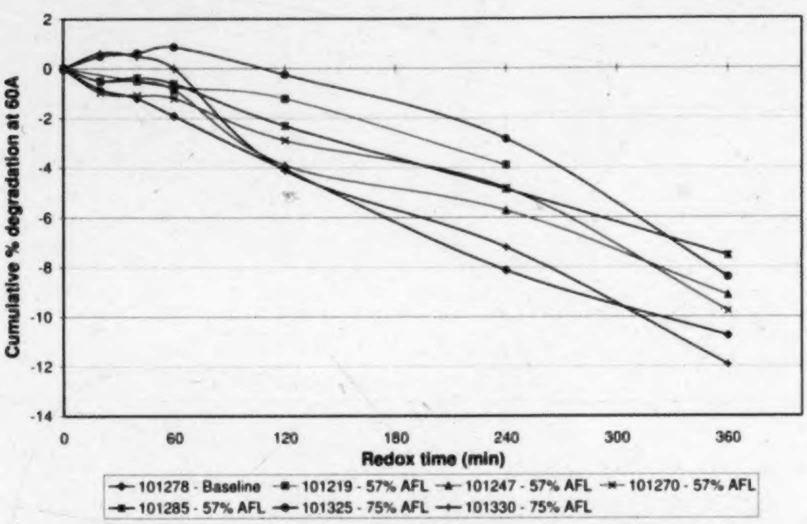

Figure 8-22: Summary of the cumulative percent degradation per redox cycle for I-V curve tests for cells with an oxidation barrier.

Table 8-5: Summary of the amount of cumulative degradation for the I-V curve tests for cells with an oxidation barrier

101278	Baseline	-0.090	-10.8	6	20, 40, 60, 120, 240, 360	840
101219	57	-0.032	-3.9	3	60, 120, 240	420
101247	57	-0.075	-9.1	6	20, 40, 60, 120, 240, 360	840
101270	57	-0.081	-9.8	6	20, 40, 60, 120, 240, 360	840
101285	57	-0.062	-7.5	6	20, 40, 60, 120, 240, 360	840
101325	75	-0.068	-8.4	6	20, 40, 60, 120, 240, 360	840
101330	75	-0.096	-11.9	6	20, 40, 60, 120, 240, 360	840

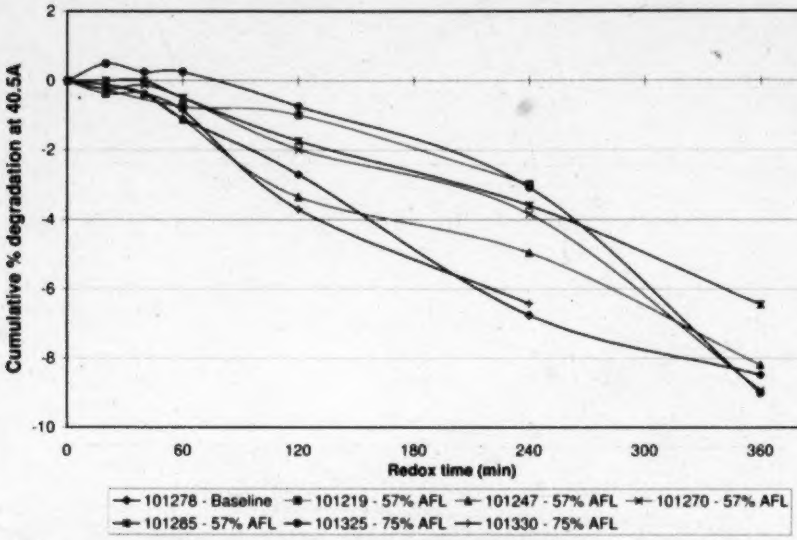

Figure 8-23: Summary of the cumulative percent degradation per redox cycle for steady-state tests for cells with an oxidation barrier.

Table 8-6: Summary of the amount of cumulative degradation for the steady-state hold tests for cells with an oxidation barrier

[illegible]	[illegible]	[illegible]	[illegible]	[illegible]	[illegible]	[illegible]
101278	Baseline	-0.069	-8.5	6	20, 40, 60, 120, 240, 360	840
101219	57	-0.024	-3.0	3	60, 120, 240	420
101247	57	-0.066	-8.2	6	20, 40, 60, 120, 240, 360	840
101270	57	-0.072	-8.9	6	20, 40, 60, 120, 240, 360	840
101285	57	-0.052	-6.5	6	20, 40, 60, 120, 240, 360	840
101325	75	-0.073	-9.0	6	20, 40, 60, 120, 240, 360	840
101330	75	-0.052	-6.4	6	20, 40, 60, 120, 240	480

After the six hour redox cycle, the cell in test 101330 had a very low OCV (0.961 V) and a voltage less than 0.6 V during the steady state hold test. This likely indicates that the electrolyte or seals had catastrophically failed, which prevented the cell from achieving 50% fuel and 25% air utilizations required in the steady state test.

Table 8-7 summarizes the cumulative amount of degradation after a 4 hour redox cycle. It can be seen in the table, that the amount of degradation after a 4 hour redox cycle, for cells with an oxidation barrier, is reduced on average by about 40% when compared to the baseline cell.

Table 8-7: Summary of the amount of cumulative degradation after 4 hour redox cycles for cells with an oxidation barrier

[illegible]	[illegible]	[illegible]	[illegible]	[illegible]	[illegible]
101278	**Baseline**	**-0.068**	**-8.1**	**-0.055**	**-6.8**
101219	57	-0.032	-3.9	-0.024	-3.0
101247	57	-0.047	-5.7	-0.04	-5.0
101270	57	-0.04	-4.8	-0.031	-3.8
101286	57	-0.04	-4.9	-0.029	-3.6
101325	75	-0.023	-2.8	-0.025	-3.1
101330	75	-0.058	-7.2	-0.052	-6.4
Average	-	**-0.040**	**-4.9**	**-0.034**	**-4.2**

8.4.4. High current results

In order to validate that the oxidation barrier does not impede the flow of fuel and thus decrease the performance at higher current densities and fuel utilizations by increasing the amount of mass transport losses, a test was performed at 70% fuel utilization and 35% air utilization to a maximum current of 100A ($1.23A/cm^2$). The results of this test were compared to that of a standard cell at 70% fuel and 50% air utilization and one at 70% fuel and 25% air in Figure 8-24. It can be seen in the figure that the performance of a cell with an oxidation barrier at high current and utilization was a bit lower than that of a regular cell, but that the shape of the I-V curve for the oxidation barrier cell does not indicate that mass transport losses due to fuel flow restrictions are occurring.

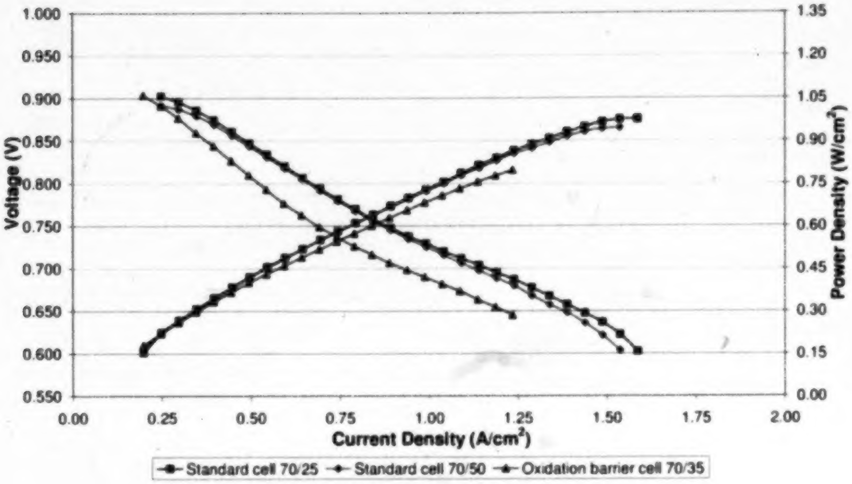

Figure 8-24: High current and utilization results for a standard cell compared to a cell with an oxidation barrier.

8.4.5. Microstructural results

Figure 8-25 to Figure 8-27 show BSE SEM images of the surface of the oxidation barrier of the cell. It can be seen that the reoxidized oxidation barriers in Figure 8-26 and Figure 8-27 look much more dense than the reduced oxidation barrier shown in Figure 8-25, which indicates that the oxidation barrier should work well to slow down the rate at which oxygen penetrates into the anode during oxidation. However, none of the oxidation barriers appear to be fully dense which indicates that none of the barriers will prevent oxidation from occurring. In the figures, the 75wt% NiO reoxidized oxidation barrier shown in Figure 8-27 appears to be much more dense than the 57wt% reoxidized barrier.

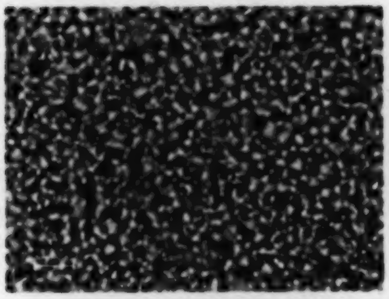

Figure 8-25: BSE SEM image of the surface of a 57wt% NiO oxidation barrier layer in the reduced condition.

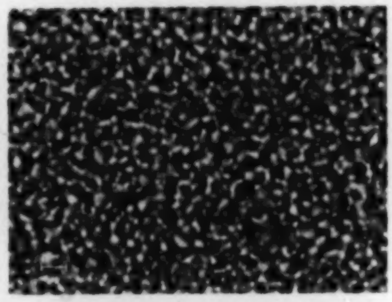

Figure 8-26: BSE SEM image of the surface of a 57wt% NiO oxidation barrier layer in the reoxidized condition.

Figure 8-27: BSE SEM image of the surface of a 75wt% NiO oxidation barrier layer in the reoxidized condition.

Figure 8-28 to Figure 8-31 show cross sectional views of the oxidation barriers in the as prepared, reduced and reoxidized conditions. The difference in porosity between the as prepared (Figure 8-28), reduced (Figure 8-29) and reoxidized (Figure 8-30) samples is readily apparent in the figures. The sample with a 75wt% NiO oxidation barrier in the reoxidized condition looks very similar to the reoxidized 57wt% NiO oxidation barrier in the cross sectional images. This may explain why there seemed to be very little difference in redox tolerance between the two types of oxidation barrier samples.

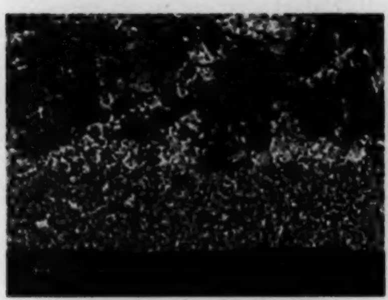

Figure 8-28: Cross sectional BSE SEM image of a 57wt% NiO oxidation barrier in the as prepared condition.

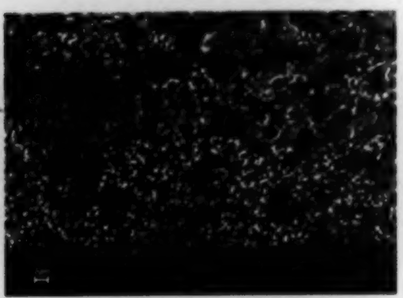

Figure 8-29: Cross sectional BSE SEM image of a 57wt% NiO oxidation barrier in the reduced condition.

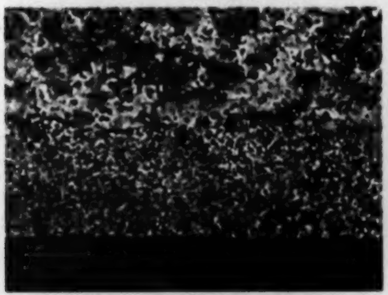

Figure 8-30: Cross sectional BSE SEM image of a 57wt% NiO oxidation barrier in the reoxidized condition.

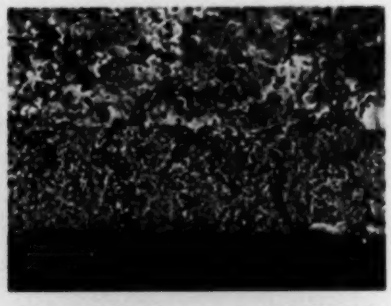

Figure 8-31: Cross sectional BSE SEM image of a 75wt% NiO oxidation barrier in the reoxidized condition.

8.4.6. Voltage behaviour upon oxidation

Figure 8-32 and Figure 8-33 compare the voltage behaviour during oxidation of a baseline redox test and a test of a cell with an oxidation barrier. It can be seen that the voltage reaches 0 V after approximately 3.5 hours of oxidation for the baseline test, while the cell with an oxidation barrier has still not reached 0 V after 6 hours of oxidation. This data strongly supports the idea that the oxidation barrier reduces the rate at which oxygen penetrates into the anode.

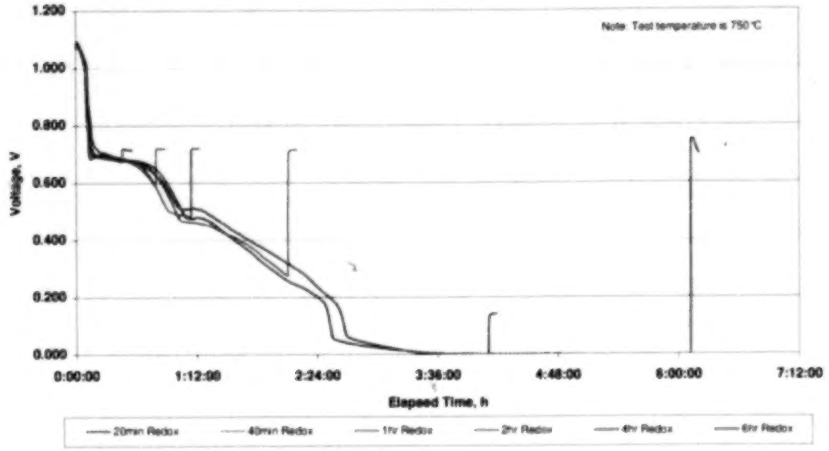

Figure 8-32: Voltage behaviour during cell oxidation for the baseline cell test.

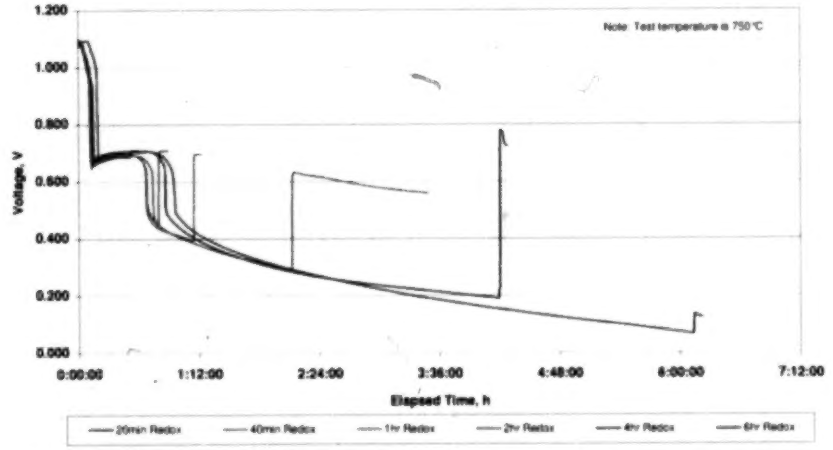

Figure 8-33: Voltage behaviour during oxidation for a cell with an oxidation barrier.

8.4.7. GC analysis

GC analysis during oxidation showed that oxygen appeared in the anode outlet much faster for cells with an oxidation barrier compared to baseline cells. Approximately 1% oxygen was seen in the anode outlet of baseline cells after about 2 hours of oxidation, while it took only 30 to 60 minutes for oxygen to be present in the anode outlet during oxidation barrier redox tests. This result confirms that the oxidation barrier does actually block some oxygen from penetrating into the anode during oxidation.

8.5.Summary

Four methods to enhance the redox tolerance of SOFC anodes were developed from the knowledge gained from TGA, TMA and baseline electrochemical tests.

The effect of redox temperature was studied by performing redox cycles at 600, 650, 700 and 750°C and comparing the amount of degradation after the cycles were complete. Temperature had a significant effect on the redox tolerance of the cell. Decreasing the redox temp to 700°C resulted in a greater than 50% decrease in redox degradation while redox cycling at 600°C increased the redox tolerance by between about 80 and 90% for a given volume of air passed into the anode chamber.

The porosity of the AFL was increased by adding carbon black pore formers in order to increase the redox tolerance of the cell. This method was successful in producing cells with a more porous AFL microstructure, but none of the cells exhibited stable performance. The high degradation during testing made separation of the redox cycling losses from other sources of degradation impossible. The unstable performance of these cells indicates that the fabrication method or microstructure was not sufficiently optimized.

In order to decrease the amount of oxidation volume expansion, the composition of the AFL was functionally graded. The functionally graded AFL had a lower amount of Ni near the electrolyte in order to decrease the amount of oxidation volume expansion, and a higher Ni content near the anode substrate in order to provide good electronic conductivity and thermal expansion match. Samples with a 40wt% NiO graded AFL had high initial degradation, but had a significant increase in performance after the 2 hour redox cycle. After this performance increase, the cells exhibited stable performance and significantly improved redox tolerance. On average, grading the AFL with 40wt% NiO enhanced the redox tolerance of the cell by about 42%, but the initial unstable performance means that higher Ni contents are likely necessary to maintain stable initial performance. Cells with 45 and 50wt% NiO graded AFL had stable performance and also had improved redox tolerance when compared to the baseline redox tests. On average, grading the AFL with 45wt% NiO enhanced the redox tolerance of the cell by between 10 and 30% and grading the AFL with 50wt% NiO enhanced the redox tolerance of the cell by about 10% after the 6 hour redox cycle.

The final method to improve cell redox tolerance involved printing an oxidation barrier layer with a fine microstructure similar to the AFL on the bottom surface of the anode substrate. In reducing conditions, the layer is porous in order to allow normal cell operation while in oxidizing conditions the layer rapidly oxidizes and densifies in order to restrict the rate that oxygen penetrates into the cell. Cells with an oxidation barrier had significantly increased redox tolerance for redox cycles up to 4 hours in length and slightly improved redox tolerance after a 6 hour redox cycle. The use of an oxidation barrier decreased the amount of redox degradation after a 4 hour redox cycle by 40% compared to baseline cells.

Table 8-8 summarizes the percent enhancement in redox tolerance for all the different methods of redox tolerance enhancement investigated in this study.

Table 8-8: Summary of the percent enhancement in redox tolerance for all methods of redox tolerance enhancement

[illegible]	[illegible]	[illegible]	[illegible]	[illegible]
Baseline	-10.8	-8.5	-	-
700 C redox	-5.4	-3.2	49.5	61.9
650 C redox	-3.2	-1.9	70.0	78.0
600 C redox	-2.2	-0.9	79.6	89.8
AFL pore formers	-9.4	-7.4	12.2	12.8
40% Graded AFL#	-5.9	-5.1	45.7	39.7
45% Graded AFL	-7.6	-7.6	29.4	10.4
50% Graded AFL*	-5.7	-5.7	29.6	15.0
Oxidation barrier*	-4.9	-4.2	39.8	38.6

# Note: 40% Graded AFL tests had rapid initial degradation rates, but their performance drastically improved after the 2 hour redox cycle.
* Note: 50% Graded AFL and oxidation barrier tests did not have significantly improved cell redox tolerance after 6 hour redox cycles (10.5 and 8.5 % enhancement respectively), so results after the 4 hour redox cycle were used to calculate the percent enhancement in redox tolerance for these tests.

Chapter 9: Recommendations and Future Work

Abstract

This chapter gives a few recommendations for future redox studies that might be of interest.

9. Recommendations and future work

Although this study was fairly comprehensive, there are always areas where a more in depth study would be of value.

Further TG studies that may be of interest might include: a study of the redox kinetics of AFL samples or a detailed study looking at the effects of partial pressure of oxygen, humidity and flow rate of gases on reduction and oxidation rates. As well, the development of a model for Ni/YSZ reduction and oxidation might be of use.

TMA of AFL samples fabricated from pastes containing pore formers may be useful. As well, a TMA study looking at the synergistic effects of lowering the amount of Ni and increasing the porosity by using pore formers to see whether the amount of volume expansion can be further reduced would be interesting.

Other important characteristics like porosity and conductivity should be measured for anode substrate and AFL samples with different Ni compositions in the as prepared, reduced, reoxidized and rereduced states in order to further optimize the composition and microstructure of cells.

Further research to modify the anode microstructure to enhance redox tolerance should also be performed. Cells with lower amounts of pore formers should be fabricated and tested to obtain cells with more stable performance. The composition and microstructure of the oxidation barrier should be modified further in order to enhance the cell redox tolerance and even oxidation barrier layers composed of materials other than Ni/YSZ should be considered.